


8-2015

THREE-DIMENSIONAL SCAFFOLDS OF GRAPHENE, CARBON NANOTUBES AND TRANSITION-METAL OXIDES FOR APPLICATIONS IN ELECTRONICS, SENSORS AND ENERGY STORAGE

Gilbert N. Mbah

University of Nebraska-Lincoln, ngohmbahgilbert@yahoo.com

Follow this and additional works at: <http://digitalcommons.unl.edu/chemistrydiss>

 Part of the [Energy Systems Commons](#), [Materials Chemistry Commons](#), and the [Nanoscience and Nanotechnology Commons](#)

Mbah, Gilbert N., "THREE-DIMENSIONAL SCAFFOLDS OF GRAPHENE, CARBON NANOTUBES AND TRANSITION-METAL OXIDES FOR APPLICATIONS IN ELECTRONICS, SENSORS AND ENERGY STORAGE" (2015). *Student Research Projects, Dissertations, and Theses - Chemistry Department*. 59.
<http://digitalcommons.unl.edu/chemistrydiss/59>

This Article is brought to you for free and open access by the Chemistry, Department of at DigitalCommons@University of Nebraska - Lincoln. It has been accepted for inclusion in Student Research Projects, Dissertations, and Theses - Chemistry Department by an authorized administrator of DigitalCommons@University of Nebraska - Lincoln.

THREE-DIMENSIONAL SCAFFOLDS OF GRAPHENE, CARBON NANOTUBES AND
TRANSITION-METAL OXIDES FOR APPLICATIONS IN ELECTRONICS, SENSORS
AND ENERGY STORAGE

By

Gilbert Ngoh Mbah

A THESIS

Presented to the Faculty of
The Graduate College at the University of Nebraska
In Partial Fulfilment of Requirements
For the Degree of Master of Science

Major: Chemistry

Under the Supervision of Professor Sinitskii Alexander

Lincoln, Nebraska

August, 2015

Three-dimensional scaffolds of graphene, carbon nanotubes and transition-metal oxides
for applications in electronics, sensors and energy storage

Gilbert Ngoh Mbah, M.S.

University of Nebraska, 2015

Adviser: Alexander Sinitskii

Electronics, sensors and energy storage devices are the new waves behind economic development, security and communication¹. Engineering small sizes of electronic, sensors and energy storage devices is the hurdle limiting efficient, portable and vast applications of Nano-devices for economic, security and communication advancement². Silicon the major material used in transistors has approached its limit to fabricated Nano-devices³. The discovery of free standing, one atomic layer thick and two-dimensional graphene sheets with high conductivity, inert, high specific surface area, stable and high tensile strength material in 2004 has shown capabilities to replaced silicon in electronics, sensors and energy storage devices⁴. Graphene and carbon nanotubes allotropes of carbon have gained momentum as the best materials for the advancement of electronics, sensors and energy storage sectors. Research has shown that 3D structuring of graphene and carbon nanotubes will expand their properties as well as applications. Unfortunately there is no technology to synthesize these materials in 3D and in bulk for applications in electronics, sensors and energy storage devices. Here, we present new technologies to synthesize new 3D materials of graphene, carbon nanotubes, manganese dioxide and tungsten trioxide. We also illustrate some of the possible applications of some of these materials in sensor and electrochromic devices.

Table of Contents

| | |
|--|------|
| List of Figures | ix |
| Acknowledgements | xii |
| Dedication | xiii |
| Chapter 1 | 1 |
| Three dimensional microporous architecture of highly connected graphene inverse opal scaffold | 1 |
| Introduction..... | 1 |
| 1. 1. 0 study of graphene..... | 2 |
| 1.1.1 Applications of graphene..... | 2 |
| 1. 1. 2 Graphene for electronics..... | 3 |
| 1. 1. 3 Graphene for energy storage..... | 4 |
| 1. 1. 4 Graphene for biomedical devices..... | 5 |
| 1. 1. 5 Graphene for light processing devices..... | 6 |
| 1. 2. 0 Synthesis of graphene..... | 6 |
| 1. 2. 1 Mechanical exfoliation of graphene..... | 6 |
| 1. 2. 2 Chemical vapor deposition of graphene..... | 8 |
| 1. 2. 3 Chemical exfoliation of graphite..... | 9 |
| Chapter 2 | 11 |

| | |
|--|----|
| Three dimensional microporous architecture of highly connected graphene inverse opals | 11 |
| 2. 1. 0 Introduction..... | 11 |
| 2. 2. 0 Experimental..... | 12 |
| 2. 2. 1 Synthesis of polystyrene spheres..... | 12 |
| 2. 2. 2 Electrochemical deposition of nickel inverse opals..... | 13 |
| 2. 2. 3 Synthesis of graphene inverse opals..... | 14 |
| 2. 3. 0 Analyses of the graphene inverse opals..... | 15 |
| 2. 3. Polystyrene spheres..... | 15 |
| 2. 3. 2 Analyses of electrodeposited nickel inverse opals..... | 17 |
| 2. 3. 3 Synthesized graphene inverse opals..... | 19 |
| 2. 3. 4 Raman spectroscopy study of graphene inverse opals scaffolds..... | 22 |
| 2. 3. 5 X-ray diffraction analyses of graphene inverse opals..... | 24 |
| 2. 3. 6 Energy dispersive X-ray spectroscopy analyses of graphene inverse opals..... | 25 |
| 2. 4. 0 Discursions..... | 26 |
| 2. 5. 0 Conclusions..... | 28 |
| 2. 4. 0 Future works..... | 28 |
| Chapter 3 | 30 |

| | |
|--|----|
| Three dimensional microspores architecture of carbon nanotubes inverse opals scaffolds | 30 |
| 3. 0. 0 Introduction..... | 30 |
| 3. 1. 0 Experimental..... | 31 |
| 3. 1. 1 Requirements..... | 31 |
| 3. 1. 2 syntheses of three dimensional carbon nanotubes..... | 32 |
| 3. 1. 3 Micro-contact printing of two dimensional iron oxide template..... | 33 |
| 3. 2. 0 Chemical vapor depositions of carbon nanotubes inverse opals..... | 35 |
| 3. 3. 0. Analyses and results of carbon nanotubes inverse opals..... | 39 |
| 3. 3. 1 Optical analyses of iron oxide template..... | 39 |
| 3. 3. 2 Field emission scanning electron microscopy of CNTs-IOs..... | 39 |
| 3. 3. 3 Raman, XRD and EDX analyses of CNTs-IOs..... | 40 |
| 3. 4. 0 Discursions..... | 42 |
| 3. 5. 0 Conclusions..... | 43 |
| 3. 6. 0 Future works..... | 43 |
| Chapter 4 | 44 |
| The-dimensional manganese (IV) oxide inverse opals architecture for oxygen reduction reaction (ORR) | 44 |

| | |
|---|-----------|
| 4. 1. 0 Introduction..... | 44 |
| 4. 2. 0 Experimental..... | 46 |
| 4. 2. 1 Syntheses of manganese oxide (MnO _x) inverse opals..... | 47 |
| 4. 2. 2 Thermal oxidation of MnO _x in air..... | 47 |
| 4.2 .3 Electrochemical oxidation of manganese dioxide nanosheets..... | 49 |
| 4. 2. 4 Study of polystyrene spheres presence in manganese dioxide nanosheets..... | 50 |
| 4. 2. 5 Manganese dioxide nanosheets catalyst ORR..... | 51 |
| 4. 3. 0 Analyses of manganese dioxide inverse opals nanosheets..... | 51 |
| 4. 3. 1 Flame atomic absorption spectroscopy of manganese oxides..... | 52 |
| 4. 4. 0 Oxygen sensors..... | 59 |
| 4. 5. 0 Discursions..... | 60 |
| 4. 6. 0 Conclusions..... | 61 |
| 4.7.0 Future works..... | 62 |
| Chapter 5..... | 63 |
| Flexible transparent electrochromic device of electrochemical deposited tungsten (VI) Oxide on graphene electrode..... | 63 |
| 5. 1. 0 Introduction..... | 63 |
| 5. 2. 0 Experimental..... | 64 |

| | |
|---|-----------|
| 5. 3.0 Tungsten (VI) oxide..... | 65 |
| 5. 4. 0 Thermal deposition of tungsten trioxide..... | 65 |
| 5. 4. 1 Field emission scanning electron microscopy analysis of WO_x | 66 |
| 5. 4. 2 Synthesis of Bilayer graphene..... | 67 |
| 5. 4. 3 Electrochemical deposition of WO_3 on graphene..... | 68 |
| 5. 4. 4 Study of WO_3 grown on graphene..... | 68 |
| 5. 5. 0 Analyses of WO_3 thin film..... | 69 |
| 5. 5. 1 Scanning electron microscopy study of the synthesized WO_3 | 70 |
| 5. 5. 2 X-Ray diffraction study of the synthesized WO_3 film..... | 71 |
| 5. 5. 3 Raman spectroscopy analyses of WO_3 film..... | 73 |
| 5. 6. 0 Electrochromic device analyses..... | 75 |
| 5. 7. 0 Conclusions and future works..... | 77 |
| Chapter 6..... | 78 |
| New three dimensional graphene composite materials with high specific surface area for energy storage..... | 78 |
| 6. 0. 0 Reduced graphene oxide composite for energy storage..... | 78 |
| 6. 1. 0 Results and analyses..... | 80 |
| 6. 1. 2 Discursions of reduced graphene oxide..... | 82 |

| | |
|--|-----|
| 6. 2. 0 Nickel sol gel as suspenders for reduced graphene oxide | 85 |
| 6. 2. 1 Introduction and experimental..... | 85 |
| 6. 2. 2 Analyses of highly porous graphene oxide..... | 86 |
| 6. 2. 3 Results of highly porous graphene oxide..... | 86 |
| 6. 3. 0 Powder graphene sol gel | 89 |
| 6. 3. 1 Experimental..... | 91 |
| 6. 3. 2 Analyses of powder graphene sol gel..... | 90 |
| 6. 4. 0 Multilayer porous graphene films for gas sensors | 95 |
| 6. 4. 1 Experimental..... | 95 |
| 6. 4. 2 Analysis of the graphene film (mesh)..... | 96 |
| 6. 5. 0 Conclusions | 97 |
| References | 102 |
| Appendix | 116 |

Lists of figures

| | |
|--|----|
| Figure 1.1 mechanical exfoliation of graphene..... | 6 |
| Diagram 1.1 Chemical vapor deposition system..... | 7 |
| Figure 1.2 Chemical exfoliation of graphite..... | 9 |
| Figure 2.1 Field emission scanning micrographs of polystyrene spheres (PSS)..... | 15 |
| Figure 2.2 Field emission scanning electron micrographs of different sizes of PSS..... | 16 |
| Figure 2.3 Field emission scanning electron micrographs of Ni IOs domains..... | 17 |
| Figure 2.4 Large area field emission electron micrographs of Ni IOs..... | 18 |
| Figure 2.5 FE-SEM domain of graphene inverse opals (GIS)..... | 19 |
| Figure 2.6a &b Large area FE-SEM micrographs of GIS..... | 20 |
| Figure 2.7 Raman spectra of GIS..... | 23 |
| Figure 2.8 XRD analyses of GIS and Ni IOs..... | 24 |
| Figure 2.9 EDX analyses of etched GIS..... | 25 |
| Figure 3.1 Synthetic pathway for carbon nanotubes from Fe-IOs..... | 32 |
| Schematic 3.2 Synthetic pathways for carbon nanotubes forest and CNTs-IOs..... | 33 |
| Figure 3.3 FE-SEM micrographs of carbon nanotubes forest..... | 35 |
| Figure 3.4 FE-SEM micrographs of Fe-CNTs-IOs..... | 36 |
| Figure 3.5 Printing contact micrographs..... | 38 |

| | |
|---|----|
| Figure 3.6 FE-SEM micrographs of CNTs-IOs..... | 39 |
| Figure 3.7 XRD, UV-Vis and Raman analyses of CNTs-IO..... | 40 |
| Figure 3.8 FE-SEM micrographs depicting stability..... | 41 |
| Figure 4.1 Synthetic schematic of MnO ₂ -IOs..... | 44 |
| Figure 4.2 FE-SEM micrographs of MnO _x -IOs..... | 47 |
| Figure 4.3 Electrochemical exfoliated MnO _x -IOs nanosheets..... | 48 |
| Figure 4.4 Electrochemical exfoliation of bulk MnO _x nanosheets..... | 49 |
| Table 4.1 Atomic absorption analyses of oxidation state of Men..... | 50 |
| Figure 4.5 XPS elemental analyses..... | 52 |
| Figure 4.6 FE-SEM analyses of thickness of MnO ₂ -IO scaffolds..... | 53 |
| Figure 4.7 XRD, UV-Vis and Raman analyses of MnO ₂ -IO nanosheets..... | 56 |
| Diagram 5.1 chemical deposition system of WO _x | 63 |
| Figure 5.0 FE-SEM micrographs of WO _x Nano rods..... | 64 |
| Figure 5.1 FE-SEM thickness of the deposited WO ₃ film..... | 67 |
| Figure 5.2 FE-SEM micrographs of WO ₃ top view..... | 69 |
| Figure 5.3 XRD analyses of WO ₃ | 70 |
| Figure 5.4 Raman analyses of WO ₃ | 71 |
| Figure 5.5 Raman analyses of bilayer graphene..... | 72 |

| | |
|--|----|
| Diagram 5.2 Frame work of electrochromic device..... | 74 |
| Figure 5.6 Electrochemical analyses of WO ₃ device..... | 75 |
| Table 6.1 Relationship between technology and capacitance..... | 79 |
| Figure 6.1 Synthesized graphene oxide..... | 79 |
| Figure 6.2 Porous reduced graphene oxide scaffolds..... | 80 |
| Figure 6.3 Capacitance analyses of reduced GO..... | 82 |
| Figure 6.4 Raman and FE-SEM micrographs of rGO..... | 85 |
| Figure 6.5 EDX and XRD analyses of PrGO..... | 86 |
| Figure 6.6 Capacitance of PrGO..... | 87 |
| Figure 6.7 FE-SEM micrographs of powder graphene sol gel..... | 90 |
| Figure 6.8 Raman and EDX analyses of graphene sol gel..... | 91 |
| Figure 6.9 XRD analyses of graphene sol gel..... | 92 |
| Diagram 6.1 chemical vapor deposition system for graphene sol gel..... | 94 |
| Figure 6.10 FE-SEM micrographs of thin film graphene..... | 95 |
| Figure 6.11 EDX and Raman analysis of graphene thin film..... | 96 |
| Figure 6.12 FE-SEM and XRD analyses of graphene thin film..... | 97 |

Acknowledgements

From the depth of my heart, I want to thank my adviser Dr. Alexander Sinitskii for his tremendous support, advised and encouragement. Thank you Dr. Alexander Sinitskii. You have been the catalyst behind my success. I will also want to thank Dr. Rebecca Lai my co-adviser for her kind intelligent support and encouragement. All the members of my advisory committee Dr. Alexander Sinitskii, Dr. Rebecca Lai, Dr. Barry Cheung, Dr. Jian Zhang and Dr. Alexei Grouverman for all your support. I thank Thomas Smith who did most of the electrochemical analyses for his candid collaborations in this project. My Lab mates Peter Wilson for his collaboration and the group in general for their tolerance. If I were asked who are you? I'll say you all have been the source of my inspiration and motivation.

I want to acknowledge the University of Nebraska-Lincoln, department of chemistry for the opportunity given to me.

Thank you and May the Almighty God bless and protect you.

Dedication

First, I would like to thank Almighty God who has given the privilege to be alive and to study at an advanced level. I want to shout a big thank you to all the people that I have encountered in my academic journey: Dr. Kristy Mardis, Dr. Kanis David and Dr. Robert LeSuer for their advice, encouragement and support. I dedicate this work to my late lovely father Ndamukong Godlove Mbah (God blessed his memories) and my dear-sweet mother Mungweri Grace Mbah for their persistent support especially when it seems impossible. I want you to know that the sacrifices you made for me toward my education cannot and will not be forgotten. You sacrificed the only kerosene lamb for me to study while you remained at the mercy of kitchen fire. I want to thank my older sisters Clementine Tar and Henrietta with their families for being there when I needed a family. Thank you to my twin brother, Edwin Aneng Mbah for standing strong for the family when I could not. Thank you to my wonderful family for their understanding and perseverance through the dark and bright moments. May the Almighty God continue to bless, protect, guide and inspire you all. You are a true family and I'm blessed to have you as my family.

I will never forget your support and I pray God our relationships continue to growth in the Love of God as we treat for each other.

God has given all I have and I owe it to him in sharing with others.

Chapter 1

Introduction

Gordon Moore the co-founder of Intel predicted in 1965 that the numbers of integrated transistors per circuit will continue to double⁵. This prediction is now known as Moore's law and is the mainframe, per-transistor performance, cost scaling that has ushered into nanotechnologies of total integrated systems⁶ Silicon, a semiconductor with a tunable indirect band gap, exhibits suitable operating temperature range of -55 to 125°C, and low current leakages. Silicon transistors stand out over germanium transistors that exhibit poor operating temperatures¹⁻³, high current leakages (screw dislocation), low power, low current gains and low operating frequencies. Silicon chips with the best technology have shown to be the safest material for integrated transistor circuits⁷. In respect to other semiconductors, silicon is a cheap, abundant material and has advanced technology that makes silicon suitable for integrated transistors and untouchable⁸. Over the past decade, silicon integrated transistors have double but the decrease in the size of transistors is a treat to the future of silicon transistors. The limitation of silicon technology (top-down synthesis) and physical properties of silicon is the problem for scientist and engineers to continue sizing down the size of integrated transistors⁹.

To keep pace with the demand for small size electronics, energy storage and sensor devices, engineers are turning to new materials that can substitute silicon. Few nanometer-thick silicon film have been synthesized for integrated transistors¹⁰. The diamond cubic crystals structure of silicon and the limitations offered by technology (wavelength of the laser, size of tools) makes it harder to synthesize atomic layer thin

film of silicon for device fabrications^{5,6-11}. Thin film silicon and one-atomic layer thick silicon and phosphorus have been studied as the alternative material^{12,13-14}. Scientific communities have hypothesized the need for a single layer semiconductor. In 2004, Geim and Novoselov demonstrated that graphene a two dimensional one atomic layer material has the potential to replace silicon in integrated transistors⁴⁻¹⁵. A lot has been done to bridge the gap between graphene and silicon in integrated transistors¹⁶. Much still have to be done to replace silicon with graphene¹⁷⁻¹⁸. The applications of graphene into integrated transistors, energy storage, sensors and biological engineering are overwarming¹⁹⁻²⁰.

1. 1. 0 Study of Graphene

Graphene, a two-dimensional hexagonal lattice structure and one atomic layer thick, is an allotrope of carbon. Graphene is the building block of graphite, carbon nanotubes, fullerene and charcoal²¹. Graphene is made up of sp^2 hybridized carbon atoms that are connected in a hexagonal pattern. Graphene also known as a miracle material because of its extraordinary properties make graphene an applicable material across wide fields. Graphene exhibits extremely high electrical and thermal conductivity²²⁻²³ high tensile strength (high modulus constant) by unit mass²², high thermal stability²⁴⁻²⁵ and high transparency²⁶. Some of graphene's applications include biological, electronics, medicine, light photodiode, energy storage, sensors and environmental applications^{5,27-28}. The effective properties of graphene are attributed to the Dirac band structure and the in plane conductivity of graphene²⁹.

1. 1. 1 Applications of Graphene

Graphene's lightweight, atomic layer thick, high conductivity, flexibility and durability make it applicable to the environment, sensors, health, electronics^{15,30}. High mechanical stability of graphene, low reactivity (inert), transparency and conductivity make graphene suitable for light processing applications, screens displays, electric circuits, sensors and solar cells²⁷.

1. 1. 2 Graphene for Electronic devices

The zero-band gap of graphene makes graphene more of a metallic material than a semiconductor. Graphene is known as the lightest material that exhibit a Dirac fermions level band gap⁴. The Dirac band structure of graphene and its aromaticity (delocalized electrons) contribute to the high electrical conductivity of graphene by modulating the electronic state of graphene around the Fermi level³¹⁻³². Graphene exhibit high charge carrier mobility suitable for fast integrated transistors but are hindered by their zero band gap^{18,27-28}. Engineering graphene nanoribbons and graphene composite materials are the alternate ways to improve on the quality and quantity of graphene band gap semiconductor³³.

1.1.1 Graphene for Sensor devices

Combustible, flammable, toxic, Oxygen depletion and unwanted gases have been known to cause unnecessary fire hazards to both lives and properties. Gas sensors are used in every environment namely homes, institutions and companies to avoid fire or suffocation from poisonous gases like carbon monoxide^{15,34}. The high electrical, inert and thermal conductivity of graphene make this material highly sensitive to doping. Different gases exhibit unique finger print signal (reversible doping) over graphene substrate and can be used to determine their presence or absence. Graphene gas

sensors function via molecular adsorption, piezoelectric effect, photovoltaic cells and body motion generating unique signal^{34,35-36}.

1. 1. 3 Graphene for energy storage devices

Transition metal oxides and hydrides have been used over the century as energy storage devices³⁷. Cost, weight, toxicity, hazards and low power density are the common factors that plague transition metals oxides and hydrides in energy storage devices^{31,37-38}. Transition metal oxides and hydrides devices exhibit high energy density with medium power density. Manganese and nickel oxides (hydrides) have been studied and are used as energy storage materials because of their reactivity, abundant, low toxicity and high activity³⁹⁻⁴⁰. Metal oxides and hydrides are heavy and expensive as such are not suitable for lightweight-pocket devices⁴¹⁻² making graphene metal oxide composites an advantageous material for energy storage devices⁴⁰⁻⁴².

High conductivity, specific surface area, thermal stability and mechanical stability have shown that graphene could be the best material for energy storage devices⁴³. Graphene has been used in lithium-ion batteries⁴⁴⁻⁴⁵, catalytic material in fuel cells⁴⁶ and as a material in supercapacitors devices^{47,48,49,50-51}. The mechanical exfoliation synthetic method of pristine graphene has been questionable since 2004 for large scale production. Different novel methods to synthesize graphene have been discovered and implemented. There are three main synthetic methods of graphene fabrication but with low efficiency and productivity. Single to few layers of graphene are synthesized via chemical vapor deposition or mechanical exfoliation of graphene⁴⁻⁵² and bulk graphene can be synthesized via chemical exfoliation of graphite^{50,53,54,55-56}. Chemical exfoliation of graphite yields three dimensional (bulk) graphene oxide material with low conductivity,

low specific surface area, high reactivity, and low thermal stability^{49,54,56}. Theoreticians predicted that three dimensional highly connected pristine graphene will generate high efficient energy storage devices¹⁶. Here, we present a technological pathway to synthesize bulk, high quality three dimensional pristine graphene for energy storage devices and sensors.

1. 1. 4 Graphene for biomedical devices

High mechanical, inert and conducting graphene composite materials have demonstrated that graphene improved biomedical devices⁵⁷⁻⁵⁸. Tissue engineering, drug delivery, polymer chain reaction, bio-imaging and sensor devices are all sectors in biomedicine that requires high quality graphene to improve their efficiency²³. Doped or functionalized graphene oxides have changed both physical and chemical properties of graphene creating both positive and negative effects on its applications^{58,59-60}. Our well coin synthetic method of 3D graphene will be of paramount importance to vast applications including bioengineer materials.

1. 1. 5 Graphene for light processing devices

Single, bilayer and few layers of graphene exhibit different transparencies and absorbed visible light over wide spectrum⁶¹⁻⁶². Graphene doped with metal oxides have shown to open a band gab making the material a semiconductor suitable for photodiode and transistors applications⁶³⁻⁶⁴. Doping graphene has also been demonstrated with metal oxides graphene composites material for batteries. Single layer graphene exhibit poor absorption spectrum of visible light applicable for photodetectors. Graphene hybrid

materials have been synthesized (doping) as the composite material to absorb light over specific wavelengths⁶⁵⁻⁶⁶.

1. 2. 0 Synthesis of Graphene

Graphene was first synthesized via mechanical exfoliation of graphite using scotch tape⁴(scotch tape graphene). The urge to utilize graphene for the different applications drove the need for cheaper, easier and faster techniques to synthesize graphene in bulk. Chemical exfoliation of graphite and chemical vapor deposition (CVD) in addition to mechanical exfoliation are the main routes used to synthesize graphene. Chemical exfoliation is cheap, time efficient and high yield (bulk) graphene⁵⁶ compared with CVD technique that is low yield but high quality graphene⁵⁵. Our work utilized chemically exfoliated graphene and CVD of graphene technologies to coin new materials.

1.2.1 Chemical exfoliation of graphene oxide.

Pristine graphene was first synthesized via mechanical exfoliation⁴. This technique can produce single, bilayer, three layers, and few layers of graphene. Analyses of the synthesized graphene single to few layers graphene depend mostly on chance. The size and shape of graphene flakes synthesized via scotch tape technique cannot be controlled. Mechanical exfoliation of graphene demands intensive labor to identify the exfoliated graphene flakes on transfer silicon dioxide wafer using optical microscopes. The contrast between single, bilayer and few layers of graphene on silicon dioxide wafer are visible under optical microscope⁶⁷. The exfoliated flakes are confirmed using Raman spectroscopy analyses. The schematic below demonstrates the necessary steps taken during mechanical exfoliation of graphene from graphite. Bulk graphene cannot be synthesized via mechanical exfoliation creating the need for new, robust and

versatile technologies to synthesize high quality pristine graphene suitable for field effect transistors and related applications.

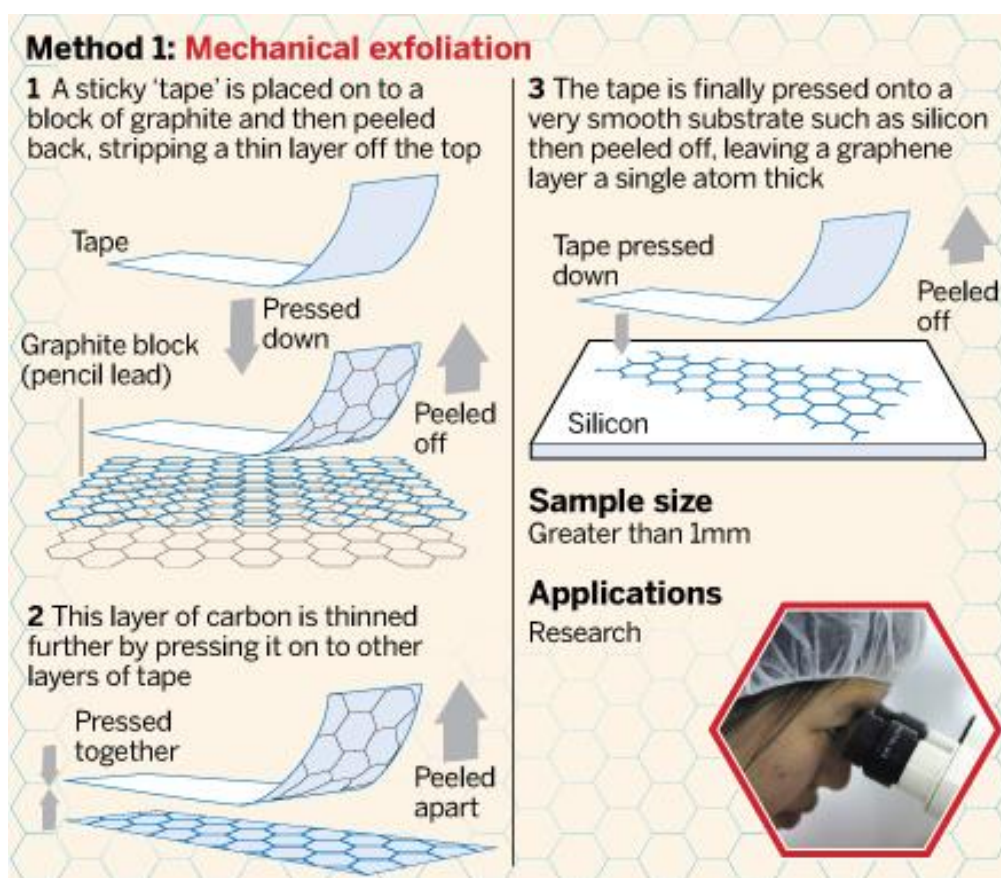


Figure 1.1. Schematic diagram illustrating the mechanical exfoliation of single layer to few layers graphene using scotch tape⁶⁸.

Low yield of graphene using scotch tape technique has led to chemical exfoliation of graphene and chemical vapor deposition of graphene as the dominant methods used to synthesize graphene.

1. 2. 2 Chemical vapor deposition of graphene

The origin of chemical vapor deposition technique has not been well defined. According to Powell, Oxley and Blocher in their book, Michael Faraday used chemical vapor deposition (CVD) technology in 1838 to synthesize a thin-film coating⁶⁹. The quality of any material synthesized via CVD is determined by the pressure of the reactor, rate of mass flows of the precursors (gas controller), thermodynamic or the kinetics of the precursors and the reaction rate (temperature controllers)⁷⁰. We used low pressure chemical vapor deposition (LPCVD or CVD) system in our research. LPCVD prevents unwanted gas-phase reactions from occurring and improve film uniformity via suitable mass flow conditions. The diagram 1.1 below depicts the CVD system used in this research

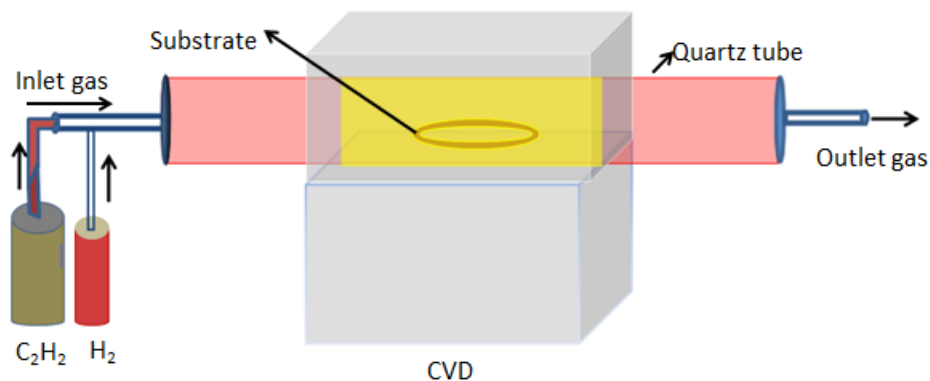


Diagram 1.1. Schematic representation of low pressure chemical vapor deposition

Acetylene (chapter 2, 3 & 6) and methane (chapter 5) were the main carbon precursors used for our graphene syntheses with hydrogen as the etching reagent and argon used as carrier gas and annealing condition. Methane requires higher temperature because of its low reactivity compared to acetylene that reacts at lower temperatures. The reactor is set-up as shown in diagram 1 above with the substrate inserted inside the

quartz via one of the open ends. The system was connected to a particular carbon source determine by the substrate. Both copper and nickel substrates were used to synthesize graphene. Single or bilayer layers graphene were grown on copper^{50,71} and few layers graphene were grown on nickel foil substrate⁵⁰.

1. 2. 3 Chemical exfoliation of graphite

Functionalized graphene oxide was first synthesized by Brodie in 1859 by repeatedly treating graphite in strong oxidizing agent and fuming nitric acid. In 1957, Hummer and Offeman modified the synthetic method using potassium permanganate in sulfuric acid and phosphoric acid now known as the Hummer's method⁵³. The acid intercalates between the graphitic sheets expanding graphite and accessible to oxidation by the oxidizing agent (potassium permanganate). Phosphoric acid is believed to reduce the degree of oxidation but not much has been done to support or dispute this claim. Figure 1.2 below illustrates the steps taken in the functionalization of graphite to graphene oxide. 30mg of graphene was poured into a solution of pure sulfuric acid and phosphoric acid (100mL) and stirred for 5 minutes at room temperature. The beaker and content immersed into an ice bath and 50mg of potassium permanganate added gradually keeping the temperature below 70°C. After 2 hours of stirring, the mixture turn light purple and 30mL of 1M hydrogen peroxide added drop wise to terminate oxidation. The product filtered, washed with deionized water and dispersed in water or acetone as brown solution.

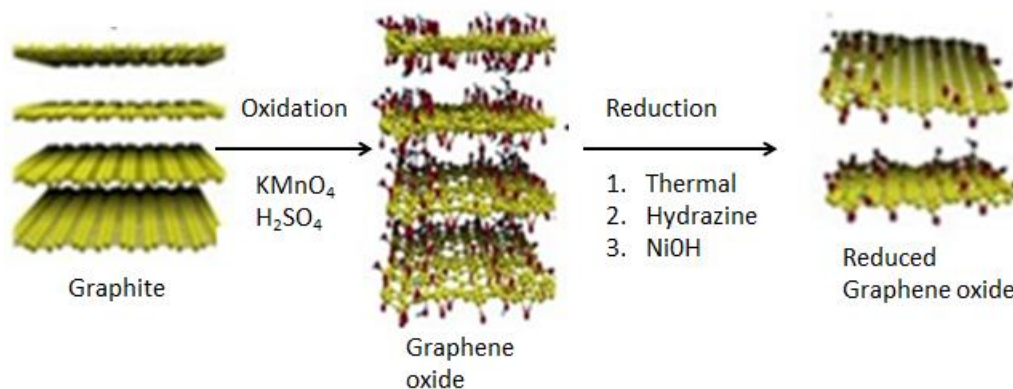


Figure 1.2. Schematic diagram for the oxidation of graphite using modified Hummer's method⁷².

Instead of using the modified Hummer's method, we re-modified the method to synthesize graphene oxide by eliminating phosphoric acid. In chapter 6, we present the cheaper way to synthesize graphene oxide nanosheets from graphite and potassium permanganate in pure sulfuric acid.

Chapter 2

Three dimensional microporous architecture of highly connected graphene inverse opal scaffolds

2. 1. 0 Introduction

Two-dimensional graphene materials have shown high prospects for semiconductor industries⁷³. Mechanical exfoliation is the best technique to synthesize high quality pristine graphene from graphite²². CVD and chemical exfoliation have been well studied as the alternate methods but yield poor quality graphene with low charge mobility. The quest for pristine graphene to substitute silicon in chips has gained steam with researchers shaping graphene into nanoribbons with expanded band gap for integrated transistors^{16,74-75}. Though progress is being made every day to improve the quality of single layer graphene for transistors, not much has been done to develop direct, easy and cheap technology to synthesize three dimensional (3D) and well connected graphene materials with improve properties for vast applications including transistors, energy storage and sensor devices. Here, we present an easy, direct, cheap, safe, scalable and reproducible technology to synthesize high quality 3D graphene scaffolds. The synthesized 3D graphene scaffolds known as graphene inverse opals have applications ranging from energy storage devices to sensor devices⁷⁶.

CVD of graphene on catalytic metal substrates such as copper, nickel, Indium, platinum, rhodium, silicon and titanium⁷⁷⁻⁷⁸ has been well documented and growth of graphene shown to mimic the architecture of the substrate⁷⁹. Our synthetic method required a pre-synthesized 3D metal architectural scaffold of nickel^{15,50,76}.

2. 2. 0 Experimental

Reagents: Nickel (II) chloride, nickel sulfate, ethanol, styrene, acetylene, hydrogen gas, argon, dry ice, boric acid, styrene, potassium persulfate, acetone, toluene, sodium hydroxide, highly oriented pyrolytic graphite, nickel foil and copper foil. All reagents were purchased from sigma Aldrich.

Instrumentals: Two electrode power source, 3cm in diameter cylindrical container, CVD system, Raman spectroscopy, hot plate, electron microscopy, X-Ray diffraction spectroscopy and energy dispersion spectroscopy.

The mechanism of graphene growth on transition metals is influenced by the metal substrate. Catalysis and solubility of carbon at the metal surface and in the transition metals respectively determine the quality of graphene synthesis. Single layer graphene grown on copper requires a catalytic surface of copper⁸⁰ while graphene grown on nickel depends on solubility of carbon into the nickel substrate⁵⁵.

2. 2. 1 Synthesis of polystyrene spheres (PSS)

Polystyrene spheres were synthesized using the well-studied dispersion polymerization of styrene technology⁸¹. 1.0 M solution of sodium hydroxide (NaOH) was used to clean 50 mL of styrene. NaOH removed the inhibitor (dinitrophenyl (DNOC, DNBP, DNOP and DNP)) that prevents styrene from polymerizing under room temperature conditions⁸²⁻⁸³. The clean styrene was rinsed with 100 mL of deionize water three times. 300 mL of deionize water was heated at 70 °C in Erlenmeyer flask and 25 mL of potassium persulfate (PKS (0.2 moles)) was added under constant rotation of 300 rpm. The temperature stabilized after 1 minute of stirring at constant stirring rate. The stir plate was set at 300 rpm for the entire experiment. 20 mL of the clean styrene was added to the hot PKS solution at 70°C. The experiment ran for 2 hours at constant

temperature and stirring rate. Different PSS sizes were synthesized by changing the synthesized sets of parameters namely, the amount of clean styrene, temperature (60°C to 70°C)⁸²⁻⁸⁴, stirring rate and the amount of concentration of PKS initiator. Different sizes of PSS (180 up to 500 nm) were synthesized. The optimized process resulted into the best procedure to synthesize desired quality of PSS. We synthesized different sizes of PSS from 180 nm to 600nm in diameter by changing the concentration of PKS with respect to clean styrene.

Table 2.0 Different sizes of synthesized PSS under different conditions

| Size of PSS (nm) | Stirring rate (rpm) | Temperature (C) | Concentration of PKS (25 mL moles) | Concentration (volume mL) |
|------------------|---------------------|-----------------|------------------------------------|---------------------------|
| 180 | 300 | 60 | 0.05 | 10 |
| 200 | 300 | 65 | 0.2 | 15 |
| 300 | 300 | 70 | 0.2 | 22 |
| 500 | 300 | 70 | 0.2 | 30 |

2. 2. 2 Electrochemical depositions of nickel inverse opals

The well-developed self-assembly technique of PSS was employed to synthesize 3D PSS template⁸⁵. 3 g/mL of the synthesized PSS solution were prepared by dispersing PSS in 50 mL deionize water at room temperature. Strips of copper foils that were cleaned in acetone, then in acetone/ethanol solution and ethanol were vertically aligned in a 100 mL beaker. The PSS solution was poured gently into the 100 mL beaker containing copper foil strips and stored in the oven at 50°C overnight⁸¹. The copper

strips were obtained with self-assembled PSS on them for electrochemical deposition of nickel.

A solution of nickel (II) nitrate (3g/mL), nickel (II) chloride (2g/mL) and boric acid (0.2moles) was prepared in a 10:1ratio solvent (deionized water and ethanol) respectively. A voltage source (two electrode system) was used to electrochemically grow nickel within the interstitial spaces of the self-assembled PSS scaffold on copper foil strips. 0.5volts were used to deposit (by infiltration) nickel on the copper substrate containing self-assembled PSS. Copper foil was mounted at the cathode and highly oriented pyrolytic graphite (HOPG) was mounted at the anode⁸⁶. The nickel solution was gently transferred into the 100 mL PET cylinder set-up with HOPG vertically inserted and the cathode strips as the based. The experiment ran for 30 minutes under constant voltage. The experiment was repeated several times to generate continuous usable nickel inverse opal substrates. The set up was unassembled and the infiltrated PSS with nickel substrate obtained and dried in the oven at 50°C for 30 minutes. The infiltrated electrodeposited nickel substrates were inserted into toluene to leach out PSS for 10 minutes. The nickel inverse opal substrates obtained served as the sacrificial metal architectural templates for the fabrication of graphene inverse opals.

2. 2. 3 Syntheses of graphene inverse opals

The synthesized nickel inverse opals were dried for 30 minutes in the oven at 50°C. The nickel inverse opals were inserted into a CVD reactor chamber at room temperature and vacuum pump to 10mtorr. The temperature gradient of the CVD system was programmed to increase at 10°C per second up to 500°C. Temperature gradient, annealing temperature, growth temperature, precursor sources, and flow rate of the gas

precursors were all studied to determine the best condition for the growth of graphene-nickel inverse opal scaffolds. The synthesized nickel inverse opals coated with graphene was at 500°C for 30 minutes under 0.5 sccm of C₂H₂ and 3 sccm H₂ gas after annealing for 15 minutes in 2 sccm of H₂ gas as the etching gas. Reduction of nickel oxide to nickel was done at 500°C for 30 minutes under hydrogen gas. The CVD system was slowly cooled down to room temperature by turning the furnace off. The cooling down process allowed the dissolved carbon into nickel to precipitate out of the nickel coating the entire nickel scaffold with graphene. The nickel inverse opal graphene were spin coated with polymethylmethacrylate (PMMA) and cured at 180°C on hot plate for 90 seconds. The copper strips with nickel inverse opals coated with graphene were transferred onto acidic iron (III) chloride solution. The copper nickel architecture frame works were etched away leaving graphene inverse opal coated with PMMA suspended on the acidic iron (III) chloride solution. The synthesized graphene inverse opals were fished out using cleaned silicon dioxide glass substrate onto deionize water. The process was repeated three times changing used the deionize water each time to ensure complete removal of residual metal ions such as iron, nickel or copper^{28,77}. The cleaned graphene inverse opals were transferred onto 1.0 M hydrochloric acid solution for 20 minutes to completely dissolve unwanted metal oxides on the graphene film. The samples were then fished out with silicon dioxide wafer dried at 30°C for 5 minutes. The SiO₂ wafer with graphene inverse opal was inserted in acetone solvent to dissolve the PMMA. Free standing 3D highly connected graphene inverse opals on SiO₂ wafers were dried at room temperature for few minutes before analysis and characterization.

2. 3. 0 Analysis of the synthesized graphene inverse opals

Field emission scanning electron microscopy (Hitachi S4700 Field-Emission SEM), X-Ray diffraction spectroscopy (Rigaku Multiflex Diffractometer, Cu K α wavelength), Energy dispersive X-ray spectroscopy (Nova NanoSEM/FEI) and Raman spectroscopy was used in the analyses process.

2. 3. 1 Analysis of the synthesized polystyrene spheres

The synthesized PSS (white solution) were dropped casted on silicon dioxide wafer dried in the oven at 50°C for 30 minutes followed by field emission scanning electron microscopy (FESCM or SEM) analyses. The SEM micrographs were used to determine the size, uniformity and quality of the synthesized PSS. The uniformity of the self-assembled PSS (cracks free) was influenced by the thickness (concentration of PSS), rate of evaporation of the solvent and the surface tensional forces between the solvent and the substrate (stress). The process was optimized by changing the concentration of PSS and rate of evaporation of the solvent. Large areas of thin film of PSS (cracks free) has been self-assembled on centimeters scale on glass substrate^{81,87}. Figure 2.1 below depict the thickness and cracks caused by stress of the self-assembled PSS on copper substrate.

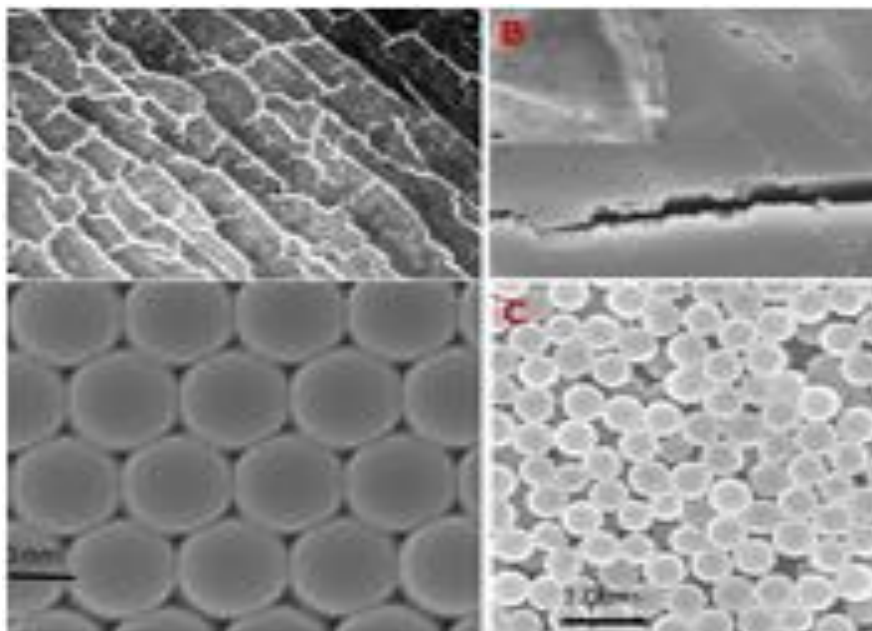


Figure 2.1. Field emission scanning electron micrographs of the self-assembled synthesized polystyrene spheres on copper strips. Images (a, c & d) are the top view of PSS at different magnifications and (b) depict the thickness of the self-assembled PSS on the substrate.

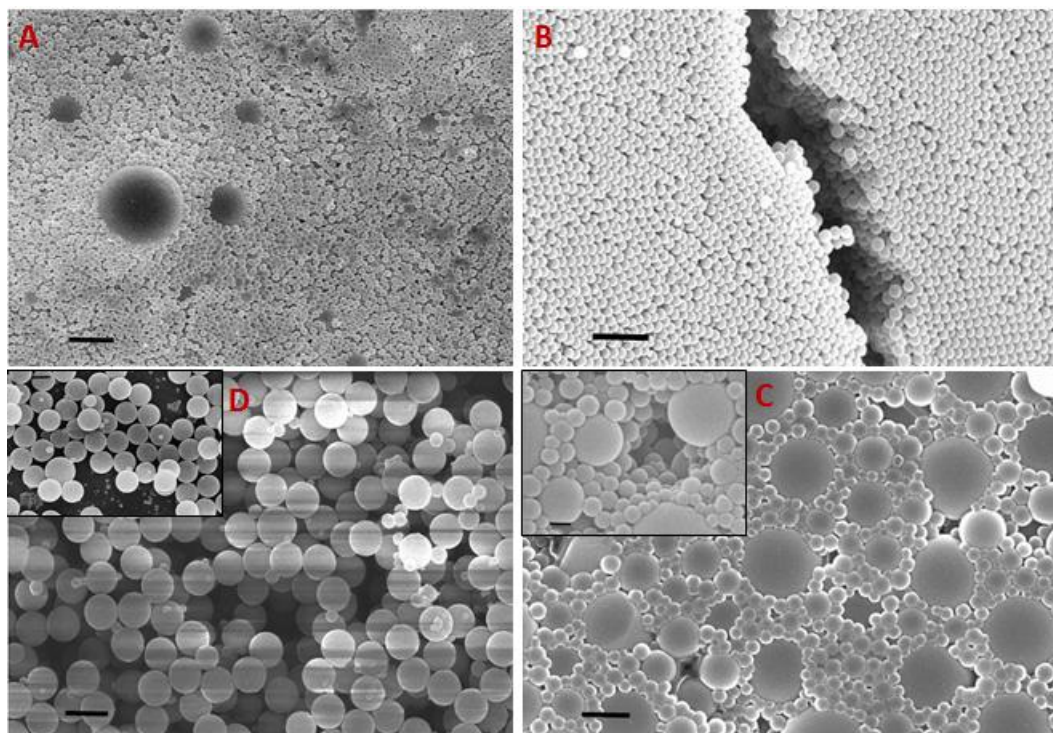


Figure 2. 2. Scanning electron micrographs depict the different sizes of PSS synthesized under different conditions. (a) SEM image of PSS synthesized at altered stirring rate, (b) SEM image of PSS synthesized at optimized synthetic conditions, (c) SEM image of PSS at both stirring and initiator altered conditions and (d) SEM image of PSS at altered temperature and stirring rate conditions.

2. 3. 2 Analysis of electrodeposited Nickel inverse opals

The synthesized nickel inverse opals were analyzed with both Field emission electron microscopy (SEM) and X-Ray diffraction (XRD) technologies. The SEM images in figure 2.3 below support the successful fabrication of nickel inverse opal scaffolds. XRD spectrum in figure 2.6 also confirmed that the synthesized Nickel inverse opals frame works were nickel metal. The qualities and quantities of the synthesized graphene inverse opals were all reflections on the quality as well as quantity of the pre-synthesized

nickel inverse opals scaffolds (domain sizes). Figure 2.3 below illustrate the effect of low quality nickel inverse opals influenced by the poor quality of self-assembly of PSS.

Figure 2.4 depict the large area nickel inverse opals obtained from the optimized self-assembled PSS template.

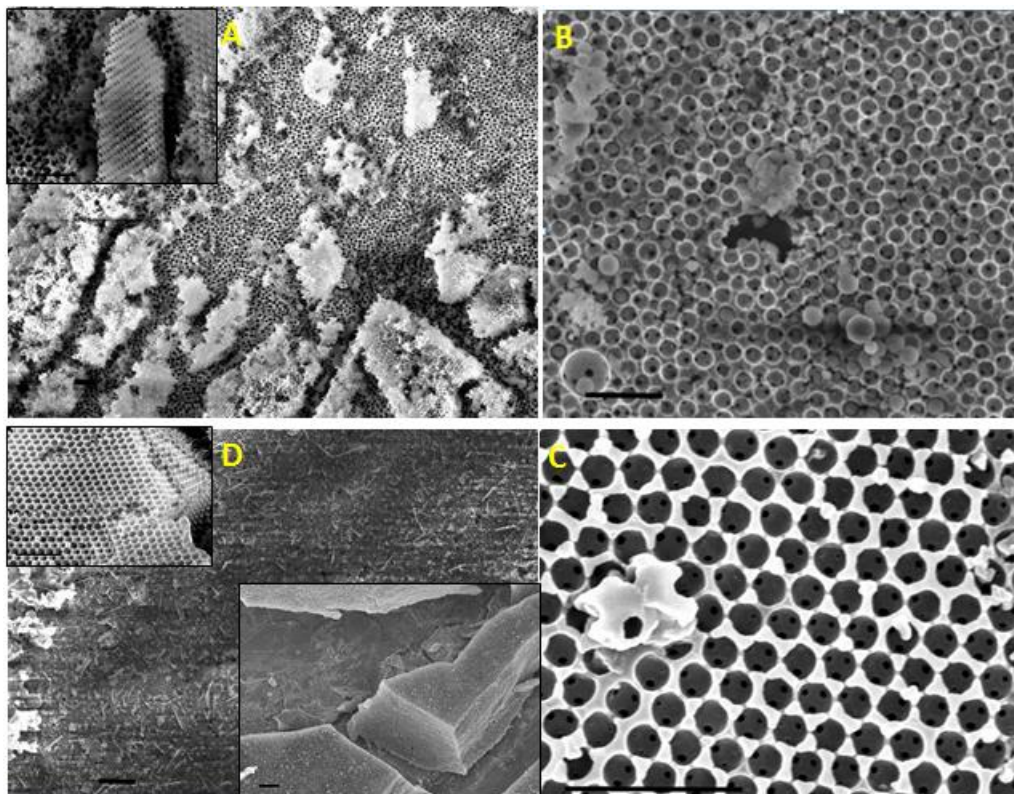


Figure 2.3. Field emission scanning electron microscopy micrographs above illustrates poor quality nickel inverse opals (Ni IOs) synthesized from poor self-assembled PSS. The scale bar for all the micrographs is $2\mu\text{m}$. (a) SEM micrograph of Ni IOs top-view at low magnification, (d) SEM micrographs of Ni IOs side-view and (b & c) SEM micrographs of top-view at high magnification.

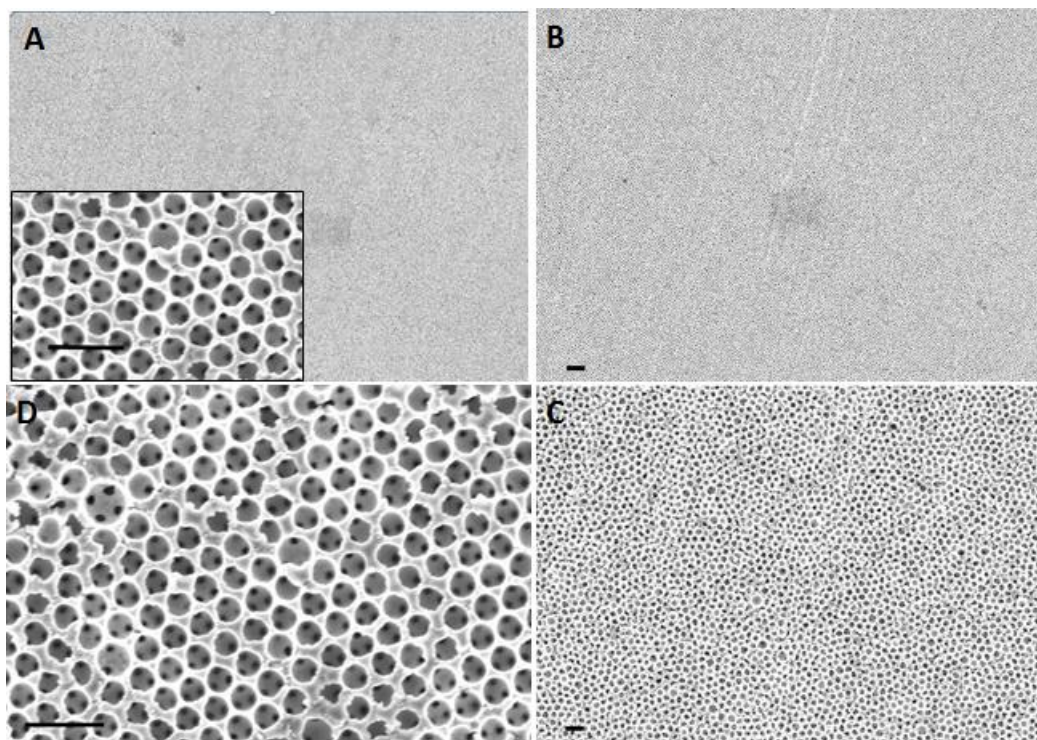


Figure 2.4. SEM micrographs of high quality nickel inverse opals synthesized from good self-assembled PSS. The scale bar of nickel inverse opals is 2 μm . (a) SEM images of Ni IOs top-view at low magnification and (b,c, & d) SEM micrographs for Ni IOs top-view obtained at different magnifications.

The large scale synthesized nickel inverse opals were obtained from the optimized self-assembly technique of uniform large area (cracks free) PSS on copper foil.

2. 3. 3 Analyses of the synthesized graphene inverse opals scaffolds

The synthesized graphene inverse opals (GIOs) were etched and transferred onto silicon dioxide wafer for SEM analysis. Figure 2.5 below are the SEM micrographs of GIOs synthesized from poor quality Ni IOs (figure 2.3 above) because of low quality self-assembled PSS template on copper strips. The domain sizes of GIOs determined by the sizes of PSS domains on copper as shown in figure 2.1 are clear indication of the finger

print left of metal substrate on CVD graphene. Research have shown that cracks occurred during self-assembly because of stress, temperature gradient, surface tension, adhesive forces and thickness of PSS on the (copper) substrate⁸⁸. Figure 2.5 on the other hand depicted that large area GIOs can be synthesized from large area uniform cracks free self-assembled PSS on copper strips by controlling the above factors.

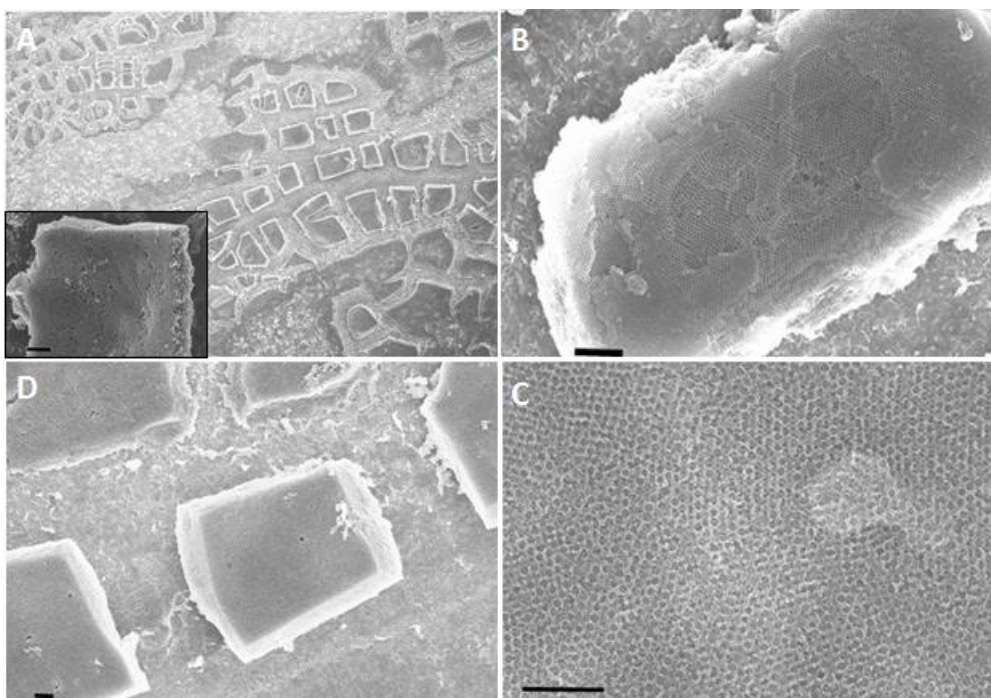


Figure 2.5. Field emission scanning electron micrographs of free standing graphene inverse opals displayed the different domains and thicknesses of GIOs. (a) SEM image of top-view GIOs on silicon wafer at low magnification (inserted micrograph at high magnification) and (b, c & d) SEM micrographs of top-view, side-view and top-view of GIOs respectively at different magnifications.

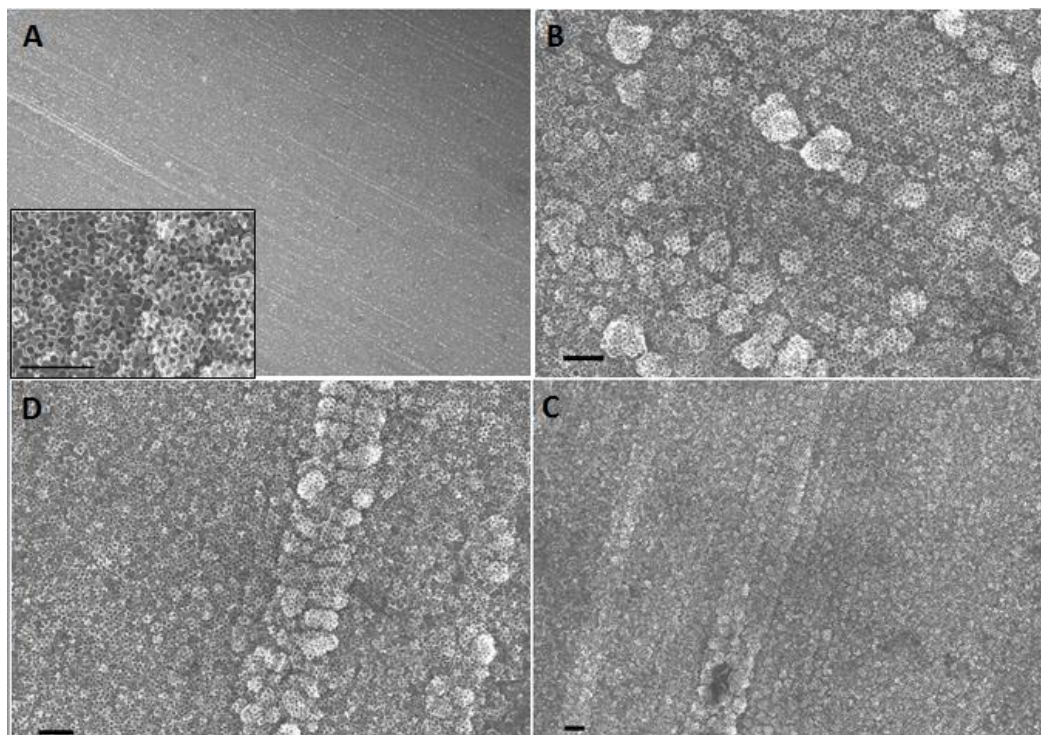


Figure 2.6a. Field emission scanning electron micrographs of large area three dimensional, free standing and cracks free pristine graphene inverse opal scaffolds. The quality of graphene inverse opal is uniform over 3cm in diameters. (a-d) SEM micrographs show top-view GIOs at low magnifications.

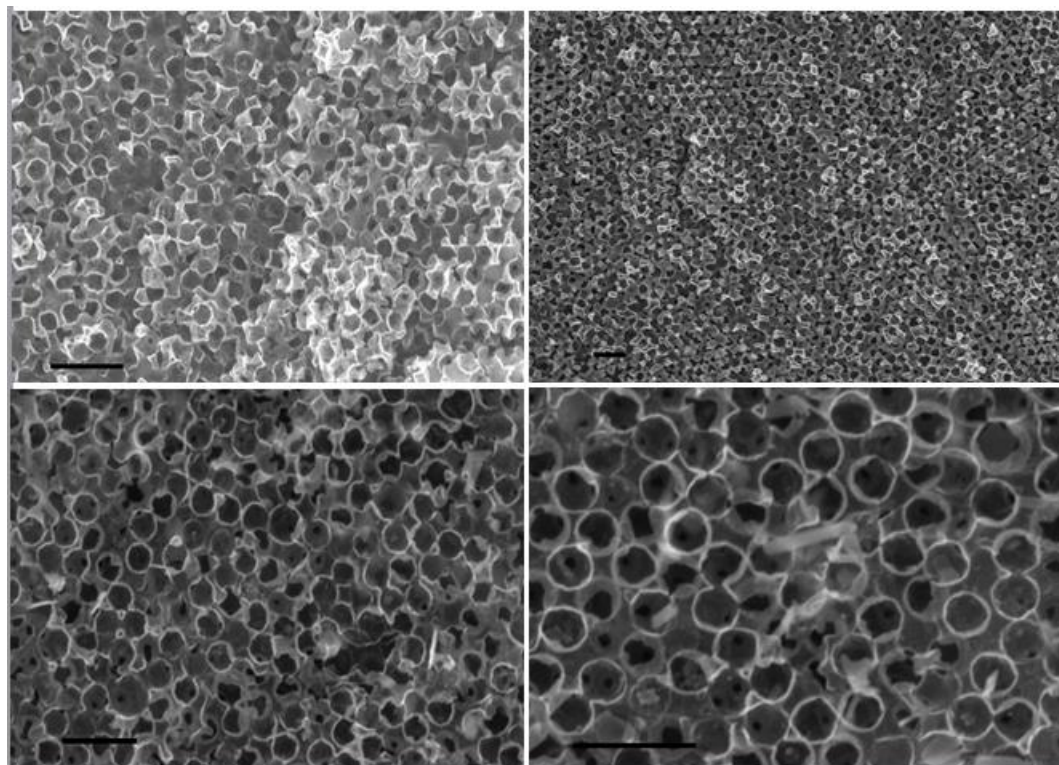


Figure 2.6b. Field emission electron micrographs of free standing graphene inverse opals (GIOs) synthesized from nickel inverse opals. Micrographs are top-view of GIOs obtained at high magnification compared to those in figure 2.6a (scale bar is $1\mu\text{m}$).

Field emission scanning electron micrographs shown above established that free standing 3D porous GIOs thin films can be transfer from one substrate to the next without damaging the physical structures. This is very important because its show the mechanical stability of the material and robustness of the material for different applications.

2. 3. 4 Raman spectroscopy studies of graphene inverse opals

Raman spectroscopy is the most efficient technology used in the characterization of graphene and graphene like materials. The spectrum of graphene (Graphite) has

characteristic two distinct peaks that occur at 1580 cm^{-1} (G-band) and 2650 cm^{-1} (2D-band) and small intense peak at 1350 cm^{-1} (D-band). The intensity ratio of 2D-band that occurs around 2650 cm^{-1} and the G-band that occurs around 1580 cm^{-1} is the characteristic testimony of the number of graphene layers present⁸⁹. The G-band is caused by the in-plane vibrations of sp^2 hybridized carbon within graphene sheet⁹⁰. Increased in the number of graphene sheets lead to increase in the number of sp^2 hybridized carbon as a result increases the intensity of the G-peak as shown. The 2D-band is the vibration signal of the out of plane vibration between the π and π^* orbitals. As the number of graphene layers increases the interaction between the π and π^* orbitals of one layer overlaps with that of the next layer. This overlaps interaction leads to decrease in the intensity with respect to the 2D-peak intensity of single layer graphene. The disorder or defect band (D-band) observed around 1350 cm^{-1} is the third most intense peak used to determine the quality of graphene. The peak is caused by the second order of zone boundary phonons which do not satisfy the Raman selection rule (breathing mode of sp^2 carbon rings)⁹⁰⁻⁸⁹. The Raman analyses as shown in figure 2.7 below compares peak intensities of single layer graphene to our synthesized graphene inverse opal scaffolds. This result predicts that our synthesized graphene inverse opals scaffolds are made up of multilayer graphene.

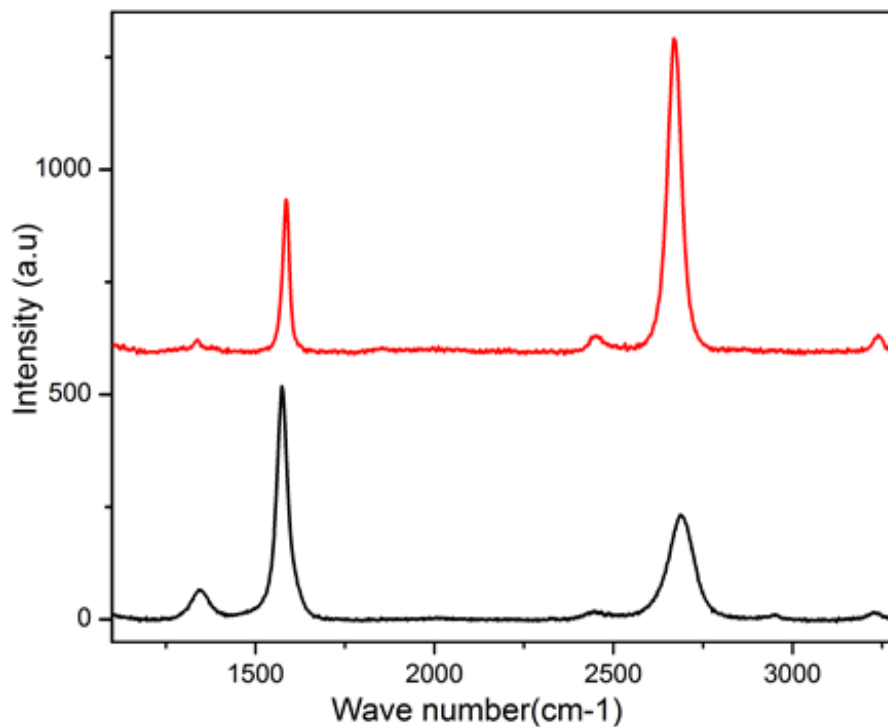


Figure 2.7. The Raman spectrum of CVD multilayer graphene inverse opals (black) and CVD single layer graphene grown on copper (red)

2. 3. 5 X-Ray diffraction analyses of graphene inverse opals

Graphite has been studied with XRD and exhibit a characteristic reflection peak at 25 degrees as a result of the (002) reflection plane. The synthesized graphene inverse opals were transferred onto a silicon dioxide wafer for XRD analysis. The XRD spectrum shown in figure 2.8 below with one broad single peak at 25 degrees confirmed that the synthesized material were graphene like material. The graphitic peak at 25 degrees has been attributed to π - π interaction⁹¹ between and within graphene sheets.

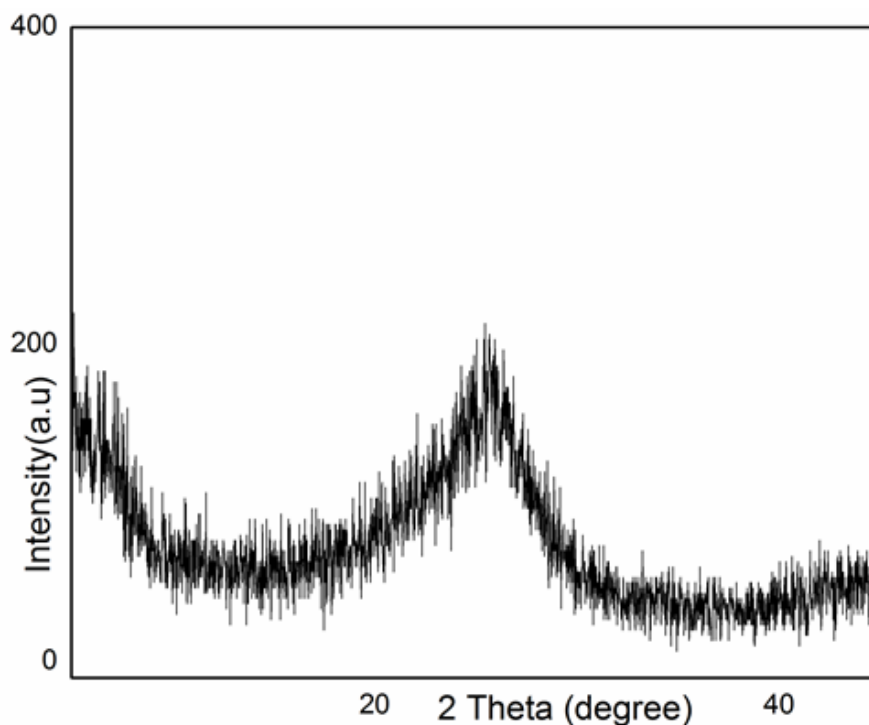


Figure 2.8. X-Ray diffraction spectrogram of graphene inverse opals indicates a strong graphitic peak at 25 degrees.

2. 3. 6 Energy dispersion x-ray spectroscopy analyses of graphene inverse opals

Energy dispersive X-Ray spectroscopy (EDX) is an elemental analysis technique. Shown in figure 2.9 below demonstrates the presence of trace amount of nickel within graphene inverse opals scaffold. The atomic percentages as well as the molecular weight percentages shown that the nickel present exists in graphene inverse opals scaffolds as nickel oxide. Based on the oxygen weight and atomic percentages of

oxygen to that of silicon and nickel, we have metallic nickel presence in the GIOs.

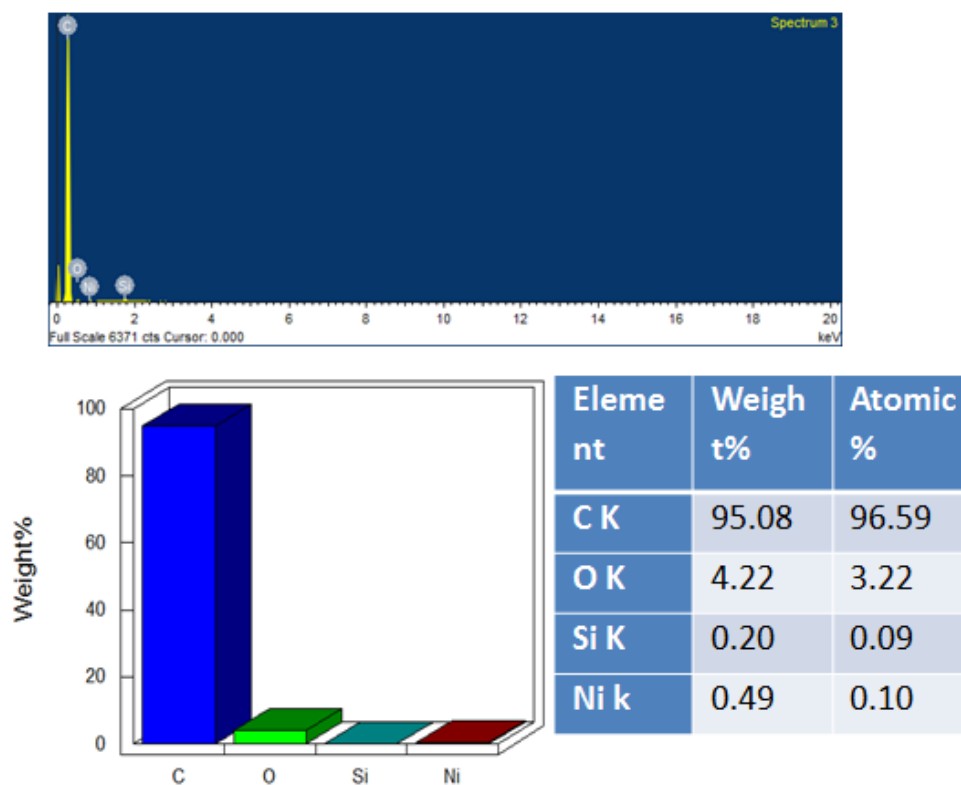


Figure 2.9. Energy dispersive x-ray spectroscopy of graphene inverse opals indicates the presence of trace amount of nickel oxide still present in the synthesized free standing pristine graphene inverse opals.

2. 4. 0 Discursion and conclusion

The high quality of the Raman spectrum of our synthesized GIOs compared to any 3D graphene material synthesized depicted that GIOs is the best 3D graphene material ever synthesized. The Raman spectrum of the synthesized GIOs shown a high intensity D-band compared to scotched tape multilayer graphene. This high defects intensity peak was expected because the edges of the etched graphene and the void caused by the dissolved PSS and nickel. In addition to these defects, are the grain boundaries defects

sources which can increase the defect concentration of the synthesized GIOs. The synthesized graphene inverse opals shown in figure 2.4 and 2.6 are mechanically stable and robust as shown by the constant transferred from one substrate to the next. This is very important because the objective will be to use these GIOs material for different applications. We used origin software to determine the average diameter of nickel inverse opal compared with the average diameter of graphene inverse opals (figure 2.10). Our calculations determine 4.6% shrinkage in the diameter of graphene inverse opal compare to nickel inverse opal. The shrinkage in size was attributed to the void created by the etched nickel resulting into surface stress on the free standing graphene inverse opals.

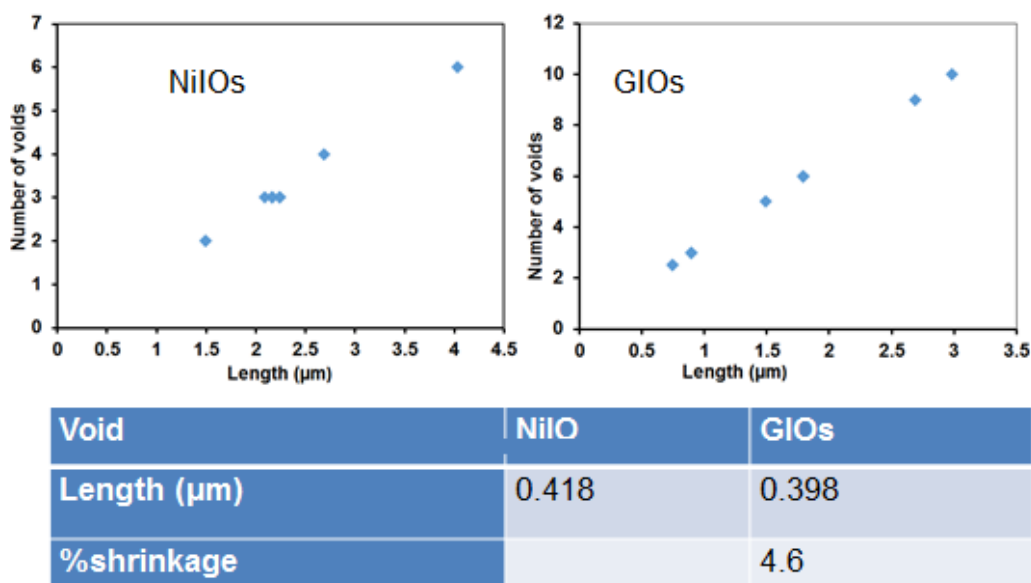


Figure 2.10. Graphs and table established the relationship between the size of nickel inverse opals (void) compared to that of graphene inverse apals. Graphs are the plot of illustrate the shrinkage percentage in GIOs as a function of quality.

Any three dimensional graphene nano-architecture materials could be synthesized using this method. To synthesize any three dimensional graphene scaffolds of interest, a metal frame work of the desire frame work must be first synthesized. The metal frame works save as sacrificial template for the graphene nano-architectural materials. Nickel has been shown to exhibit highest degree of carbon solubility^{28,50} resulting into multilayers graphene with high tensile strength to support 3D graphene scaffolds. Similar experiment was attempted on copper but with no observable findings because of the single layer graphene grown on copper.

2. 5. 0 Conclusions

We have shown in this project that highly porous free standing graphene inverse opal nanostructures can be synthesize by first designing a sacrificial metal template. The template must exhibit ability to facilitate the conversion of carbon into graphene. The SEM micrographs and Raman spectroscopic analyses confirmed that the synthesized GIOs nanostructures are free standing and mechanically stable architectures. With these findings, new opportunities to design highly porous graphene scaffolds using nanostructure architectural design can be foster. These will expand the applications of 2D graphene materials into 3D graphene materials as hypothesized^{75,92,93-94}

2. 6. 0 Future works

While we abled to scale the project to centimeter scales, we have not increase the thickness of the graphene scaffold. It will be beneficiary if we could develop a method that could improve the thickness to centimeters scale for the large areas synthesized graphene inverse opals. This improve material will be used for gas sensors^{15,95}. An increase in high specific surface area will make the material a formidable material for

sensors and energy storage devices better than 2D graphene. A Graphene inverse opal seems to exhibit high electrical conductivity as well as thermal stability compared with all the synthesized bulk graphene. Further studies will include measuring the conductivity of the material using four probe electrodes. The materials have been used as energy storage materials in supercapacitor and gas sensor devices making GIOs better candidate for these applications.

Chapter 3

Three-dimensional microspores architecture of carbon nanotube inverse opals scaffold

3. 0. 0 Introductions

Carbon nanotubes (CNTs) are cylindrical one dimensional material that exhibit high specific surface area, mechanical stability, charge mobility, conductivity and poor activity. These properties make CNTs the suitable material for electronics (acceptable electronic band gap), optical, energy storages, sensors and biomedical applications^{20, 58,96,97- 98}. The 1D CNTs are synthesized predominantly in 2D format with the direction of growth limited by the substrate as Nano-forest and Nano-carpet. Syntheses of 3D nanostructures require the catalyst to facilitate growth in 3D confirmation. 3D CNTs has been grown from 2D CNTs materials. Among the technologies used are: self-assembly of nanomaterials aided by lithographic patterning⁹⁹⁻¹⁰⁰, surface enhanced Raman scattering (SERS)^{26,101- 102} and printing¹⁰³ as well as micro-contact printing¹⁰³ aided by self-assembly and lithography. 3D CNTs scaffolds have been hypothesized as one of the best material to enhance the performance and applications of 2D and 1D carbon nanotubes devices¹⁰⁴. In addition, 3D nanostructures have been used to significantly increase the dosage of active materials in photocatalysis¹⁰⁵, electronics¹⁰⁶, chemical sensors and optoelectronics¹⁰⁷. Over the last decades, progressed has been made to engineer 3D CNTs materials using lithographic technology^{20,108-109}. These techniques incurred high cost, labor intensive and low productivity. Here, we present a novel bottom-up technology to synthesize 3D CNTs scaffolds. Our techniques utilized iron (II)

nitrate as catalytic source and polystyrene spheres templates as the pre-synthesized sacrificial template. We further present easy way to coin Iron (II) nitrate into 2D CNTs forest. This technology is fast, cheap, safe and economical. Field emission scanning electron microscopy, X-Ray diffraction, energy dispersive X-ray spectroscopy and Raman spectroscopy were used to study and characterize the synthesized 3D CNTs scaffolds.

3. 1. 0 Experimental

3. 1. 1 Reagent

Iron (II) nitrate, styrene, potassium per sulfate, ethanol, nickel foil, copper foil, acetylene, Argon, hydrogen, polydimethylsiloxane (PDMS), toluene, Iron (III) chloride, hydrochloric acids, polymethylmethacrylate (PMMA) and silicon dioxide wafer. All materials were purchased from Alfa Aesar and Sigma Aldrich and were used without any further purification.

The synthesized carbon nanotubes inverse opals (CNTs-IO) were performed in three steps. First, we synthesized polystyrene spheres (PSS) template as discussed in chapter 2. The synthesized PSS were then self-assembled on nickel and copper strips as discussed in chapter 2. Secondly, the self-assembled PSS substrates were infiltrated with solution of iron (II) nitrate. The iron (II) nitrate solution was prepared by dissolving 3g of iron (II) nitrate in 10mL solution (1:1 volume ratio of deionize water and 200 proof ethanol)¹¹⁰. The copper and nickel strips with self-assembled PSS were aligned vertically in an empty 100 mL beaker. The iron (II) nitrate solution was gently poured into the 100 mL beaker with about 1/5 inch of the nickel and copper substrates stripes soaked in iron (II) nitrate solution. The beaker with vertically aligned stripes and iron (II) nitrate solution was stored at room temperature for one hour. The infiltrated PSS templates were

removed from the beaker and dried in the oven for 30 minutes at 50°C¹¹¹⁻¹¹². The dried infiltrated PSS templates with iron (II) nitrate were oxidized on hot plot at 500°C in air. This process enable decomposition of PSS at the same time iron (II) nitrate oxidized into iron oxide (Fe_xO_y IO) inverse opals on copper and nickel strips. Chemical vapor deposition (CVD) system was used to synthesize iron inverse opals from iron oxide inverse opals¹¹³. This was achieved by reducing Fe_xO_y -IOs into Fe-IOs at 500°C under hydrogen gas (3sccm, 60mtorr) The iron inverse opals nanostructures were used as catalytic templates to synthesize three dimensional carbon nanotubes inverse opals (CNTs-IO). The advantage of this technique is the ability of the catalyst to facilitate grown of CNTs in all direction and not restricted by the substrate. Lastly the Iron catalytic templates were etched out together with the metal strips in concentrated hydrochloric acids for 30 minutes.

3. 1. 2 Synthesis of three dimensional carbon nanotubes inverse opals

An easy, cheap and fast method to synthesize 3D CNTs-IO scaffolds using Fe_xO_y -IO engineer from iron (II) nitrate. Iron oxide was obtained from the infiltrated iron (II) nitrate PSS templates. PSS were synthesized and self-assembled at room temperature⁷⁶ on copper and nickel foil as mention in chapter 2. The Iron oxides inverse opal (Fe_xO_y IOs) samples were then transferred into the CVD reactor for the synthesis of Iron inverse opal. Carbon nanotubes were grown on the pre-synthesized iron inverse opal at 500°C using acetylene as the carbon precursor and hydrogen as the carrier gas and etching agent as shown in figure 3.1b below.

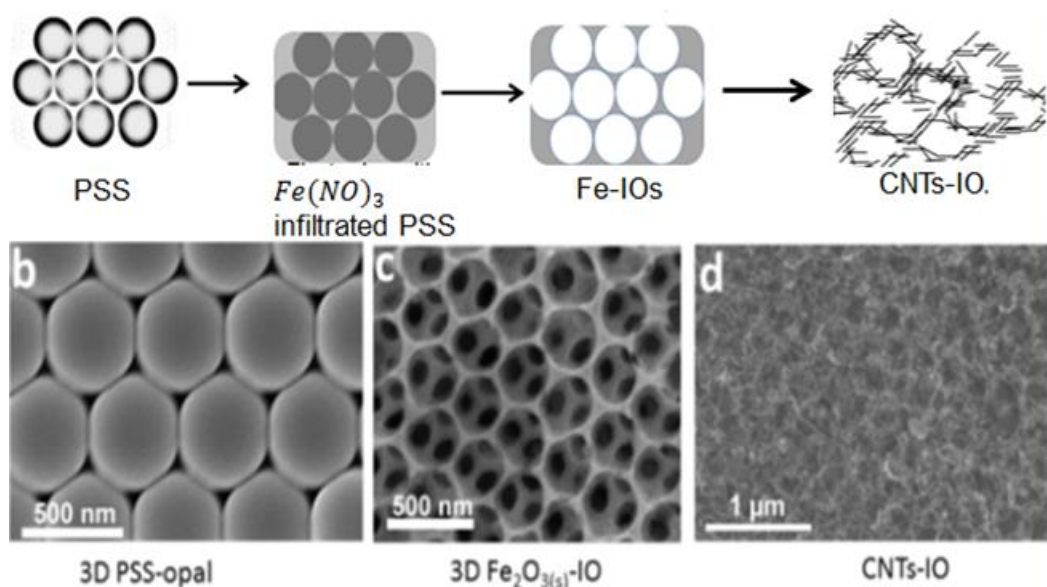


Figure 3.1. Schematic diagram and micrographs of carbon nanotubes synthesis from iron (II) nitrate. Field emission scanning electron micrographs of CNTs (a) Schematic diagram for the synthesis, (b) SEM micrographs for the self-assembled polystyrene spheres templates, (c) SEM micrographs for the oxidized Iron oxide inverse opals and (d) SEM micrographs for the synthesized carbon nanotubes inverse opals.

The synthesized Fe_xO_y IOs on the hot plates were removed and allowed to cool at room temperature. The samples were transferred into the CVD system and annealed under hydrogen (3sccm) up to 500°C for 30 minutes and hold at 500°C for another 30 minutes. Acetylene (carbon source) 0.5sccm was supplied into the system for different time 1, 2, 4, 6, 10, and 20 minutes. The effect of acetylene concentration on the growth of CNTs-IOs length was also studied by using different concentrations of acetylene (0.5, 1.0, 2.0 and 5.0sccm). The gravity of temperature was studied as well as different carbon precursor sources (methane and acetylene). The synthesized CNTs IOs scaffolds were cooled to room temperature. The samples were spin coated with PMMA to etch the copper substrate away and catalyst iron. The free standing CNTs IOs were

fished out with silicon dioxide wafer and the coated PMMA dissolved in acetone and the samples rinse in fresh acetone solution and were dried in the oven for 20 minutes before analyses.

3. 1. 3 Micro-contact printing of two dimensional iron oxide template

Lithography a printing technology was invented in 1796 by Aloise Senefelder a German actor. Soft lithography was used to synthesize a mesh with polymethylmethacrylate (PMMA) on silicon dioxide wafer. Polydimethylsiloxane stamps were fabricated using the PMMA mesh as the template. The PMMA mesh on silicon wafer was printed onto different PDMS solid transparent materials that serve as stamp. The silicon wafer was caged with copper and filled PDMS sol gel solution. The gel-like PDMS solution was cured at 50°C for one hour on hot plate. The PDMS stamp was then pill off from the PMMA mesh on silicon wafer. The PDMS stamps were used to transfer iron (II) nitrate jelly like solid-solution onto copper and nickel foil separately. The schematic shown below in figure 3.2 depicted how Iron oxide patches were fabricated by thermally oxidizing the stamped Iron (II) nitrate solid in air at 500°C on hot plate. The iron oxide patches were inserted into the CVD reactor for the growth of carbon nanotubes forest as shown below in figure 3.2 and figure 3.3b. The CVD precursor used was acetylene (2sccm), hydrogen gas (2sccm) etching agent. Iron oxide inverse opals were reduced into iron inverse opal at 500°C for 30minutes under hydrogen (3sccm) for 30 minutes.

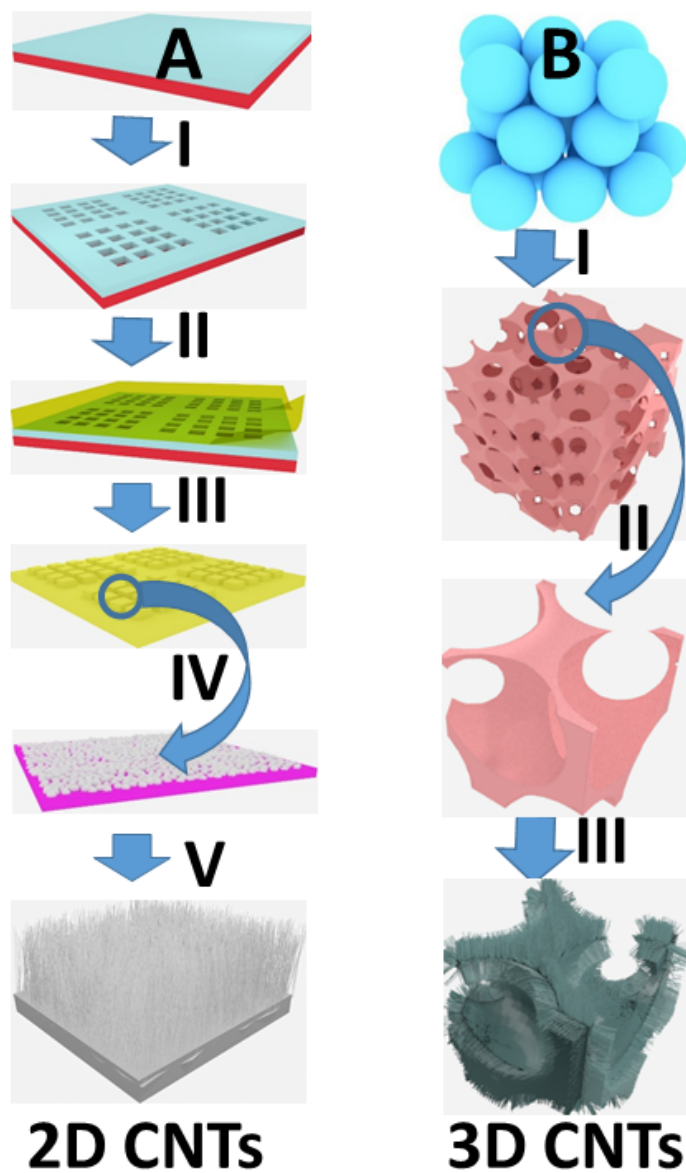


Figure 3.2. Schematic diagram for the synthesis of two dimensional carbon nanotube forest and three dimensional carbon nanotubes inverse opals using iron as the catalyst material. (A) synthetic pathw way for 2D CNTs forest and (B) synthetic path way for 3D CNTs-IO

3. 2. 0 Chemical vapor deposition of carbon nanotubes inverse opals

The synthesized carbon nanotubes inverse opals were controlled by annealing temperature, rate of annealing, concentration of carbon and the type of carbon source¹¹⁴⁻¹¹⁵. Temperature for the growth of CNTs-IOs were optimised. The substrate were also optimised. We observed that at elevated temperatures of 900°C, CNTs were grown on both the copper and nickel substrate containing iron FeIOs. When the temperature was increased to 1000C, only cluster of CNTs were synthesized on the nickel foil and almost nothing on the copper. Since nickel is used as the catalyst for CNTS synthesis, we rolled out nickel as the substrate and used only copper for the rest of the experiemnts^{56,116}. We studied the effect of rapid temperature increased on the synthesis of iron inverse opals. We observed that at high temperatures and higher temperate increase rates, sintering of iron ocured hindering the synthesis of carbon nanotubes but favoring the growth of carbon nanofibers as shown in figure 3.3 below. At higher temperature the iron nanoparticles nucleate together forming larger clusters of iron which catalyst the growth of carbon nanofibes as shown in figure 3.4 below. We used acetylene over methane because methane requires higher temperatures of 1000°C for activation over lower temperatures of activated acetylene¹¹⁷⁻¹¹⁸. The lowest activated temperature observed for acetylene was to 500°C. At 500°C no sintering of iron nanoparticles were observed during the growth of CNTs-IOs on iron inverse opals catalyst. Different flow rate of acetylene (0.5, 1, 2, 3, and 5) sccm were studied at constant time of 2 minutes at 500°C. Another experiment to study the effect of time and carbon precursor on the length of the synthesized acrbon nanotubes inverse opals scaffolds. The CVD system was held at 1, 2, 4, 5, 10, 15, and 20 minutes at constant acetylene concentration (2 sccm) and temperature (500°C). We observed that at high flow rate (concentration of acetylene), the synthesized CNTs-IOs changes from mixed carbon nanotubes to carbon nanofibers (figure 3.4). The length of the synthesized

CNTs-IOs were inconclusive because we have not identified the based method to separate and analysisist them.

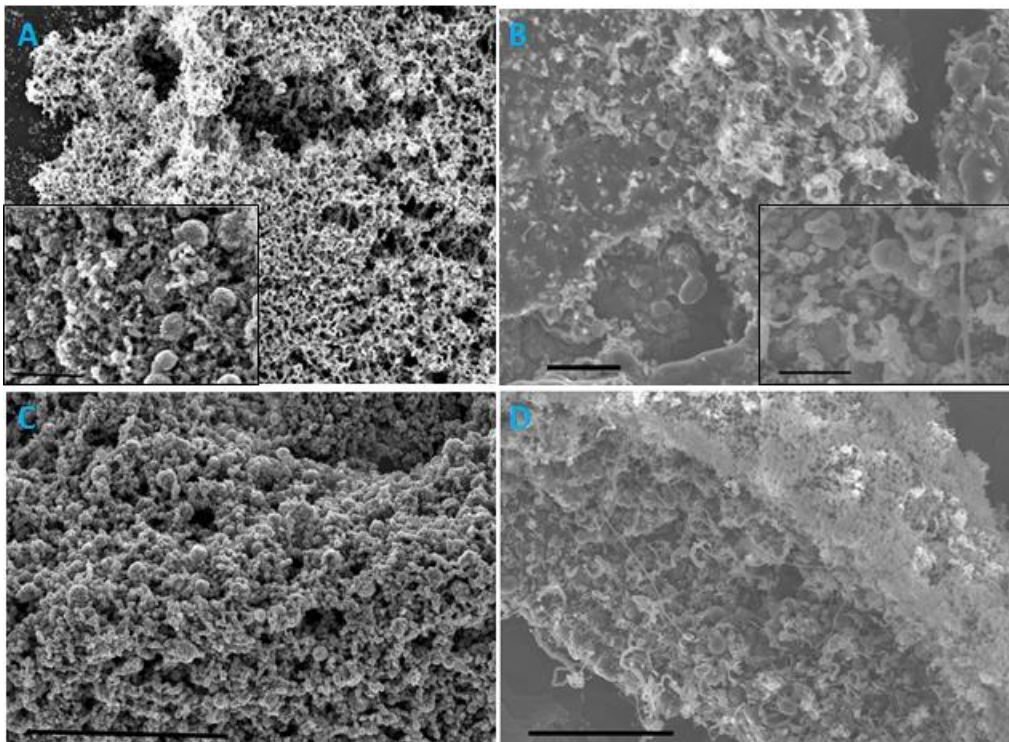


Figure 3.3. The field emission scanning electron (SEM) micrographs depicting the synthesized carbon nanotubes inverse opals at different temperatures and carbon source. (a & c) 600°C and 900°C with acetylene as the precursor and methane respectively and (b & d) 900°C and 700°C under acetylene and methane respectively.

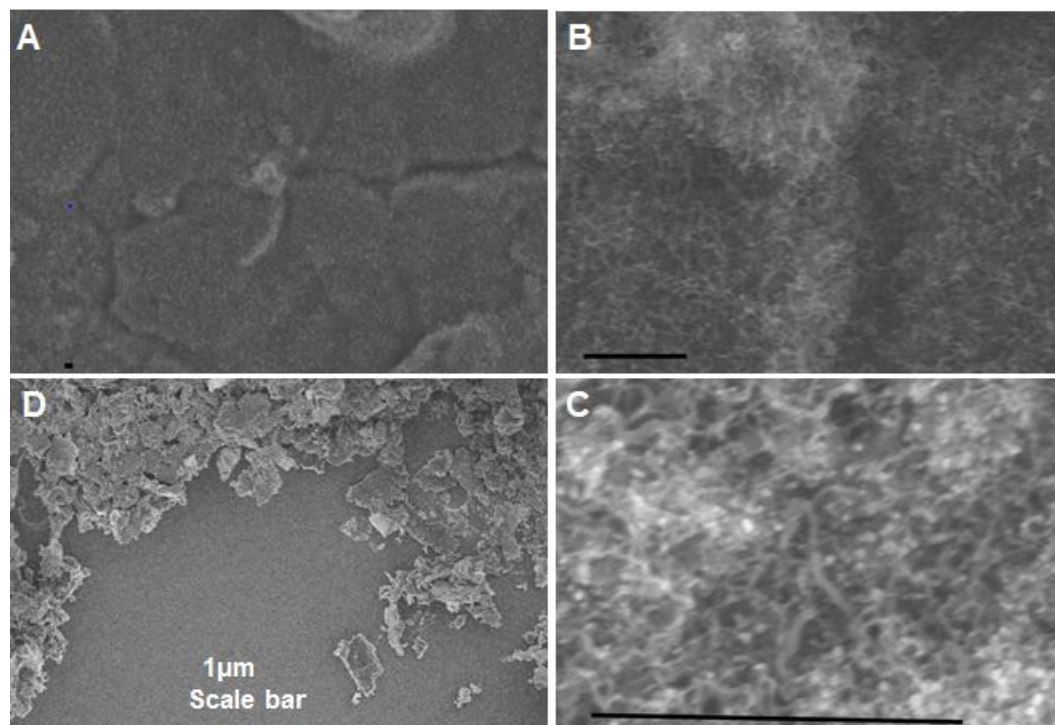


Figure 3.4. FE-SEM micrographs of carbon nanotubes forest synthesized from stamped iron (II) nitrate onto copper substrate. (a-c) SEM micrographs showing top view on the synthesized CNTs forest on copper foil before etching and (d) CNTs forest after the etched copper substrate at low magnification. The scale for the micrographs is 1 μm

The synthesized CNTs-IOs were spin coated with PMMA solution for 30 seconds, cured on the hot plot at 180°C for 90 seconds⁵⁰. The cured CNTs-IOs were transferred onto the concentrated hydrochloric acid to etch the copper substrates and iron catalyst. The suspended films of CNTs-IOs were fished out with glass substrates, rinsed with deionize water and the PMMA dissolved in acetone.

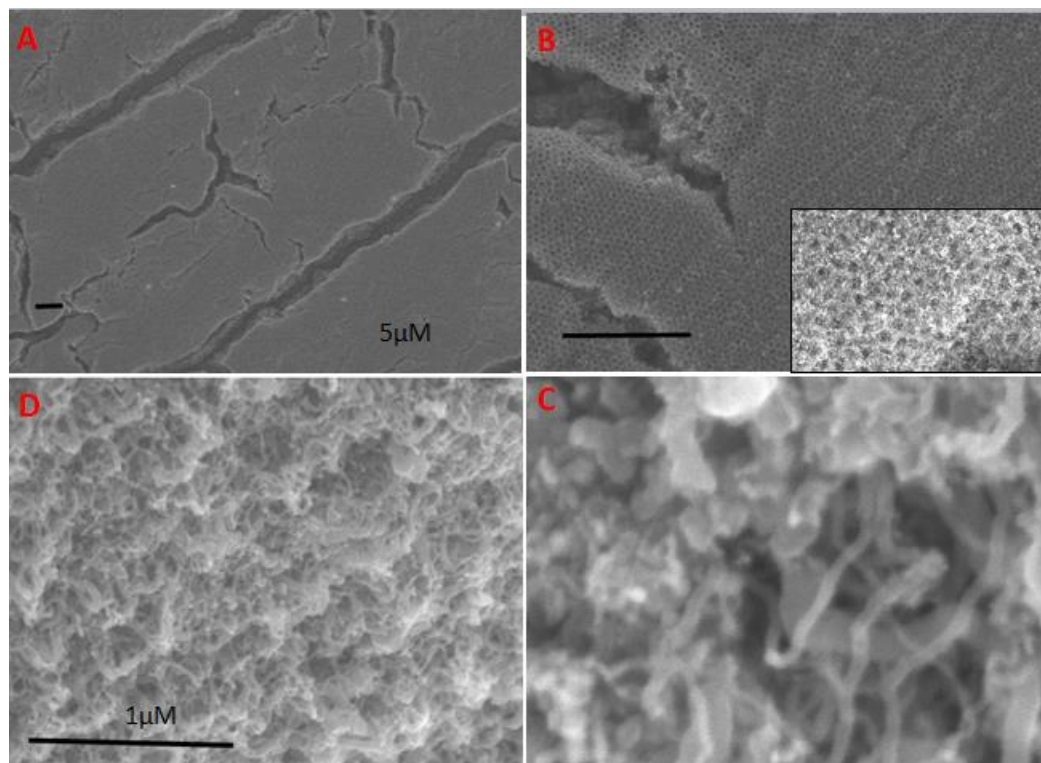


Figure 3.5. Field emission scanning electron (SEM) micrographs of the synthesized carbon nanotubes inverse opals as function of acetylene concentration. (a & b) acetylene (2sccm at 500°C) and (d & c) the flow rate of 4 and 5 while 10sccm has no changed from 5sccm.

Carbon nanotubes inverse opals were synthesized at 500°C (10°C per minutes) for 2 minutes with the flow rate of 0.5sccm acetylene under slow cooling rate. Research has shown that the growth of CNTs depends on the exposure of the catalyst to carbon precursor. In our work, we hypothesized that the synthesized CNTs-IOs stop growing as they reached their maximum length which is the radius of the iron inverse opals. At this stage, we believe that CNTs overwarm the catalyst such that no catalytic surface was exposed for CNTs growth^{118,119-120}.

3. 3. 0 Analysis and Results of carbon nanotubes inverse opals

Optical microscopy, Field emission scanning electron microscopy (figure 3.5 below), Raman spectroscopy, X-Ray crystallography and energy dispersive x-ray spectroscopy technologies were used to analyze and characterize the synthesized CNTs-IOs scaffolds and CNTs forest.

The synthesized CNTs-IOs were etched away in concentrated hydrochloric acid, fished out with silicon wafer and rinsed with deionize water three times. The clean CNTs-IOs were dried and inserted into acetone solution to remove the PMMA⁷⁷. The free standing CNTs-IOs were fished out on glass substrate dried in the oven for 10 munities at 50°C before analyses.

3.3. 1 Optical analysis of iron oxide template

Optical microscope was used to determine the micro-architecture of the pattern iron (II) nitrates template fabricated into iron oxide meshes. Figure 3.1 above 4.5(a &b) below depicted the fabricated iron oxide mesh templates. The brown color of the templates is dominantly due to the interference of copper substrate. The irregularities on the synthesized templates are from human errors. The optical and SEM micrographs shown below confirmed that the iron oxide mesh templates for CNTs forest were effectively synthesized.

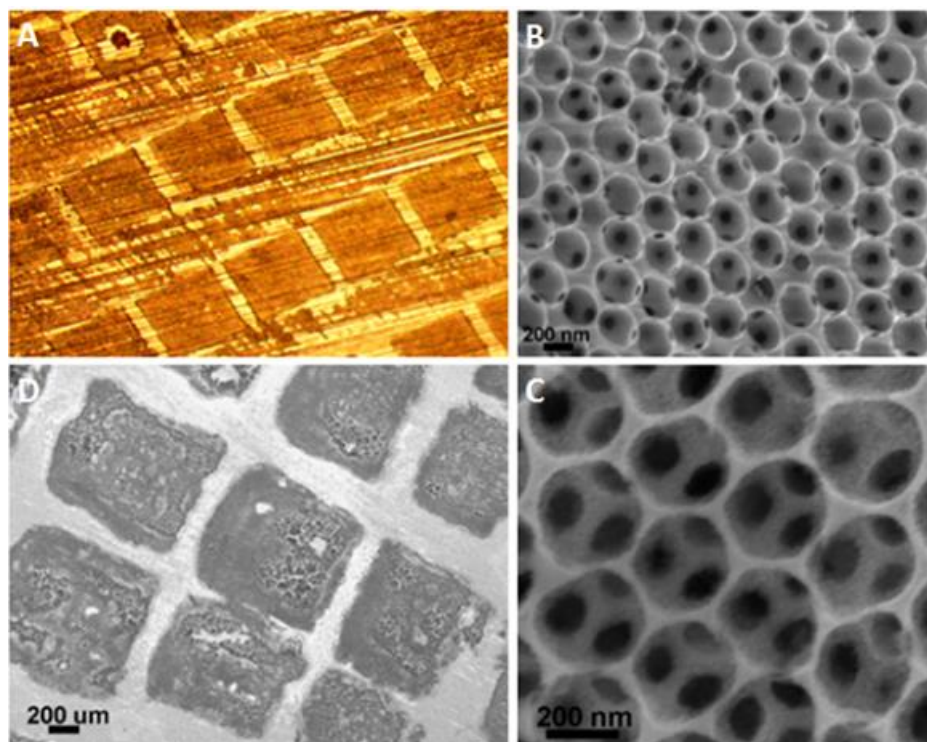


Figure 3.5. Field emission scanning electron and optical micrographs of iron oxide inverse opals scaffold. (a) Optical image of the stamped iron (II) nitrate on copper foil, (d) SEM micrograph of the stamped iron oxide and (b & c) SEM micrographs of top-view iron oxide inverse opals

3. 3. 2 Field emission scanning electron microscopy of carbon nanotubes inverse opals

The synthesized Carbon nanotubes were spin coated with polymethylmethacrylate. The samples were suspended on a solution of concentrated hydrochloric acid. The iron nanoparticles were etched out leaving the free standing carbon nanotubes inverse opal suspended on the hydrochloric acid solution. The thin scaffold film was fished out with silicon wafer and rinse several times with deionized water, dried at 50°C for hour before microscopic analysis. Figure 3.5 below shows the highly connected porous carbon nanotubes inverse opals architecture.

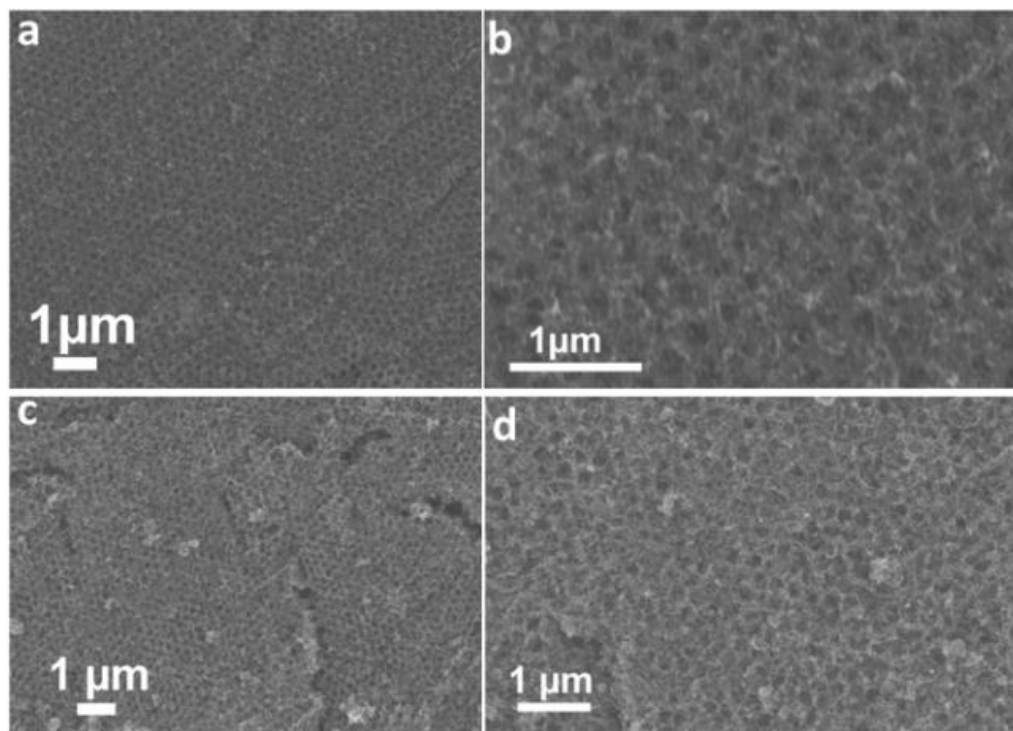


Figure 3. 6. SEM micrographs of carbon nanotubes inverse opals at different magnifications

3. 3. 4 Raman, XRD and EDX analysis of materials

The clean synthesized carbon nanotubes scaffolds were transferred onto a clean silicon dioxide wafer for Raman, XRD and EDX analyses. The Raman analysis confirmed that the synthesized materials are carbon nanotubes¹⁰⁹. The high intensity D-band (breathing mode for sp^2 hybridized carbon ring) merge with the dominant G-band peak (in-plane vibrations) and low intensity 2D-band ($\Gamma-\Gamma^*$ vibrations) all indicates CNTs. Below are the XRD spectra obtained for both iron oxide scaffolds, carbon nanotubes-iron inverse opals scaffolds and carbon nanotubes inverse opals scaffolds. XRD result supports that iron inverse opals were etched out giving free standing CNTs-IOs scaffolds. Figure 3.7 below includes EDX the elemental analysis of the cleaned CNTs-IOs scaffolds. The trace

amount of iron present in the synthesized clean CNTs-IOs scaffolds are attributed to the poor rinsing methods.

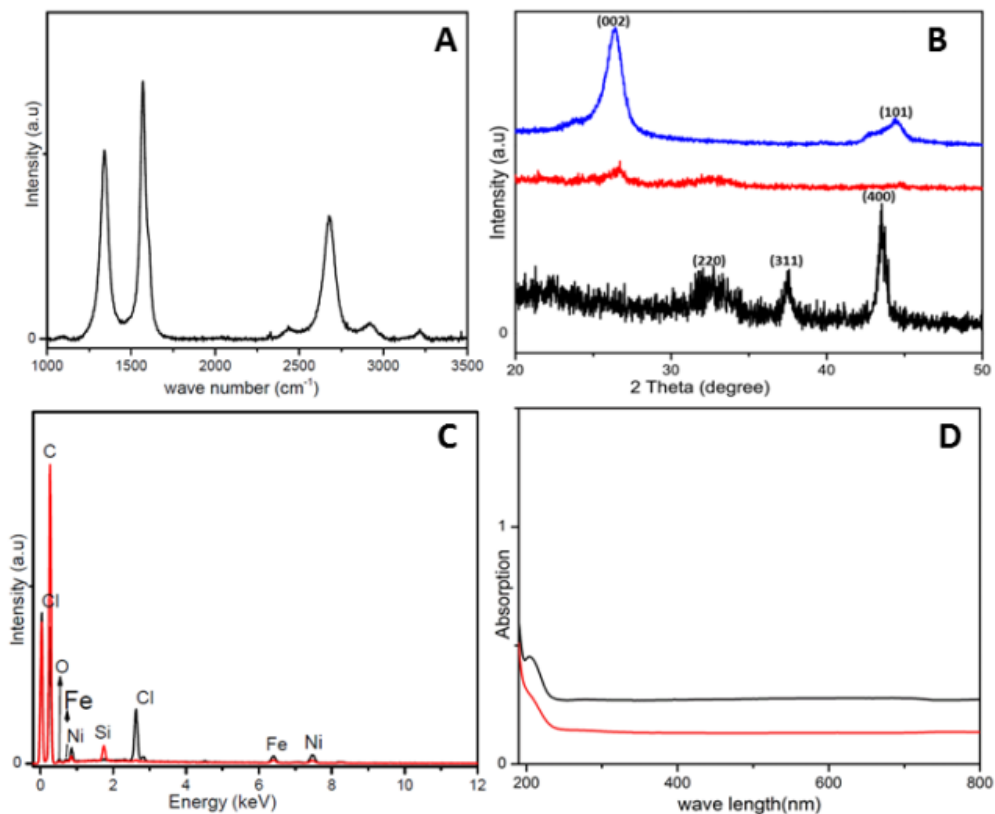


Figure 3.7. Raman, XRD, EDX and UV's Spectra analysis of carbon nanotubes inverse opals scaffolds. (a) Raman analysis of carbon nanotubes inverse opals scaffolds, (b) XRD spectrum of iron oxide inverse opals (black), carbon nanotubes-iron inverse opals (red) carbon nanotubes inverse opal (blue), (c) EDX spectrum show trace amount of iron, chlorine and nickel present in the clean dried carbon nanotubes inverse opals and (d) absorption spectrum of carbon nanotubes.

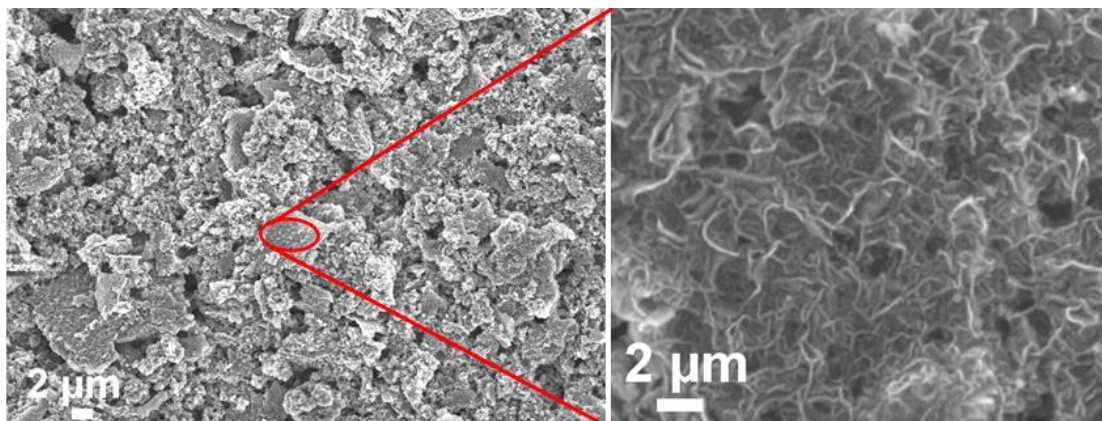


Figure 3.8. SEM micrographs of mechanically stable carbon nanotubes inverse opal scaffold after an hour of sonication. The synthesized 3D CNTs scaffolds exhibit high level of mechanical stability as well as connectivity compared with existing

3. 4. 0 Discursions

The synthesized 3D CNTs exhibit similar growth pattern as observed with 2D CNTs forest grown using cobalt¹²¹⁻¹²² or iron¹²³ nanoparticles as catalyst. This technology need to be scale up and optimizing the condition for the scaling up will be the next focus for this project. Complete removal of the trace amount of iron and nickel in the clean CNTs-IOs are paramount for the applications of CNTs-IOs in sensor devices. Large scale synthesis cracks free CNTs-IOs scaffold need attention for direct application of the product in energy storage devices like supercapacitors. This technology opens new avenues for the synthesis of 3D CNTs structures and other 3D nanostructures from ionic solutions. The SEM micrographs in figure 3.8 above are chunks of CNTs-IOs obtained after sonicating the metal free CNTs-IOs for over a day. The ability of these synthesized CNTs-IOs to remain as chunks attest to their mechanical stability and robustness. The synthesized 2D CNTs exhibit similar growth as 2D CNTs forest grown using cobalt¹²¹⁻¹²² or iron¹²³ nanoparticles as catalyst. This work established plausible avenues where 3D

CNTs-IOs including new architectures can be fabricated. Low cost, fast, easy and robustness make this technology more appealing and applicable for diverse materials.

3. 5. 0 Conclusions

We have demonstrated that 3D complex nanostructures of CNTs can be grown easily using metal salts frame work as the basic source of catalyst. We have established synthetic pathways that utilize metal salts as catalytic frame work to engineer 3D complex structures. The fact that the engineered scaffolds remained stacked together after an hour of sonication also attests to the high mechanical stability of these CNTs-IOs scaffolds. Research have shown that highly connected, porous materials with high specific surface area have increased the charging and discharging rate within bulk material in batteries^{58,108}. We believe that CNTs-IOs scaffolds may be a suitable material for supercapacitors and batteries. This project exposes new methods to fabricate complex 3D CNTs nanostructures.

3. 6. 0 Future works

The synthesized carbon nanotubes inverse opals and carbon nanotube forest (figure 3.5 and 3.6) will be used to fabricate gas sensor devices and energy storage devices such as supercapacitor and batteries. Improving this technology to obtain large scale synthesis will make these material applications achievable and applicable in a vast field such as biomaterial engineering.

Chapter 4

The-dimensional manganese (IV) oxide inverse opals architecture for oxygen reduction reaction (ORR)

4. 1. 0 Introductions

Manganese oxide (MnO_x) have been used for a number of different applications including electrocatalyst of oxygen reduction reaction (ORR) and often in metal-air batteries^{124,125,126-127}, an electrocatalyst for the detection of hydrogen peroxide, ascorbic acid, uric acid and others¹²⁸. Metal oxides such as MnO_x have been used as the cathode in MnO_2 -based dry cell batteries¹²⁹ and an active material for capacitors/pseudocapacitors^{130,131-132}. Manganese oxides are attractive materials for these applications because manganese is cheap, abundant, and environmentally friendly^{132,133-134}, when compared with other electrocatalytic materials like platinum. These applications requires material that exhibit high specific surface area (SSA) material and active. In order to increase the SSA of these materials, researchers have turned to nanoparticles^{133,135}, nanorods¹³³, nanotubes¹³³, nanosheets^{133,136}, nanowires¹³⁷, three-dimensionally ordered microporous (3DOM) structures^{110,138-139} and other structures with high SAA.

Manganese oxide materials can be synthesized through a variety of techniques, including hydrothermal^{131,132,133}, thermal decomposition of manganese salts^{124,140,141-142}, and electrodeposition¹³⁸. Designing different methods to synthesize metal oxides with high SAA and catalytic properties will be of great interest in regard to these applications. Here, we present a new unique, cheap and easy two-step technology to produce 3D MnO_2 -IO nanosheets material that exhibits high SAA and electrocatalytic activity for

ORR in alkaline environment. The two steps synthetic method involved thermal oxidation of aqueous manganese (II) nitrate to produce manganese oxide inverse opals scaffolds (Mn_2O_3 -IOs)⁴⁰. The second step was electrochemical oxidation of the synthesized Mn_2O_3 -IOs framework transforming the material into manganese dioxide nanosheets inverse opals scaffolds (MnO_2 -IOs) figure 4.1¹⁴³⁻¹⁴⁴. Brunauer–Emmett–Teller (BET) analysis as well as field emission scanning electron microscopy (FE-SEM) micrographs indicated that MnO_2 -IOs nanosheets material exhibit high porosity as well as an increased specific surface area (SSA). This increase in SSA is attributed to the transformed Mn_2O_3 -IO nanoparticles into MnO_2 -IO nanosheet scaffolds as well as the PSS suspenders as shown in figure 4.1 below¹⁴⁵.

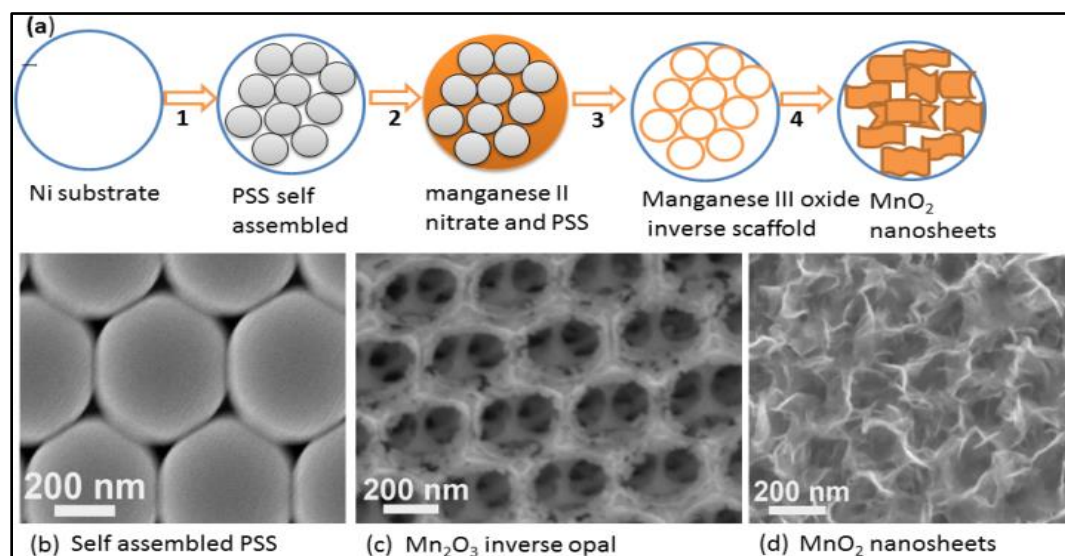


Figure 4.1. Schematic illustration of the two-steps synthetic pathway of MnO_2 -IO nanosheets scaffold: (a) schematic of the reaction steps: self-assembled PSS on nickel substrate (1), infiltration of PSS with 4.1M $\text{Mn}(\text{NO}_3)_2(\text{aq})$ (2), thermal oxidation (3) and electrochemical oxidation/transformation (4). (b) FE-SEM images of the material: self-assembled PSS, (c) Mn_2O_3 -IO scaffold and (d) MnO_2 -IO nanosheets structure

4. 2. 0 Experimental

Reagents; Sodium sulfate ($\geq 99.0\%$), potassium hydroxide (99.99%) and sulfuric acid (99.999%), potassium persulfate, styrene, ethanol, acetone and (30 wt. %) hydrogen peroxide were purchased from Sigma-Aldrich. Manganese (II) nitrate was purchased from Alfa Aesar. Toluene and ethanol (200 proof) were purchased from Decan Labs Inc, Nickel foil (0.010 inch thick) was purchased from McMaster Carr, and hydrogen gas was purchased from Linweld. All materials were used without further purification.

4. 2. 1 Synthesis of Manganese oxide (MnO_x) inverse opals

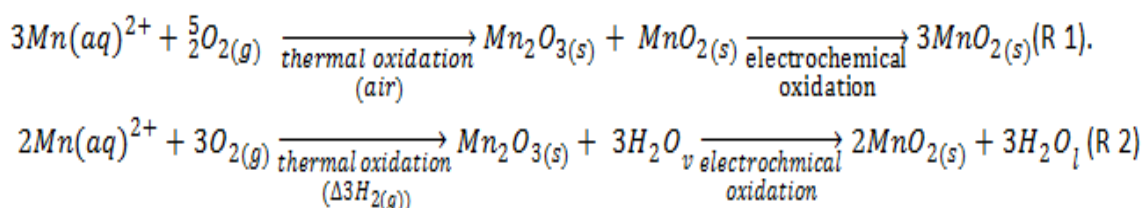
The synthesized PSS (300 nm) were dispersed in deionized water as explained in chapter 2 and 3 to obtain 3mg/mL solution. Stripes of nickel were aligned in a cleaned beaker held in place by scotch tape. 3mg/mL of the PSS was poured into the beaker with aligned nickel stripes. The beaker and its content was stored in the oven at 50°C overnight¹⁴⁶. The self-assembled PSS on nickel were transferred into a clean beaker. The tips of the nickel substrate with PSS were immersed in 4.1M manganese (II) nitrate solution. Manganese (II) nitrate solution was prepared in equivalent solution of 1:1 volume of ethanol and water. The PSS on nickel were infiltrated with manganese (II) nitrate solution over 1 hour at room temperature.

4.2.2 Thermal oxidation of MnO_x in air

The infiltrated PSS substrate was dried at 50°C for 30 minutes and were annealed at 500°C in CVD reactor^{141,146}. The CVD system was programmed by setting the ramp rate of 10°C/minute up to 500°C. The CVD system was held for 30 minutes at 500°C to

ensure complete decomposition of PSS. We used thermogravimetric analysis (TGA) to determine the decomposition temperature of PSS. Thermal oxidation of manganese oxide was performed both in air and hydrogen environments. Hydrogen was the reducing agent while argon was the carrier gas. Air and hydrogen conditions were used to optimize complete oxidation of manganese (III) oxide. Thermal oxidation under hydrogen was performed by decomposing PSS under hydrogen flow rate of 5.0 sccm at the pressure of 132 mtorr¹⁴⁷.

The reaction mechanism schemes of the manganese (III) oxide synthesis in air and in hydrogen condition are shown below.



The synthesized Mn₂O₃-IO nanosheet scaffolds were characterized with Raman spectroscopy, Field emission scanning electron microscopy (SEM). Figure 4.2 below are the SEM images of the synthesized MnO_x. The effects of PSS on MnO_x exfoliation were performed on bulk non-porous MnO_x samples. 4.1 M solution of manganese (II) nitrate were prepared in solvent (1:1 volume ratio of deionize water and ethanol). The solution was dropped casted on different nickel stripes and allowed to dry in the oven at 50°C for 30 minutes. The dried material was first annealed on the hot plate at 500°C for thermal oxidation. The samples were removed from the hot plate allowed to cool and were inserted in the CVD reactor. The samples were further oxidized in the reactor under hydrogen flow (3sccm) at 500°C for 30 minutes the same as the MnO_x scaffolds. The

samples were further oxidized in 1M sodium sulfate solution as the previous samples (figure 4.4).

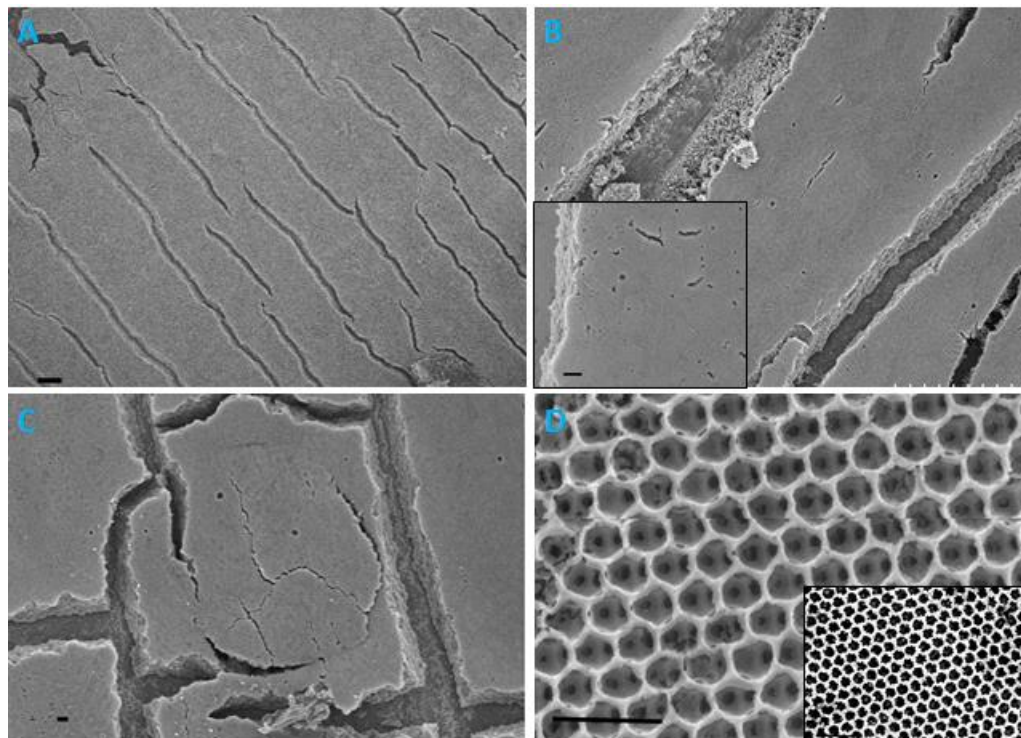


Figure 4.2. Field emission scanning electron micrographs depicting the synthesized MnO_x inverse opal on nickel stripes. (a & c) SEM micrographs top view of the MnO_x inverse opals and cracks domains (scale bar $20\mu\text{m}$ & $5\mu\text{m}$) and (b & d) SEM images showing the thickness, domains and inserted image at high magnification (scale bar $5\mu\text{m}$ & $1\mu\text{m}$).

4. 2. 2 Electrochemical oxidation of manganese (IV) oxide nanosheets

Electrochemical oxidation was performed on a CH Instruments model 1140B or 660C Potentiostat/Galvanostat in a three electrode cell configuration with a Pt basket counter electrode and Ag/AgCl (1 M KCl) reference electrode. All the potentials reported were compared to normal hydrogen electron (NHE)¹²⁴. 1M sodium sulfate electrolyte

was in the synthesis of Manganese dioxide inverse opals nanosheets. Thermal oxidized Mn_2O_3 -IO materials were treated using electrochemical technology. The nickel substrate that functions as the current collector was subjected to cyclic voltammetry (CV) at 0.253 and 1.253 V vs. NHE at $5\text{mV}\cdot\text{S}^{-1}$ or at constant potential between 0.353 and 1.253 V vs. normal hydrogen electrode (NHE) in a 3 electrode system for 1,000 to 10,000 seconds. The exfoliated MnO_2 inverse opal nanosheets were studied using Raman spectroscopy and field emission scanning electron microscopy.

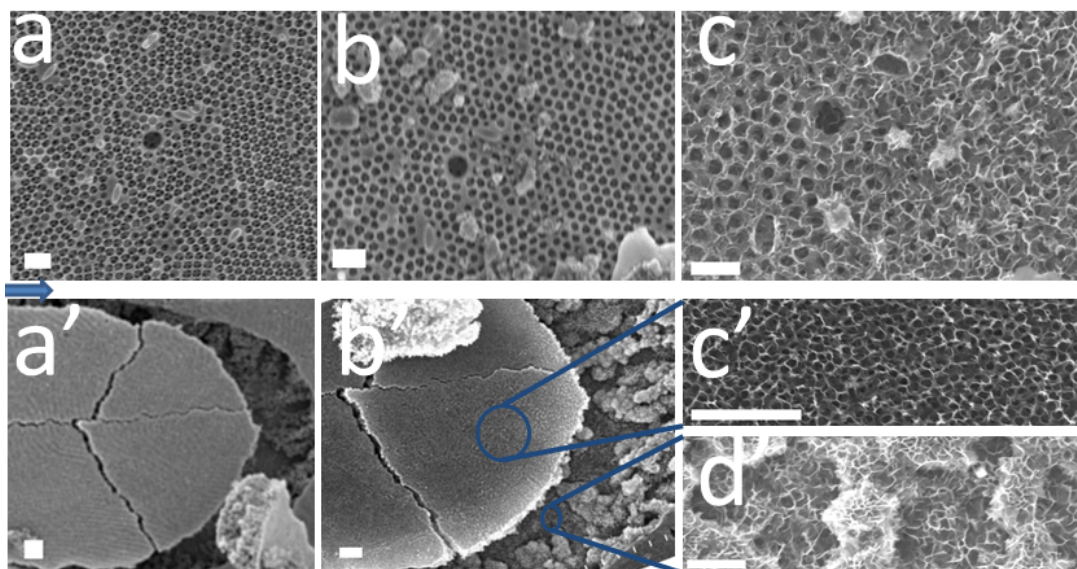


Figure 4.3. FE-SEM images depicting time-dependence study of electrochemical transformation of Mn_2O_3 -IO particles into MnO_2 -IO nanosheets scaffolds at constant potential (1.253 V vs. NHE). The scale-bars of the SEM images are $1\mu\text{m}$ for (a-c and a'-b') and 200 nm for (c'-d'). (a & a') SEM images of Mn_2O_3 -IO scaffold before electrochemical oxidation, (b, b', c' & d') SEM images studied of Mn_2O_3 -IO after 20,000 second of electrochemical oxidation and © SEM studied of Mn_2O_3 -IO after 50,000 second of electrochemical oxidation.

We studied the effect of time and the changed in potential on the pre-synthesized Mn_2O_3 -IO for at times and at different potentials. The obtained results provided clues

that adhesion of the Mn_2O_3 -IO to the nickel substrate is very imperative for electrochemical oxidation and transformation of Mn_2O_3 -IOs. After short time of electrochemical treatments of Mn_2O_3 -IOs, some sections of Mn_2O_3 -IO as shown in figure 4.3 above exhibited complete exfoliation while some took longer time and others did not oxidized after extended time treatments. Different set of samples were studied by repeatedly applying a constant potential over and over and the progress of electrochemical oxidation studied with SEM as shown in figure 4.3 above.

4. 2. 3 The role of PSS in oxidation of MnO_2 -IO inverse opals nanosheets

We designed an experiment to study the effect(s) of PSS on the electrochemical oxidation of Mn_2O_3 -IO nanoparticles into MnO_2 -IO nanosheets. Separate fresh bulk samples were prepared on nickel substrate PSS as explained above. The resulted bulk Mn_2O_3 substrates were electrochemically treated with the three electrode system as shown above. The results shown in figure 4.4 below indicated that bulk Mn_2O_3 nanoparticles can be directly oxidized into MnO_2 nanosheets by treating the samples electrochemically.

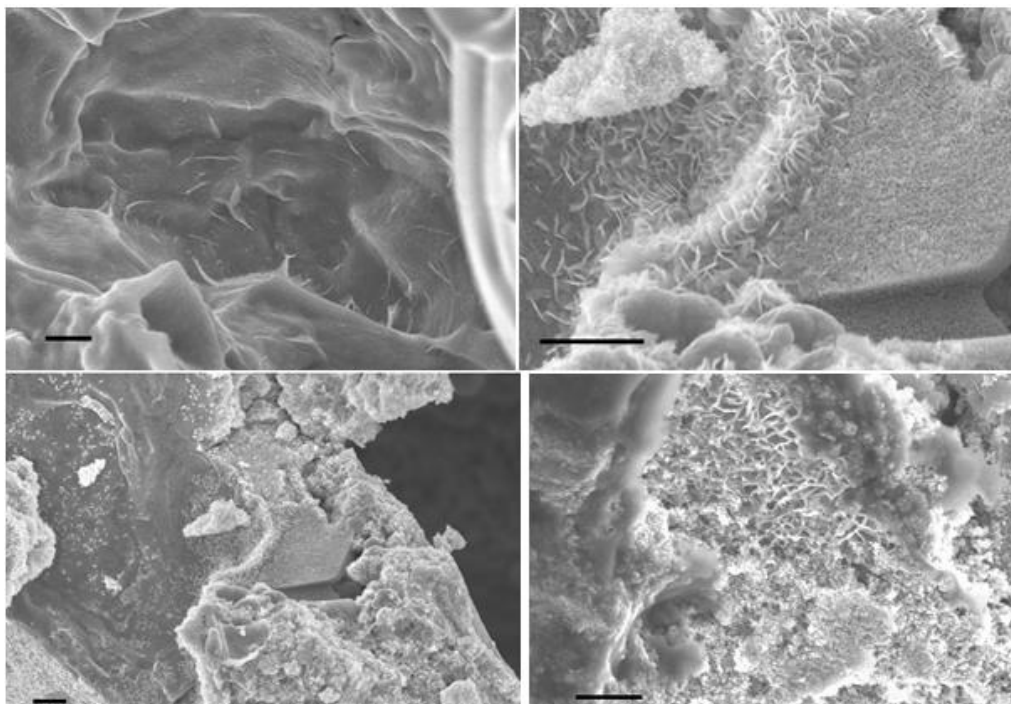


Figure 4.4. Scanning electron micrographs of bulk manganese dioxide nanosheets synthesized from bulk manganese (II) nitrate after thermal oxidation followed by electrochemical oxidation.

Based on our findings, PSS do not play any catalytic influence over the transformation of $\text{Mn}_2\text{O}_3\text{-IO}$ nanoparticles to $\text{MnO}_2\text{-IO}$ nanosheets but provide easy access for the sodium sulfate electrolyte. The adhesion of $\text{Mn}_2\text{O}_3\text{-IO}$ particle to the substrate and interaction with the electrolyte are the main factors that drive the transformation of nanosheets.

4. 2. 5 Manganese dioxide nanosheets catalyzed ORR

The electrolyte used for oxygen reduction reaction studies was the air-saturated or nitrogen-degassed 0.1M potassium hydroxide solution. The ORR studies were performed on the synthesized $\text{MnO}_2\text{-IO}$ nanosheets structures after thermal and electrochemical oxidation of $\text{Mn}_2\text{O}_3\text{-IO}$ with the three electrode system¹²⁸.

4. 3. 0 Analysis of manganese dioxide inverse opals nanosheets

The synthesized MnO_2 -IO nanosheets scaffolds were studied using FE-SEM as shown in figure 4.3 above. The SEM findings were further confirmed with Raman spectroscopy and X-ray diffraction analyses. Flame atomic absorption spectroscopy was used to study the oxidation of the Mn_2O_3 -IO after thermal oxidation under hydrogen conditions. The findings agree with the SEM, AAS and XRD findings. We confirmed the complete oxidation of Mn_2O_3 -IO to MnO_2 -IO nanosheets using X-ray photoelectron

| Sample | Amount of Electrochemical Oxidation (s) | O:Mn* |
|--------|---|---|
| 1 | 0 | 1.22 to 1.1 (Mn_3O_4) |

spectroscopy as shown below.

4. 3. 1 Flame atomic absorption spectroscopy (FAAS)

Perkin-Elmer Model 3100 AAS was used for the AAS to study the stoichiometry of the thermal oxidized manganese (III) oxide. The samples were massed and introduced to hot concentrated sulfuric acid solution. After cooling, hydrogen peroxide (30 wt. % in H_2O) was added until all MnOx had visibly dissolved. The solutions were quantitatively transferred to volumetric flasks and diluted to appropriate concentrations for FAAS. Mass percent of the individual atoms present were calculated.

| | | |
|---|---------|-------------------------------------|
| 2 | 10,000 | 2.1 to 1.67 (MnO ₂ + Mn) |
| 3 | 20,000 | 2.2 to 2.08 (MnO ₂) |
| 4 | 50,000 | 2.5 to 2.29 (MnO ₂) |
| 5 | 100,000 | 1.99 to 1.82 (MnO ₂) |

Table 4.1. Atomic ratio of the atoms present in the manganese oxide

Our result indicated that oxidized bulk manganese oxide in hydrogen condition (limited oxygen) were complete oxidized to manganese dioxide.

We employed X-ray photoelectron spectroscopy (XPS) PHI Versa Probe II instrument equipped with monochromatic Al K(alpha) anode source an X-ray source ($h\nu = 1486.6$ eV), and hemispherical analyzer to study oxidation state and composition of the synthesized MnO_x. The X-ray source power was 65 W at 15 kV, 260 micron beam and take off angles of 45 degrees. The ultimate Versa Probe II instrumental resolution was determined to be 0.35 eV using the Fermi edge of the valence band for metallic silver. The resolution with charge compensation system was 0.68 eV FWHM on PET. The instrument work function was calibrated (BE) of 84.0 eV for Au 4f_{7/2} line on metallic gold and the spectrometer dispersion was adjusted to give a BE's of 284.8 eV, 932.7 eV and 368.3 eV for the C 1s line of adventitious (aliphatic) carbon from the non-sputtered samples. The PHI double charge compensation system was used on all samples, to remove any photovoltaic charging effects from the data. The spectra were additionally

checked for charging and other artifacts by measuring the Fermi level with temperature, and using that as a second reference standard and provide a more accurate assessment of binding energies for our nonconductive molecular materials. The instrument base pressure was ca. 8×10^{-10} torr. All XPS spectra were recorded using PHI software *SmartSoft –XPS* v2.0 and processed using PHI *MultiPack* v9.0 and/or CasaXPS v.2.3.14. Signal above background measurement and Shirley background subtraction was made using *CASA XPS* software. Peaks were fitted using GL line shapes, an accepted combination of Gaussian and Lorentzian. Up to 50 scans were accumulated. A given sample was examined at 5-6 different spots on the mounted specimen to assure that consistent, reproducible results were obtained. XPS has been used to analyze MnO_2 nanostructures^{132,148,149-150} and in this case was used to gain information about the surface oxidation state of the manganese oxide inverse opal scaffold. XPS was run on a set of samples that ranged from as-synthesized Mn_2O_3 -IO with no electrochemical treatment to a sample with 100,000 seconds of constant potential electrochemical oxidation. The X-ray photoemission spectra for these samples are shown in the supplementary information and the O:Mn ratio that has been calculated from those data is shown in Table 1. The data indicates that the surface of the manganese oxide scaffold is converted primarily to Mn^{4+} within 20,000 seconds of constant potential electrochemical oxidation. This was interesting as FE-SEM images didn't show much change until 50,000 seconds or more of electrochemical oxidation. This was attributed to samples to samples preparation variation. The quality of contact between the manganese (II) oxide scaffolds and the nickel substrate has been shown to of great importance in the electrochemical oxidation of manganese oxides.

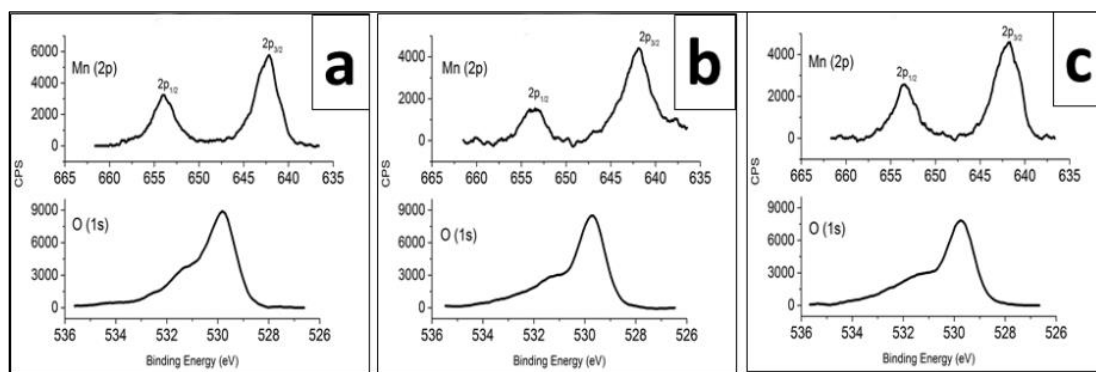


Figure 4.5. XPS analyses of the step synthesis of MnO_2 -IO nanosheets using thermal and electrochemical oxidation. (a) As synthesized Mn_2O_3 -IO using thermal oxidation, (b) electrochemical oxidation of (a) after 20,000 seconds and (c) Electrochemical treatment of (a) after 50,000 seconds

The XPS analysis of the synthesized Mn_2O_3 -IO nanosheets confirmed that the materials were electrochemically oxidized and transformed into MnO_2 -IO nanosheets scaffolds. XPS analysis performed on the thermally oxidized Mn_2O_3 -IO in air (figure 4.5a), XPS analysis on the electrochemical oxidized MnO_2 -IO nanosheets for 20,000 seconds (figure 4.5b) and XPS analysis on the electrochemical oxidized MnO_2 -IO nanosheets 50,000 seconds (figure 4.5c). XPS results confirmed that manganese (II) nitrate can be thermally and electrochemically transformed into MnO_2 nanosheets.

Field emission scanning electron microscopy (Hitachi S4700 FE-SEM) was used to analyze the morphology of the material as synthesized on nickel substrate. The synthesized materials were analyzed before electrochemical treatment and after electrochemical treatment. Figure 4.6 below are micrographs of the manganese (III) oxide inverse opal and manganese dioxide inverse opal nanosheets.

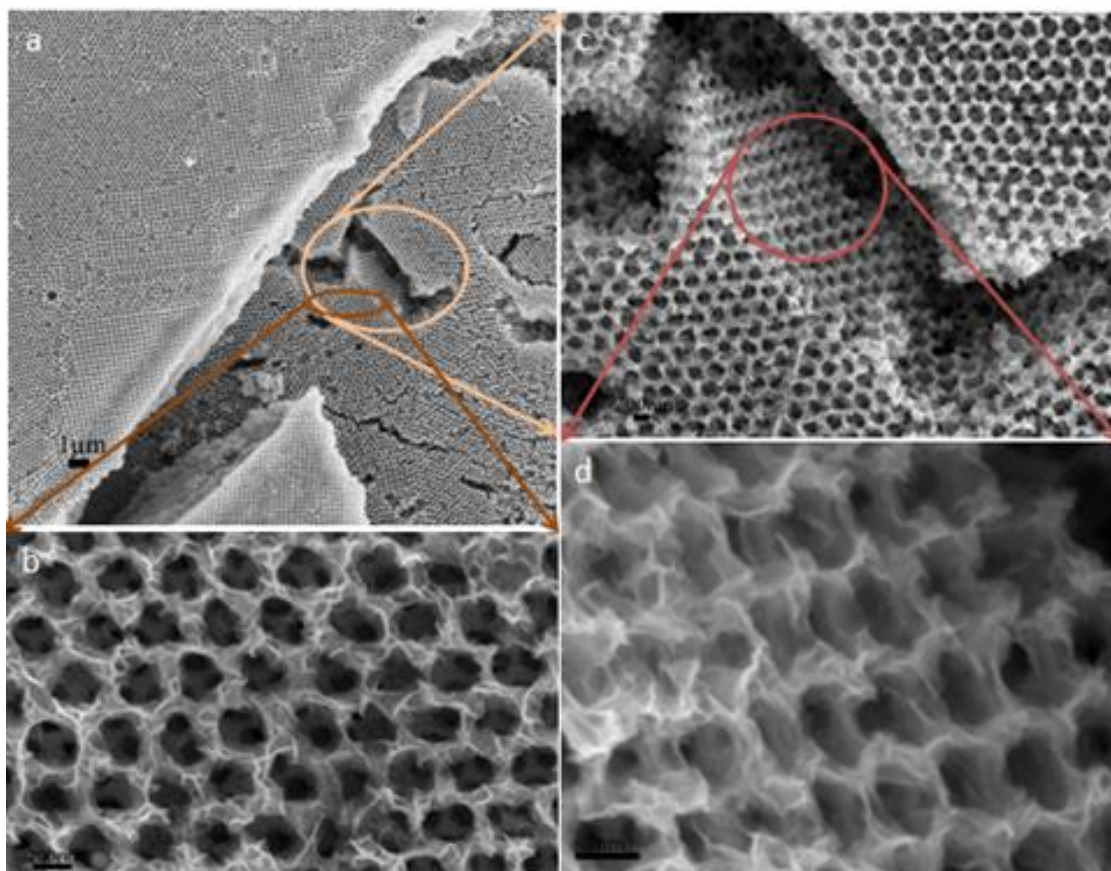


Figure 4.6. Scanning electron micrographs depicting the complete transformed MnO_2 -IO nanosheets scaffolds. (a) SEM image of top-view of MnO_2 -IO nanosheets scaffold, (b) SEM cross section image showing the in-depth synthesis of MnO_2 -IO nanosheets structure, (c) SEM magnified cross section image of MnO_2 -IO nanosheets and (d) SEM high magnification image top view MnO_2 -IO nanosheets on the top surface

Electrochemical oxidation of Mn_2O_3 -IO was study using SEM figure 4.3 & 4.6 above. The samples were imaged before and after the electrochemical oxidation for 20,000 seconds figure 3(b and b'), after 50, 000 seconds figure 3c and figure 3 (a and a') before

electrochemical oxidation. Different samples of Mn_2O_3 -IO that were treated for shorted time shown proportional degree of exfoliation as we extended the time of treatment.

X-ray Diffraction (PANalytical-Empyrean diffractometer was used to analyzed the MnO_2 -IO nanosheet scaffolds , X-ray diffraction (XRD) at power (40Kv/44mA), Recslit 0.3 mm, step 0.04 and scan rate of 1.5 degree/minute was used to analyze the crystal structure of the synthesized manganese dioxide inverse opal nanosheets⁴⁰. The absorption spectroscopy (Jasco V-670 spectrometer) was used to determine the absorption wavelength of the synthesized manganese dioxide inverse opal nanosheets. Raman spectroscopy (DXR microscope 532 nm filter was used to analyze the synthesized manganese dioxide nanosheets. The materials were analyzed with Raman spectroscopy while there were still on the nickel substrate. Raman spectra (figure 4.5a) were measured before electrochemical treatment of Mn_2O_3 -IO material and after electrochemical treatments. Raman analyses were performed on different set of material after 20,000 seconds and after 50,000 seconds of electrochemical oxidation at constant potential. Figure 4.3 depicts the exfoliation progress of manganese (III) oxide to manganese dioxide nanosheets as a function of time studied with FE-SEM. Raman spectroscopy analysis illustrates the transformation progress of Mn_2O_3 -IOs material into MnO_2 inverse opal nanosheets. This were evidenced by the peaks at 492.5 nm and 575.4 nm in plane bond vibrations of Mn^{4+} -O bonds in MnO_2 nanosheets as well as Mn_2O_3 -IO inverse opal material. The peak at 640.9nm are caused by the Mn^{3+} -O bond vibration^{124,141,151}. The shift in peak positions towards the larger wave number for the 20,000 seconds and 50,000 seconds Mn_2O_3 -IO treatment when compared to the Mn_2O_3 -IO Raman analysis are attributed to the changed in particle size. Nanosheets have large surface area compared to nanoparticles creating the shift in peak position figure 4.3. XRD analysis indicated the presence of MnO_2 -IO nanosheets as well as Mn_2O_3 -IO

particles as shown in Figure 4.3b. The XRD peaks labelled in black are attributed to MnO_2 while the peaks in green are attributed to Mn_2O_3 . The nickel peaks observed, shown in red, are contributions from the nickel substrate^{124, 141-142}. Energy dispersive spectroscopy (EDS) analysis of the material (supplementary information) also detected nickel from the substrate and additionally detected some carbon trace impurities, likely from PSS. Given that peaks attributable to Mn_2O_3 were present in addition to peaks attributable to MnO_2 indicates that the material had not been fully converted into MnO_2 . The XRD peaks analysis agrees with literature studies. FE-SEM images above depict the thickness of the MnO_2 -IO nanosheets scaffold. This means that large thick MnO_2 -IO nanosheets scaffold can be synthesized using this two-step technique. Degree of MnO_2 -IO nanosheets transformation is also attributed to the contact between nickel substrate and the material (fig. 2.4 SI).

After Raman, XRD, UV-Vis and XPS analysis of the Mn_2O_3 -IO and MnO_2 -IO nanosheets, it was hypothesized that perhaps a more complete or more substantial formation of nanosheets could be achieved if the manganese oxide inverse opal material was in a lower oxidation state prior to electrochemical transformation. Given that the nanosheets formation were clearly caused by the constant potential electrochemical oxidation, it would be a reasonable expectation that if the MnOx -IO was synthesized in such a way that it would be all Mn(III) or a mixture of Mn(III) and Mn(II), it might yield a more abundant amount of nanosheets

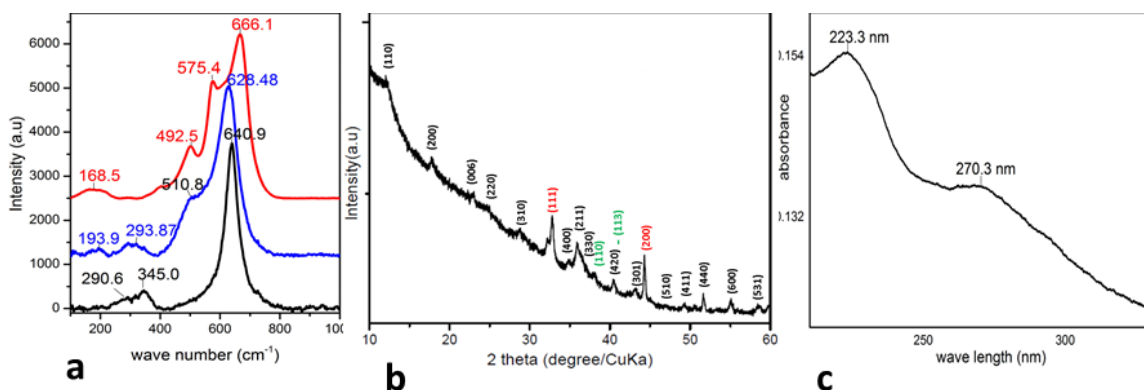


Figure 4.3. Raman, XRD and UV-Vis analysis of MnO_2 -IO nanosheets material indicates complete transformation of the material. (a) Raman spectra of MnO_2 -IO nanosheets transformation as a function of time (black thermally oxidized Mn_2O_3 -IO, blue after 20,000 seconds electrochemical treatment and red after 50,000 seconds electrochemical treatment. (b) XRD of MnO_2 nanosheets (black), Mn_2O_3 (green) and nickel substrate (red) and (c) UV-Vis spectrum indicates MnO_2 -IO nanosheets material with a shift in wavelength due to mix trace of Mn_2O_3 -IO material.

Following the optimization procedure of MnO_2 -IO nanosheet, the potential applications for this highly porous (figure 4.4) electrocatalytic material was explored. It was observed that after 100,000 seconds at constant potential of electrochemical oxidation, the material was not fully oxidized to manganese (IV) oxide with the air oxidized samples, as evidenced by SEM study with some sections of the sample with no nanosheets (supplementary information). Due to this partial oxidation, electrocatalyzed oxidations were not feasible since there was a large oxidation current background attributable to the manganese (III) oxide scaffold undergoing electrochemical oxidation. Electrocatalyzed reductions were then explored; one of the most common of which for

MnO₂ is the electrocatalytic oxygen reduction reaction. ORR was investigated using CV in 0.1 M KOH that was air or nitrogen saturated and these scans are shown below.

4. 4. 0 Oxygen sensors

For the air annealed sample with 50,000 seconds of electrochemical nanosheet formation, there is an irreversible reduction wave starting around ~0 V that can be attributable to ORR as it is no longer present when the solution has been degassed with nitrogen. For the hydrogen annealed sample, more scans were performed, including before nanosheet formation. Prior to MnO₂-IO nanosheet formation (red and blue lines), a redox couple appears to be centered about 80 mV. It is likely that this redox couple is Mn³⁺/Mn²⁺. In air saturated 0.1 M KOH, a peak is beginning to form at ~-0.6 V, which is likely attributable to ORR. When nitrogen degassed, this peak is no longer present. After nanosheets formation, 50,000 seconds of constant potential application (green and purple lines), a very different cyclic voltammogram was recorded. In an air saturated solution, an irreversible reduction wave is observed, starting around -0.1 V. When degassed with nitrogen, there is still a peak in the same position, but with significantly decreased in magnitude indicating that the peak was due to oxygen reduction. A control experiment with only a nickel current collector was performed to ensure that the nickel was not contributing to the ORR.

While the CV scans shown here are primarily qualitative in nature since probing the electrocatalyst's performance via rotating disk electrode is not feasible, there can still be conclusions drawn from these data. The air annealed sample has its ORR peak approximately 100 mV more positive than that of the hydrogen annealed sample. This is

possibly due to contact resistance issues and electrode to electrode variability, as described previously. The hydrogen reduced sample appears to have much less capacitance after nanosheet formation, while the air annealed sample has a fairly significant amount of capacitance that the ORR peak is superimposed upon. This suggests that the hydrogen annealed sample undergoes a more complete transformation to MnO_2 , as other MnO_x species do not contribute to the electrocatalytic ORR and it is known that the air annealed samples do not undergo a complete transformation to MnO_2 .

4. 5. 0 Discussions

UV-Vis spectrum shown above in figure 3C with absorption at 223.3 nm and 270.3 nm which agrees with prior research also supports that this material is MnO_2 -IO nanosheets^{1,140,142}. This analysis was performed by sonicating the samples in deionized water for 30 minutes. The nickel substrate was then fished out using spatula. The UV-Vis matches with literature review but with the shift of the peak position up higher wave length. This shift is attributed to the size of the as synthesized MnO_2 -IO nanosheets. Following the optimization procedure of MnO_2 -IO nanosheet, the potential applications for this highly porous (figure 4) electrocatalytic material was explored. It was observed that after 100,000 seconds at constant potential of electrochemical oxidation, the material was not fully oxidized to manganese (IV) oxide with the air oxidized samples, as evidenced by SEM study with some sections of the sample with no nanosheets (supplementary information). Due to this partial oxidation, electrocatalyzed oxidations were not feasible since there was a large oxidation current background attributable to the manganese (III) oxide scaffold undergoing electrochemical oxidation. Electrocatalyzed reductions were then explored; one of the most common of which for

MnO₂ is the electrocatalytic oxygen reduction reaction. ORR was investigated using CV in 0.1 M KOH that was air or nitrogen saturated and these scans are shown below.

4. 6. 0 Conclusions

MnO₂-IO nanosheet structures were synthesized using a unique two steps technique of thermal oxidation followed by electrochemical oxidation. X-ray spectroscopy, Raman spectroscopy, Absorption spectroscopy, and others were used to characterize and analyze the formation of MnO₂-IO nanosheet scaffolds. It was found that optimization of the nanosheet formation could be achieved by reducing the manganese oxide scaffold during the thermal step of the synthesis. This method has shown great potential for large scale synthesis of three dimensional MnO₂-IO nanosheets. The MnO₂-IO nanosheets showed activity for ORR, and due to the high porosity and surface area of the scaffold-based material, it may be applicable to gas diffusion type electrodes used in metal-air batteries¹²⁸. Experimental results indicated that the oxidation of Mn (II) nitrate into Mn₂O₃ is more effective under hydrogen condition. This is true because hydrogen is used to partially reduce MnO₂ to Mn₂O₃. Hydrogen function as a reducing agent to prohibit the synthesis of MnO₂-IO material also pumping the chamber down reduces the oxygen concentration which favor the synthesis of Mn₂O₃ over MnO₂. SEM images indicated that the degree of synthesis of MnO₂-IO nanosheets was greatest with Mn₂O₃ synthesized under hydrogen over those in air and vacuum and ORR response was well differentiated with samples synthesized in hydrogen environment.

4. 7. 0 Future works

The synthesized MnO₂-IO scaffolds need synthetic design for large scale production. This will enable the application of this material in supercapacitors¹⁵², batteries¹⁴⁸ and sensors¹⁵³. Some metal oxides like vanadium pentoxide need evaluation using this technology.

Chapter 5

Flexible transparent electrochromic device of electrochemical deposited tungsten

(VI) Oxide on bilayer graphene electrodes

5. 1. 0 Introductions

Electrochromism is the phenomenon where some materials reversibly change their color as a result of redox reaction of the material. Electrochromism is dated back to 1704 when Diesbach discovered that Prussian blue changed from colorless to blue in the presence of iron oxidation¹⁵⁴⁻¹⁵⁵. This phenomenon is used to fabricate devices that change color as a function of potential changes in screens and windows. Tungsten trioxide among other transition metal oxides like titanium dioxide and nickel oxide has been well studied as electrochromic (EC) materials. Tungsten trioxide (WO_3) was discovered in 1930 by Kobosew and Nekrassow as an electrochromic material and was later explained the changes in oxidation state of Tungsten oxide in 1953 by Kraus¹⁵⁶⁻¹⁵⁷. Tungsten trioxide is one of the transition metal oxides that has been extensively studied as the best electrochromic material for smart windows, solar cells and windows¹⁵⁸. Integration of electrochromic materials on flexible-transparent plastic have led to high level of anti-counterfeit development¹⁵⁹. Flexible electrochromic devices (ECD) are those that can easily exhibit electrochromism when a spurt of charge is applied¹⁶⁰. This technology to control the amount and frequency of charges supply to the device has led to high efficient ECD and more applications for electrochromism. Optical properties of ECD (transmission, absorption, reflectance, and emittance) are controlled by an uninterrupted charges supply or interrupted charges supply. Manipulating the frequency and efficiency

of electrochromism by playing with the potential source has led vast applications of ECD in mirrors, smart-windows, and EC display like computer screens and television screens.

The core of ECD is their flexibility, transparency and their applications on plastic substrate. High Conducting-transparent electrodes are paramount to the fabrication of good-efficient and applicable ECDs. Graphene substrate has been used as the conducting electrode for WO_3 ECDs. The graphene sheet for electrode was transferred onto glass substrate after chemical vapor deposition of graphene for ECD^{61,161}. The fabricated ECD was not robust and flexible because of the poor flexibility of glass substrate. The active material tungsten trioxide was chemically deposited on the transferred graphene on glass substrate. The oxidation state of tungsten oxide changes between 6 and 4 providing resistance in the efficiency in the rate of color changes¹⁶². Here, we present easy, fast, new and efficient technology to design ECDs with graphene and WO_3 on flexible plastic substrate. The fabricated ECDs will be synthesized via electrochemical deposition of WO_3 from tungsten resulting into a single state tungsten material (W^{+6}) with low resistance to electrochromism.

5. 1. 0 Experimental

Transparent thin film of WO_3 for electrochromic devices are synthesized either via thermal deposition^{163,164-165} or electrochemical deposition^{166,167,168,169}. Tungsten is a high thermal stable material with melting point of 3,422°C but the metal oxide exhibit low temperature decomposition at 550-85°C¹⁷⁰. WO_3 synthesized via thermal deposition technology have shown to have high level of oxygen vacancies and mixed oxidation states¹⁶⁷. Here, thermally deposited WO_3 films were grown from powder hydrotungstite (H_2WO_3) under vacuum condition (10mtorr) in the chemical vapor deposition system.

Requirements: Hydrogen gas, Argon, methane, chemical vapor deposition system, three electrodes system, tungsten, hydrotungstite powder, copper foil, silicon wafer, polyethylene terephthalate (PET), lithium perchlorate, ethylene carbonate, Indium tin oxide on glass substrate and polymethylmethacrylate (PMMA)

5. 3. 0 Tungsten (VI) oxides

Tungsten trioxide a yellow powder with the monoclinic crystal structure (mp32, space group $p1/2/c1$ have tungsten cation (W^{VI+}) at octahedral position and oxygen anion (O^{2-}) at trigonal planar position). Tungsten trioxide is the ore for tungsten synthesis. Tungsten trioxide occurs naturally as hydrates (tungstite ($WO_3 \cdot H_2O$), meymacite ($WO_3 \cdot 2H_2O$) or hydrotungstite (H_2WO_4) nature as

5. 4. 0 Thermal deposition of tungsten trioxide

Ceramic bolt with 30mg of tungsten (VI) oxide was inserted into the furnace and copper foil substrates were inserted at both ends of the quartz as shown in diagram 1 below. The furnace was set at $10^\circ C$ per minutes up to $900^\circ C$ and the pressure was 10mtorr. CVD system was held at $900^\circ C$ for 10 minutes and the furnace was turn off under vacuum to cool down to room temperature. The Copper substrate with the deposited WO_x was removed and the copper etched away before analyses of free suspended WO_x thin film.

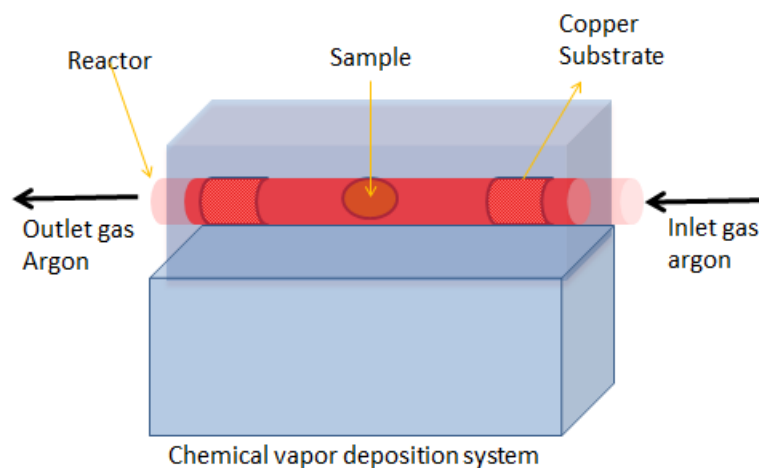


Diagram 5.1. Chemical vapor deposition of tungsten oxide from tungsten trioxide powder

The WO_x -copper foil was coated with PMMA and etched away in iron (III) chloride solution. The suspended thin film of WO_x was fished out using silicon dioxide wafer. The synthesized WO_x was oxidized further in air at 500°C for 15 minutes to synthesize WO_3 thin film.

5. 4. 1 Field emission scanning electron microscopy of WO_3 nanorods film

The synthesized WO_x film was purple in color an indication of W (V) or mixed state of tungsten. XRD analyses indicated that the thin film contain both W (V) and W (VI) oxidation state. The etched WO_x thin film was blue in color an indication that the transferred material is $WO_3 \cdot xH_2O$ (silicon dioxide wafer). Attempt to reduce (bleach) the colored WO_3 in the process of etching failed. The thickness and mixed oxidation states of the material were the suspicions attributed to the failure in bleaching and coloring of the material. So to solve the problem of mix oxidation states, the material was annealed in air at 500°C which turn from blue to white WO_3 thin film. Fabricated ECD with the further annealed WO_3 thin film yield no coloring and bleaching results. The ECD

device was performed using the thermal deposited WO_3 nanorods film in lithium perchlorate as the electrolytes and sulfuric acid electrolytes solution.

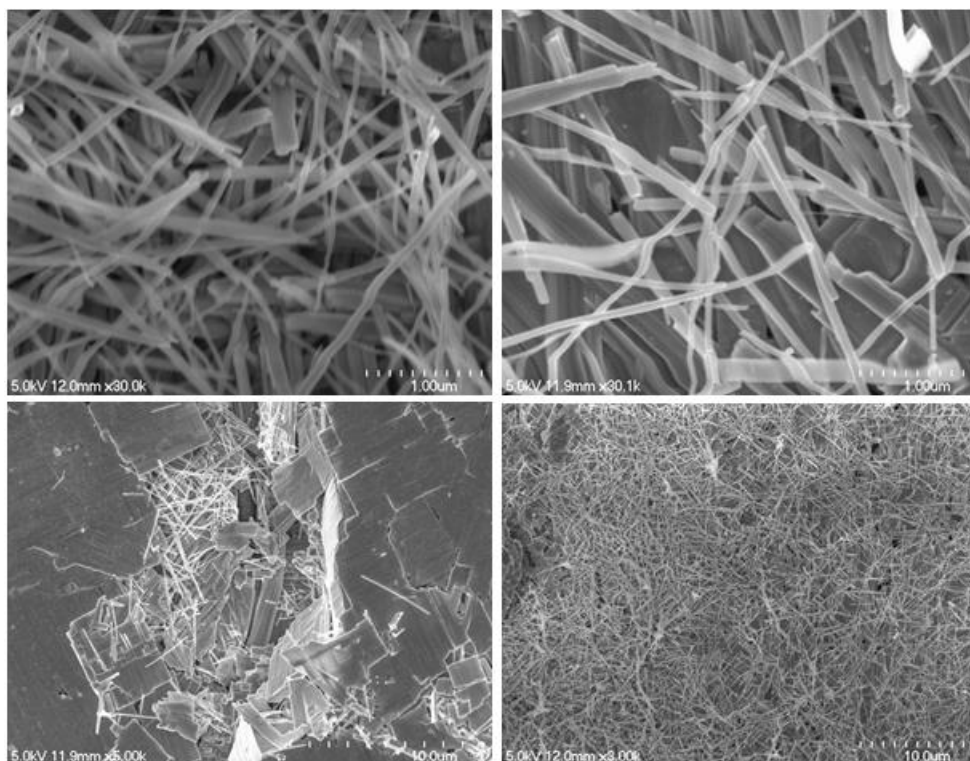


Figure 5.0. Field emission scanning electron micrographs of WO_3 thermally deposited WO_3 before etching (a), after etching (b) and after annealing in air (c & d).

The synthesized WO_3 on copper substrate, etched and annealed in air was transferred onto graphene conductive transparent electrode and attempted bleaching in lithium perchlorate solution did not occurred. The thickness of the thermally deposited WO_x , the etched $\text{WO}_3 \cdot x\text{H}_2\text{O}$ and the annealed WO_3 thin film for bleaching and coloring could be the possible reason for the device failure in addition to vacancies. Several attempts such as the time of deposition and the temperature were made to control the thickness but were unable. It was resolved that electrochemical deposition of WO_3 thin

film on the graphene conductive-transparent electrode will be the best option to engineered thin transparent WO_3 film for ECD.

5. 4. 2. Synthesis of bilayer graphene.

CVD of single layer graphene on different transition metals has been well studied. Graphene has been synthesized from different carbon sources such as gases, liquid or solid carbon precursors. Bilayer graphene on the other hand has not been well explored but has been demonstrated to grow on copper and nickel foil using acetylene and methane. Bilayer graphene has been grown from acetylene on nickel and methane on copper. In this study, extensive study on the growth of bilayer graphene on copper using methane precursor and acetylene were performed. CVD of graphene on copper is a catalytic process that is inhibited by the first graphene layer. Bilayer graphene growth on copper occurs at high pressure (1torr). It's been shown that the second layer of graphene infiltrate between the catalytic copper substrate and the first layer of graphene.

Stripes of copper foil were clean for 1 minute in acetone, 10 minutes in acetic acids, rinsed in deionize water and then ethanol. The clean copper substrates were inserted in the CVD reactor. The CVD system was set to 10°C per minute increase up to 1000°C . Copper foil was annealed in hydrogen (3sccm) for 30 minutes at 1000°C with pressure 54mtorr. The growth conditions were adjusted such that the flow rate of hydrogen 9sccm and methane 9sccm (1.10tor) for 60 minutes at constant temperature and the reactor was rapidly cold down to room temperature⁸⁰⁻¹⁷¹. The synthesized bilayer graphene was transferred onto polyethylene terephthalate (PET) via spin coating with PMMA. The copper coated with graphene was spin coated with PMMA and cured on the hot plate at 180°C for 90 seconds. The coated copper graphene substrate was then

suspended on the surface of acidified iron (III) chloride solution for 30 minutes. The etched graphene in iron (III) chloride was fished out using glass slide onto deionize water for cleaning. This step was repeated three times before fishing out the bilayer graphene with PET substrate. The PET with graphene PMMA on it was inserted into a beaker with acetone to dissolve the spin coated PMMA^{76,172-173}. The bilayer graphene spin coated with PMMA was transferred into 1M hydrochloric acid solution for 30 minutes to dissolve any iron oxide and un-etched metal. After immersing the substrate in acetone, the sample was rinsed in deionize water, dried in the oven at 50°C for 10 minutes and inserted into 1 M ammonium hydroxide solution to oxidize any amorphous carbon on the graphene. Final rinsing was done in clean deionize water three times to remove all the ions and anions that could function as doper on the graphene.

5. 4. 3. Electrochemical deposition of WO_3 on graphene

The bilayer graphene on PET substrate was connected into a three electrode cell system. The anodic electrode was graphene for electrochemical deposition of WO_3 and the cathodic electrode was tungsten (source of the tungsten) and reference electrode was platinum. 1M lithium perchlorate solution dissolved in purged propylene carbonate (PC) (source of protons as well as electrolytes). The potential used in this deposition was 0.5volt. The average experimented deposition time was 10 minutes. The same potentiostat used in chapter 2 and 4 was used for experimenting. The absolute time for effective deposited WO_3 thickness obtained by analysis of WO_3 deposited on indium-tin oxide (ITO) PET conducting substrate. The rate of WO_3 deposited were experimented both ITO and graphene substrate. ITO is efficiently more conductive on PET than single layer graphene as a result of substrate acting as a doping material which was prove by stacking more than single layer with conductivity increasing with the number of graphene

on PET. It was shown that the conductivity of graphene on PET is inversely proportional to conductivity as well as rate of electrodeposition of WO_3 . This work will place bilayer graphene electrode in a competitive region with the well-studied ITO electrode for transparent electrode and sensor devices. The deposited WO_3 thin films were characterized and used to fabricate ECD for smart windows, flexible televisions screens and computers, phones, iPod screens.

5. 3. 4 Characterization of electrodeposited WO_3 on bilayer graphene

The synthesized WO_3 thin films on graphene substrates were analyzed using FE-SEM. The micrographs shown in figure 5.5 below as well as WO_3 thin film grown on ITO substrates were obtained using SEM. Analyses show that the thicknesses of WO_3 thin films grown on ITO substrate were directly proportional to the amount of time exposed for electrochemical deposition. This effect was not directly observed for all the graphene substrates. This may be attributed to the irregularities involve each transferred bilayer graphene. In some cases, the thicknesses of the electrochemical deposited WO_3 were proportion with time (4 layers graphene) some substrates did not have a direct relationship (2layers, 5 layers and 6 layers). We used multi-meter to estimate the electrical conductivity of the graphene by measuring the resistance of the materials. Our results show that conductivity increases with increased in the number of graphene layers. This was obvious given that the first layer graphene is highly doped by the substrate (PET) subsequent layers do not have the same doping effect from the PET substrate.

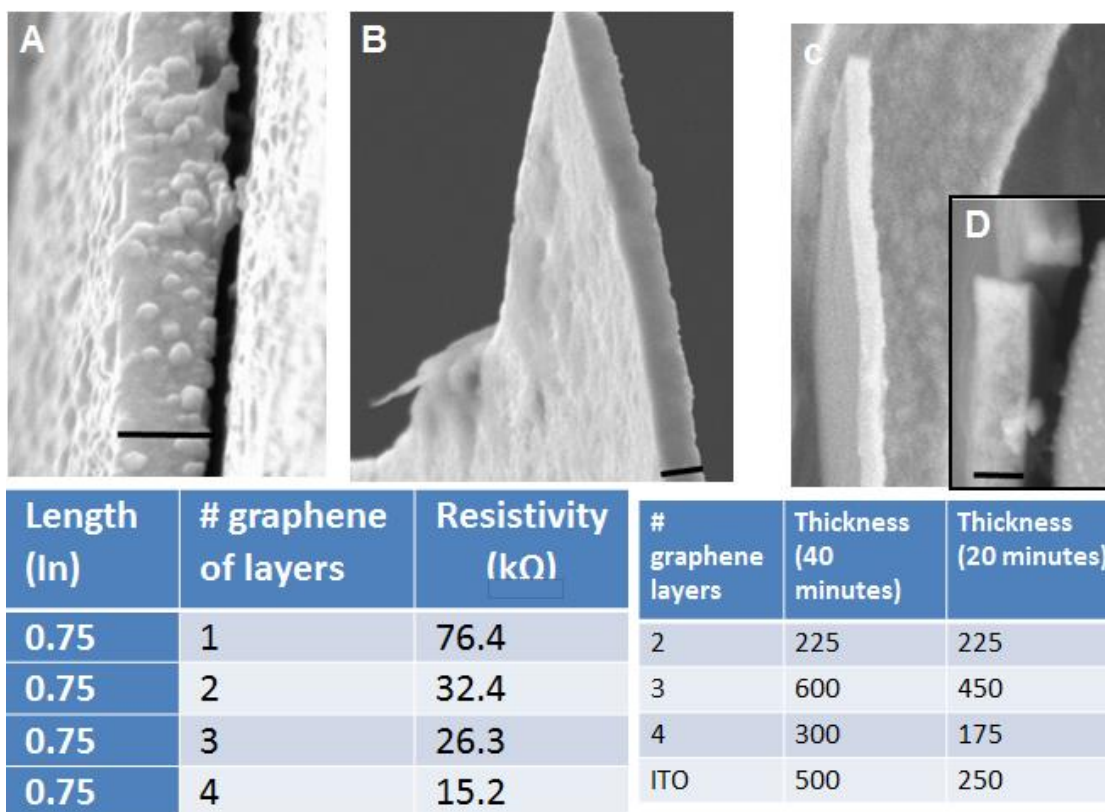


Figure 5.1. Field emission electron micrographs show the thicknesses and resistance of the electrodeposited tungsten trioxide thin film. The thickness of tungsten trioxide depends on the length of deposition and conductivity of the electrode increases with number of graphene layers up to 4 layers of graphene. (a-d) depicts micrographs of WO_3 deposited on three layer graphene for 10 minutes and table included in the figure are how time and conductivity affects the thickness of WO_3 grown.

Base on the analyses, 10 minutes of deposition of WO_3 on graphene as well as ITO yield the thickness of 300nm. All WO_3 growth for ECD was performed for 10 minutes allowing graphene and ITO electrode results comparable. This conclusion is based on figure one above results.

5. 5. 0 Analysis of WO_3 thin films

PANalytical-Empryean diffractometer (40Kv/44mA), Raman spectroscopy (DXR microscope 532 nm filter), Field emission scanning electron microscopy (Hitachi S4700 FE-SEM) and 660C Potentiostat/Galvanostat (CH Instruments) technologies were employed in the analyses and in the syntheses of WO_3 thin film. Field emission scanning electron microscopy was used to study the morphology of the thermal deposited WO_x and the electrochemical WO_3 .

5. 4. 1 Scanning electron microscopy study of the synthesized WO_3 thin film

X-Ray diffraction and Raman spectroscopy have been used to confirm the synthesis of WO_3 . Raman analyses shown in figure 5.3 below gave the finger print Raman peaks for WO_3 materials. Commercially available WO_3 powder analyses also confirmed our Raman analyses of WO_3 thin film. The XRD result also support that the synthesized material is WO_3 . Figure 5.2 are FE-SEM micrographs of electrochemical deposited WO_3 on graphene and indium-tin oxide. The topography and crystallinity of the electrochemical deposited WO_3 on graphene and ITO depict no difference but the same quality. These findings make the comparison of WO_3 grown on ITO and WO_3 grown on graphene meaningful for the ECD.

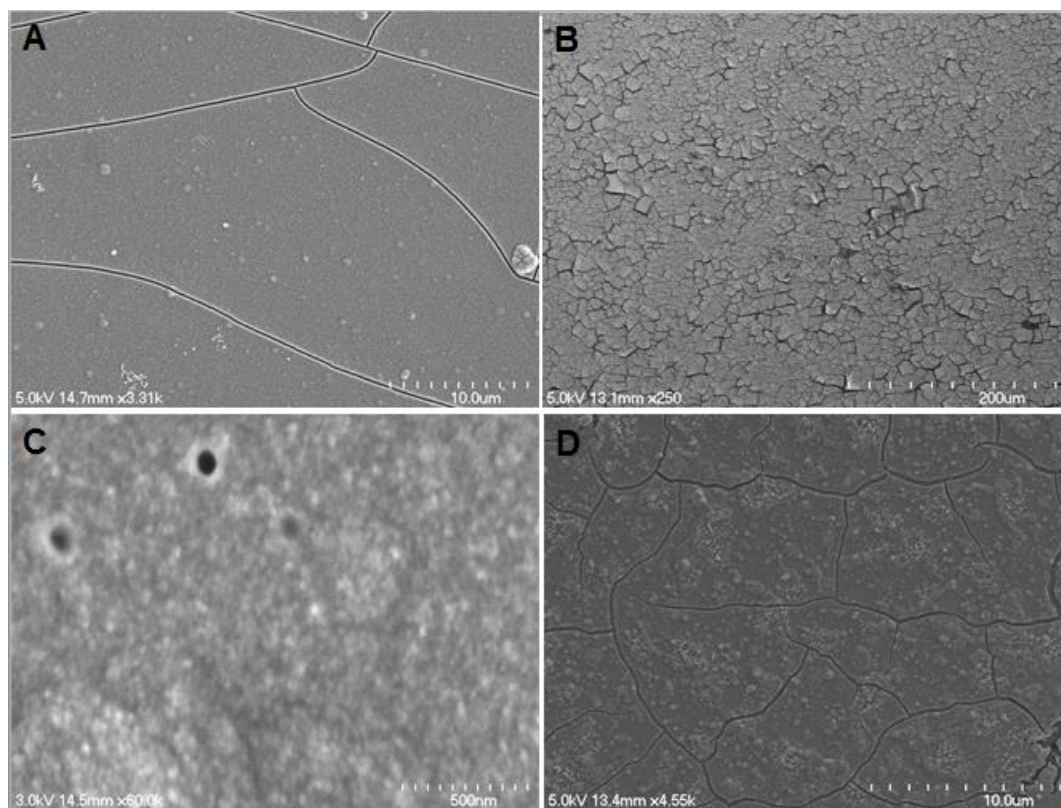


Figure 5.2. Field emission scanning electron micrographs of tungsten trioxide electrochemically deposited on graphene and ITO are the same.

5. 5. 2 X-Ray diffraction study of the synthesized WO₃ thin film

The cracks observed on both graphene and ITO substrates are the result of stress generated during the evaporation of the solvent and the difference in the surface energy of graphene or ITO with the electrodeposited WO₃ on the substrate¹⁷⁴.

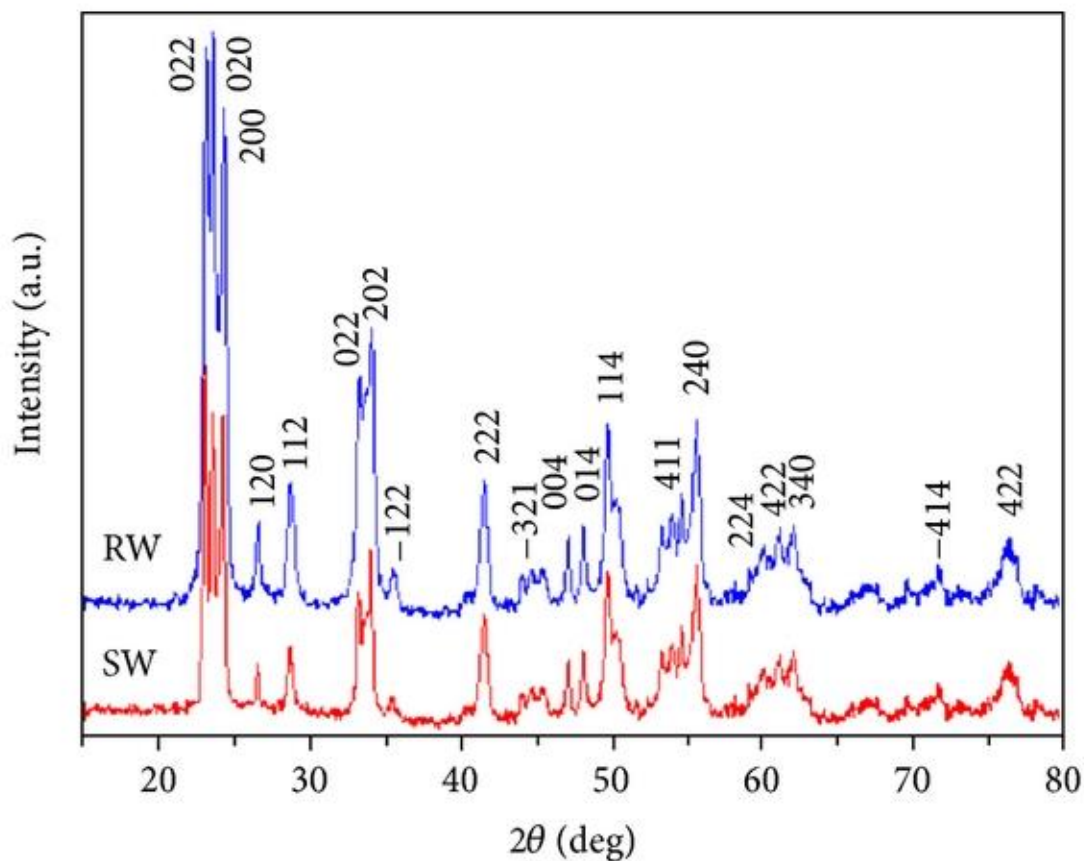


Figure 5.3. X-Ray diffraction of electrochemical deposited tungsten trioxide on graphene commercially available tungsten trioxide powder. The XRD spectrogram above is those of commercial WO_3 powder (black) and XRD of the electrochemical deposited WO_3 on graphene (red).

Commercial WO_3 was poured onto the glass substrate for the XRD analysis while the synthesized WO_3 on graphene and ITO was measured directly on the graphene or ITO substrate¹⁷⁴⁻¹⁷⁵. This finding matches our SEM analyses in figure 5.2 above.

5. 5. 3 Raman spectroscopy analysis of WO_3 thin film

Analyses of WO_3 with Raman spectroscopy was performed on the WO_3 material as synthesized. Figure 5.4 below depicted Raman analyses of WO_3 on graphene the same as on ITO¹⁷⁶. Raman analysis of WO_3 has been well studied with same result showing the in plane and out of plane vibration of the W-O bonds^{168,176}.

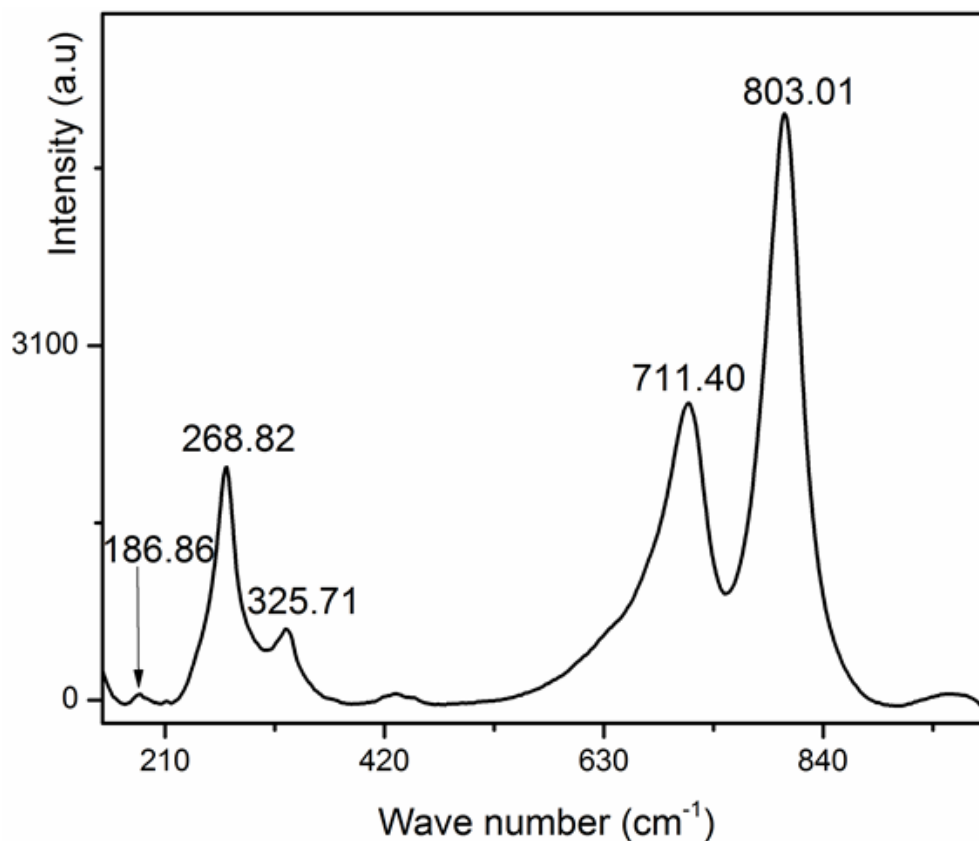


Figure 5.4. Raman studied of tungsten trioxide thin film electrodeposited on graphene substrate.

5. 5. 4 Raman spectroscopy analysis of bilayer graphene

The synthesized WO_3 thin film on graphene was dried in the oven at 50°C for 20 minutes. The Raman spectrum above confirmed that the synthesized material was WO_3 because of the O-W-O bending mode vibration (186cm^{-1} , 268cm^{-1} and 325cm^{-1}) and

stretching mode of the O-W bonds observed (711cm^{-1} and 803cm^{-1})^{174,158}. The chemical vapor deposited bilayer graphene grown on copper foil was analyzed with Raman spectroscopy as shown in figure 5.5 below. Bilayer graphene has been studied for transistors sensors but has not been used as an electrode in electrochemical deposition^{24,171}.

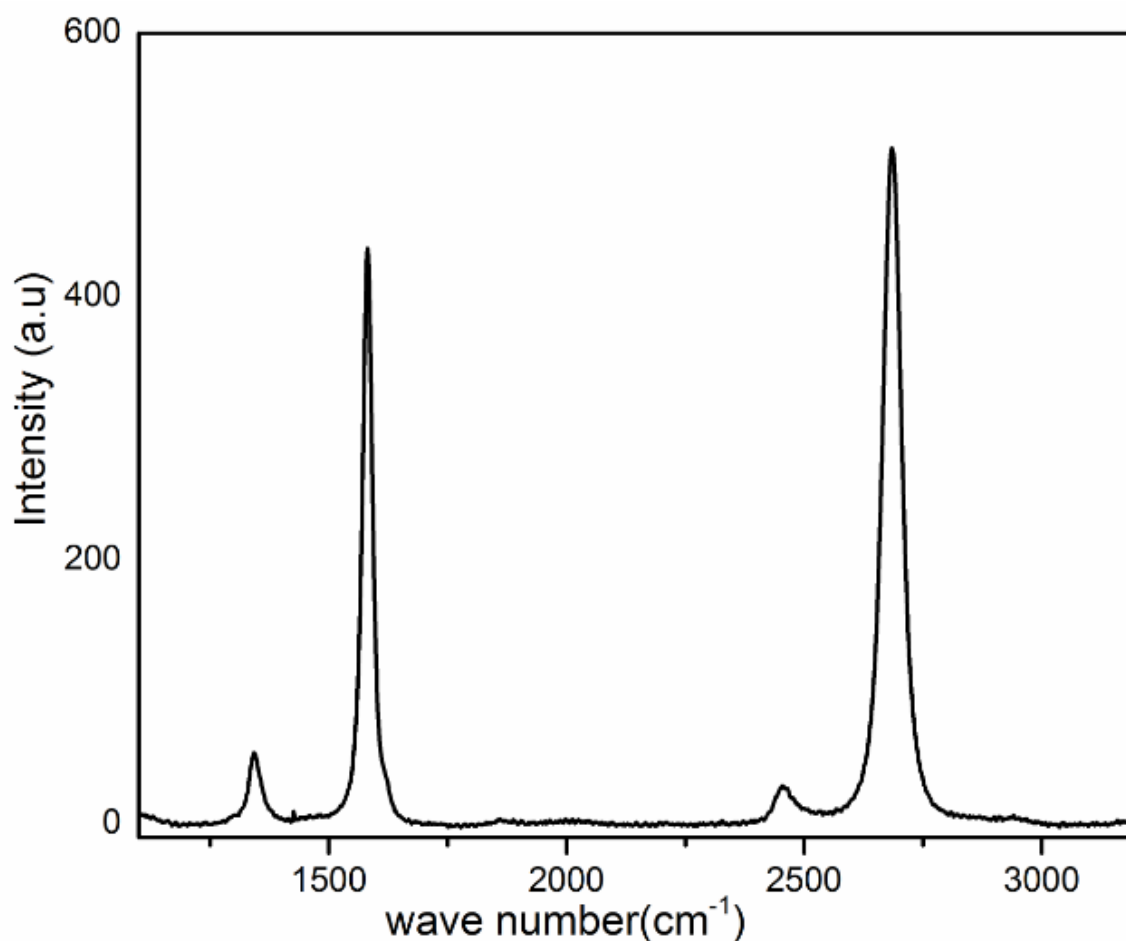


Figure 5.5. Raman spectrum of bilayer graphene grown on copper and transferred onto silicon dioxide wafer

Characteristic of bilayer graphene is that the ratio between the G-band and the 2D-band is always one^{76,171}. The calculated ratio the intensity of the G-band and 2D-

band of the synthesized graphene was 1 confirming that we synthesized and utilized bilayer graphene in this project.

5. 6. 0 Electrochromic analyses

WO_3 has been electrochemically deposited and used in electrochromic devices¹⁷⁷. Liquid electrolytes (sulfuric acids) have been used as the electrolytes and intercalating agent. Sulfuric acid is a strong acid as such not a good electrolyte for smart windows. Lithium perchlorate has been well studied and used as the electrolytes both in liquid and in solid ECDs. As solid gel, lithium perchlorate is mixed in propylene carbonate as solvent with polymethylmethacrylate (PMMA) as the solidify reagent^{160,177-178}.

Lithium perchlorate gel electrolyte is robust for this work because it enables bending of the device flexible to suit its application as computer screens. 1 M solution of lithium perchlorate was prepared in 10:1 %weight propylene carbonate and PMMA respectively. The solution was poured between two electrodes one of which is the graphene WO_3 electrode and the graphene electrode with no WO_3 grown on it as shown in diagram 5.2 below. The device was then cured on hot plot at 50°C for 10 minutes. Polymerization of PMMA and PC encapsulate the lithium perchlorate conducting electrolytes with the gel. The gel also functions as the separator keeping the two electrodes apart. Diagram 5.2 below depicts the system in place for the fabrication of the ECD with graphene WO_3 electrodes.

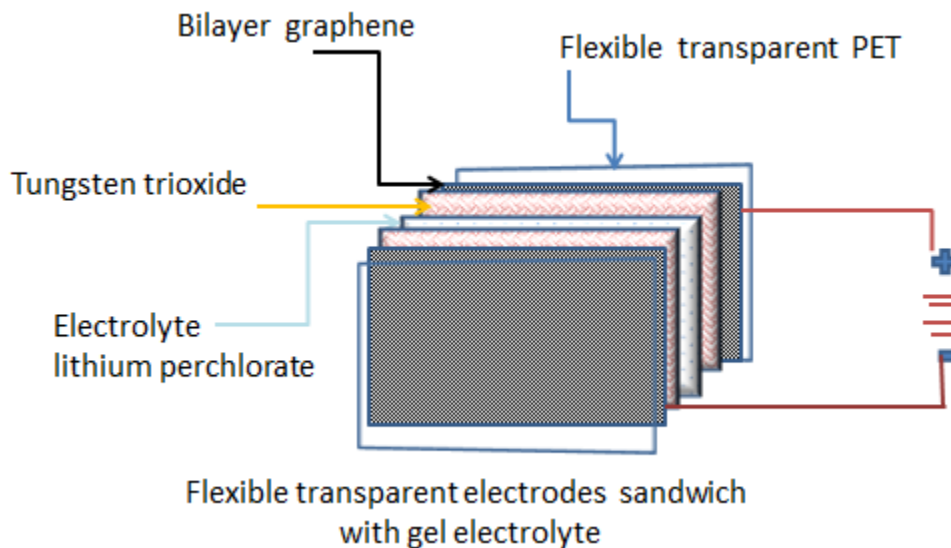


Diagram 5.2. Schematic of the fabricated electrochromic device using graphene-PET substrate with electrodeposited WO₃ the active electrochromic material.

Observed results demonstrated that the application of electrodeposited WO₃ on graphene on PET can be the formidable material in EC industries. While we are in the process of finalizing our findings, figure 5.6 below represent the competitive nature of graphene with ITO in the feature of ECDs electrodes and in electronics and sensors devices.

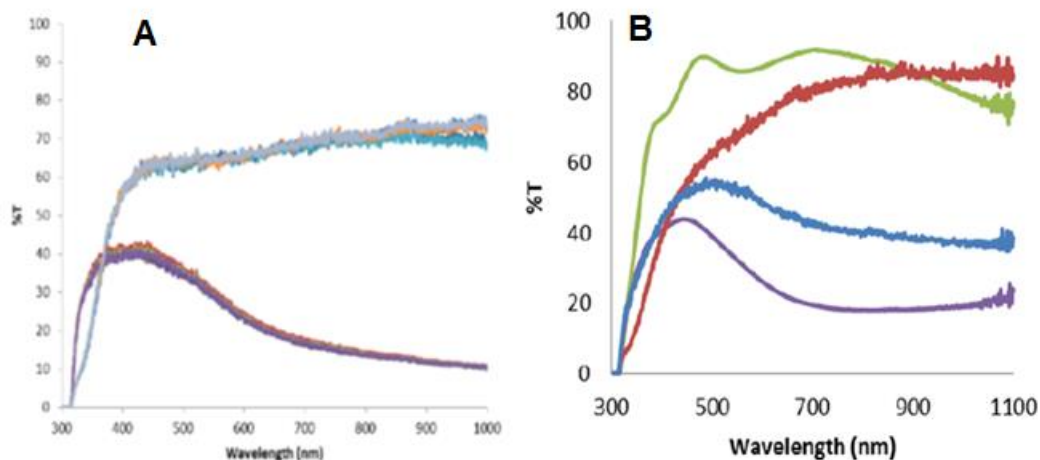


Figure 5.6. Electrochromism of the fabricated device is shown by the coloring and bleaching of WO₃ using lithium perchlorate gel. (a) WO₃ on graphene depicted above the bleaching transmittance around 20% and coloring transmittance around 80% of light over full spectrum and (b) WO₃ on ITO depicted above the bleaching around 40% transmittance and coloring transmittance around 80% of light over full spectrum.

Figure 5.6 above shows that WO₃ bleaching and coloring on graphene is more effective because the % transmittance of the ECD remain almost constant as the graphene device was recycled but a change with ITO device was recycled. These are preliminary results that are not necessary the true representation of the functionality of WO₃ graphene device compared with existing WO₃ ITO device.

5. 7. 0 Conclusions and future work

Flexible ECD of WO₃ graphene have shown progress in applications which can only be confirmed to a limited degree until subsequent work is completed. Different set of devices are in progress that will enable the analysis to determine the flexibility of the fabricated ECD with graphene on PET.

Chapter 6

New three dimensional graphene and graphene like materials with high specific surface area for energy storage

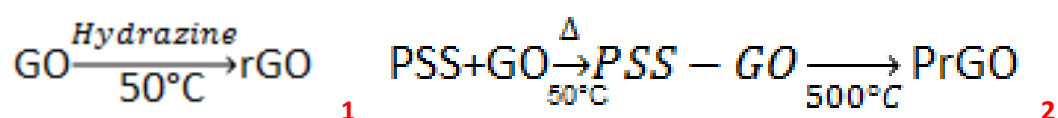
6. 0. 0 Reduced graphene oxide composites for energy storage

Graphene oxide initially known as graphite oxide (GO) was first synthesized in 1859 by Benjamin C. Brodie using potassium chlorate in fuming nitric acid¹⁷⁹. The chemical exfoliation technique of graphene oxide from graphite was modified in 1957 by Hummer. He used graphite in hot potassium permanganate, sulfuric acid and sodium nitrate now known as the Hummers 'method'⁵³. The beauty of chemical exfoliation of GO is the ability to scale up reaction and the properties of GO. GO can be reassemble into a high stable, high tensile strength, conductive and transparent thin film suitable for sensors and energy related devices^{103,180-181}. Why GO brought glimpse of hope to researchers of graphene, it has its limitations such as poor electrical conductivity attributed to the high oxygen doped graphene. Secondly, its ability to restack itself due to pi-pi interaction between the graphene sheets reducing specific surface area of the material. To solve these problems, different reduction methods (reducing agents) have been used to reduce the concentration of oxygen on GO resulting into a new material known as reduced graphene oxide (rGO). Among the numerous methods of graphene oxide reduction are, thermal reduction¹⁸²⁻¹⁸³ and hydrazine¹⁸⁴⁻¹⁸⁵ but hydrazine reduction has been the most efficient methods. This method has failed to address the issue of restacking of the graphene sheets. Improving the electrical conductivity of the chemical exfoliated graphene oxide, we propose a method that will prevent restacking of the

graphene nanosheets and reduced oxygen doping there by increasing specific surface area and electrical conductivity¹⁶.

To Increase the specific surface area for rGO, the use of the already synthesized PSS (chapter 1) as suspenders to prevent restacking of rGO sheets during hydrazine reduction of GO¹⁸⁴ equation 1. To remove the PSS from rGO, the composite material was immersed into toluene for 30 minutes to leach out the PSS. The composite was analyzed using optical microscopy for PSS (SEM images (Figure 1)). The wrapped GO prevent the penetration of toluene from dissolving PSS⁵⁹. The result indicated that not all the PSS dissolved in toluene because toluene does not penetrate graphene. To solve this problem, the composite material was annealed at 500°C to decompose PSS resulting into porous reduced graphene oxide (prGO) instead of immersing the composite in toluene. PSS was removed using thermal treatment of the GO-PS composite at 500°C in vacuum for 30minutes equation 2. Figure 2 depict the thermally reduced porous graphene oxide (prGO) scaffold synthesized by using PSS as suspenders to prevent restacking of rGO. This will increase the porosity of the prGO material scaffold consequently increases the specific surface area of this prGO and channel for flow of electrolytes. After analyzing the material at 500°C, the specific surface area was determined using BET technique for both rGO and prGO. Specific surface area results indicated that the prevented rGO from restacking using PSS (prGO) exhibit low SSA compared with the solution hydrazine reduction method. This conclusion was solely based on our BET results (Table 1 below). This method could be improved by increasing the concentration ratio of PSS over GO and secondly by optimizing the method of leaching PSS out of the GO scaffold through temperature gradient and the conditions of leaching in hydrogen to facilitated thermal reduction of

GO. The use of small size PSS in diameter as suspenders (5-10nm) compared to the used 180nm PSS will allow the PSS to infiltrate much better between GO nanosheets preventing restacking better than larger PSS. This will enable perfect uniform composite PSS-GO material that will eventually yield high microporous prGO material scaffold after the removal of PSS. The prGO material will yield high specific surface area scaffold with high conductivity which can be attributed to the degree of GO reduction.



6. 1. 0 Results and Analyses

The two forms of reducing graphene oxide obtained rGO and prGO exhibit high specific surface area. The analyses were done separately using BET, SEM, Raman and XRD technology. The BET analysis was performed by degasing the material at 80°C for 1 hour and run at 250°C for 12 hours which is the suitable temperature to purge out all the unwanted residual contaminants like water^{41,186}. Table 1 below shows the difference in SSA of the rGO synthesized using the two different methods outline above rGO and prGO.

Table 6.0. The specific surface area of different types of reduced graphene oxide.

| specific surface area of rGO synthesized under different conditions m ² /g | | |
|---|--------------------------|-------------------------|
| rGO (Hydrazine reduction) | prGO (Thermal reduction) | rGO (Thermal reduction) |
| 642.69 | 485.6 | 154.7 |
| 687.61 | 457.7 | 321.4 |

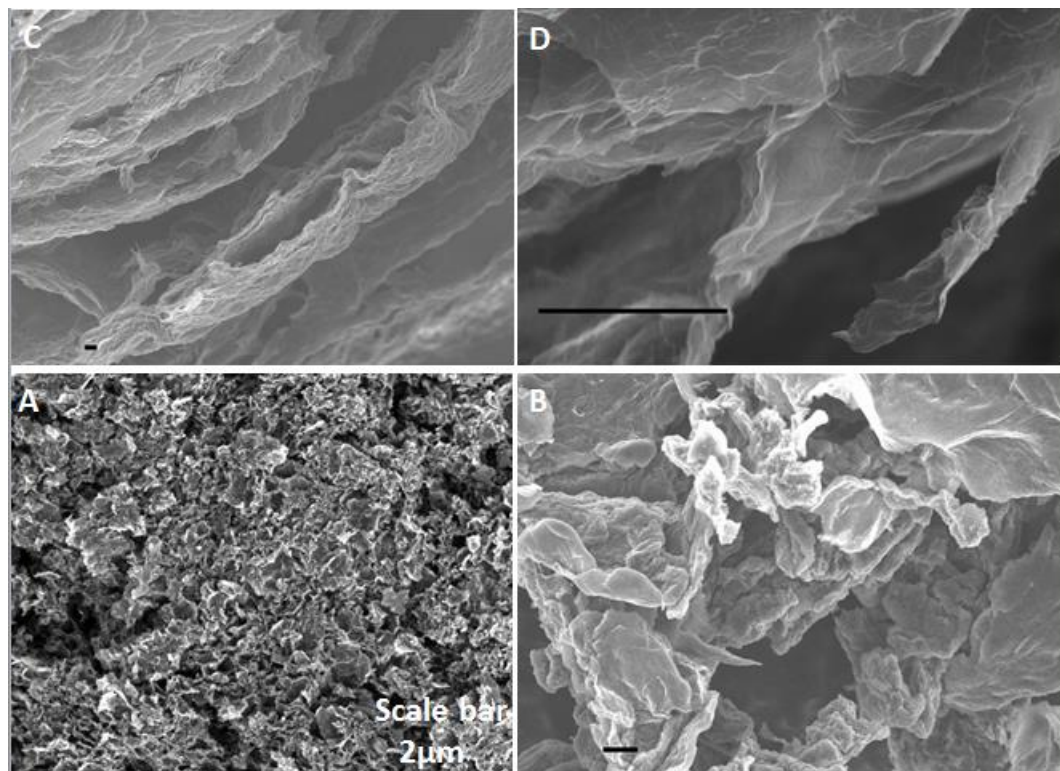


Figure 6.1. Scanning electron micrographs of reduction graphene oxide in hydrazine (a) powder reduced graphene oxide, (b) micrograph of the zoom in powder rGO, (c) side view micrograph showing restacked rGO nanosheets and (b) zoom-in micrograph of few layers of stacked rGO nanosheets.

The hydrazine reduced graphene oxide was washed with water several times and filter using 40nm pore size filter paper and dried over night at 50°C in the oven. The sample was then disperses in deionized water and drop cast on silicon wafer for analyses as shown in figure 1 above. The results illustrated that the decrease in SSA of the rGO is caused predominantly by the restacking due to the pi-pi-bond interaction between the reduced graphene oxide nanosheets figure 1C& 1D and poor reduction of GO into prGO.

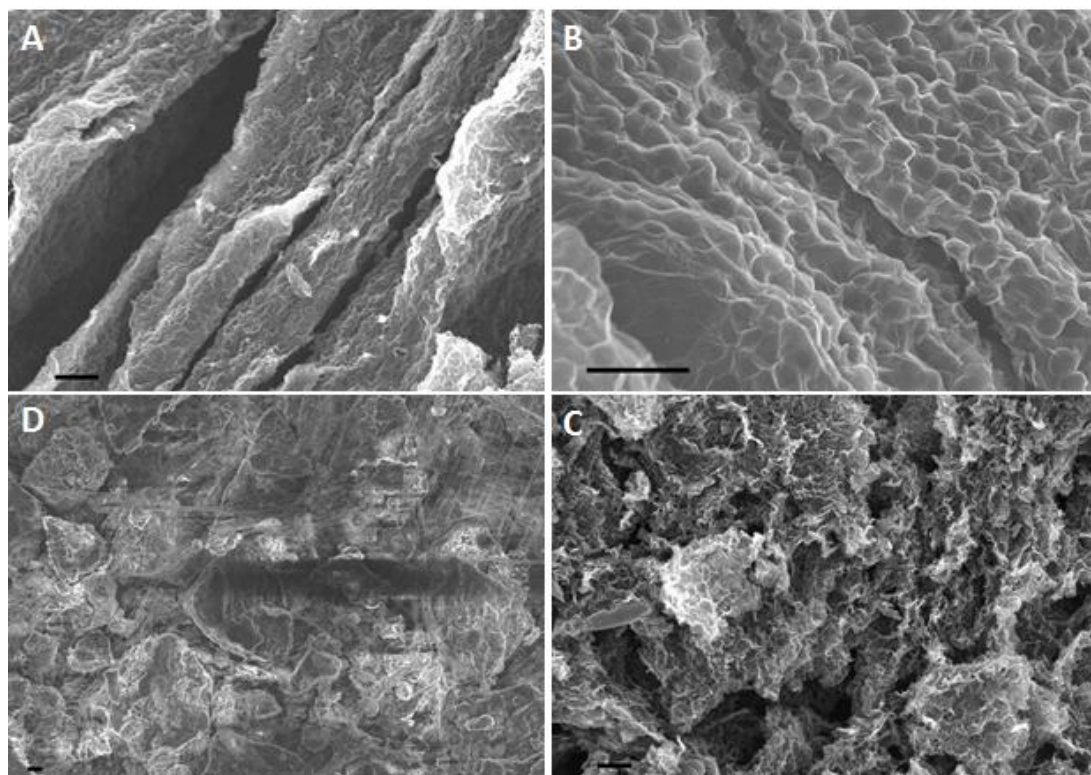


Figure 6.2. Scanning electron micrographs of porous reduced graphene oxide. (A,B & C) depict side view, top view and zoom out on microstructures of prGO and (d) shows prGO mixed with 6%wt of polytetrafluoroethylene (PTFE) for capacitance analyses.

The micrographs in figure 2 above clearly illustrate the pores created by PSS that have been removed via thermal decomposition at 500°C. The prGO scaffolds was then mechanically mixed with PTFE to obtain a semi-uniformed composited (figure 2C) material that was then used to fabricate thin film material that serves as capacitive plates for charge storage.

6. 1. 1 Discursion on reduced graphene oxide

The designed rGO thin films made from mixing 6%wt PTFE with rGO and prGO separately were assembled for capacitance measurement in 1.M sodium sulfate solution

(electrolytes) using two cell electrode system. The electrochemical impedance spectra Figure 3D below indicates that the material had good surface contact with the electrodes^{56,187} indicated by the semi-cycle around 10 ohms. Cyclic voltammetry (CV) shown in figure 3a below indicated that the fabricated material exhibit a low charging to discharging frequency ratio. This phenomenon has been observed and predicted to be as a result of poor free channel for charges mobility within the solution and the electrodes. Chrono-potentiometric measurements (figure 6.3c) shown below support the concept that low rate of charging and discharging exist within the fabricated device which is affected by high scanning rate. Fast scanning rate yield high cyclic time an indication of slow charging and discharging device. The analyzed capacitance as shown in figure 6.3d is low compared to publish rGO fabricated devices⁶⁷. Our result does not reflect the high SSA shown in table 1 above. This could be caused by our poor method of fabricating the device which we intern to improve by improving the quality of the synthesized graphene oxide and the way the device is fabricated. To solve this problem, rGO should be well reduced to improve conductivity, design experimental methods that will lead to higher surface area for the accessibility of the electrolytes.

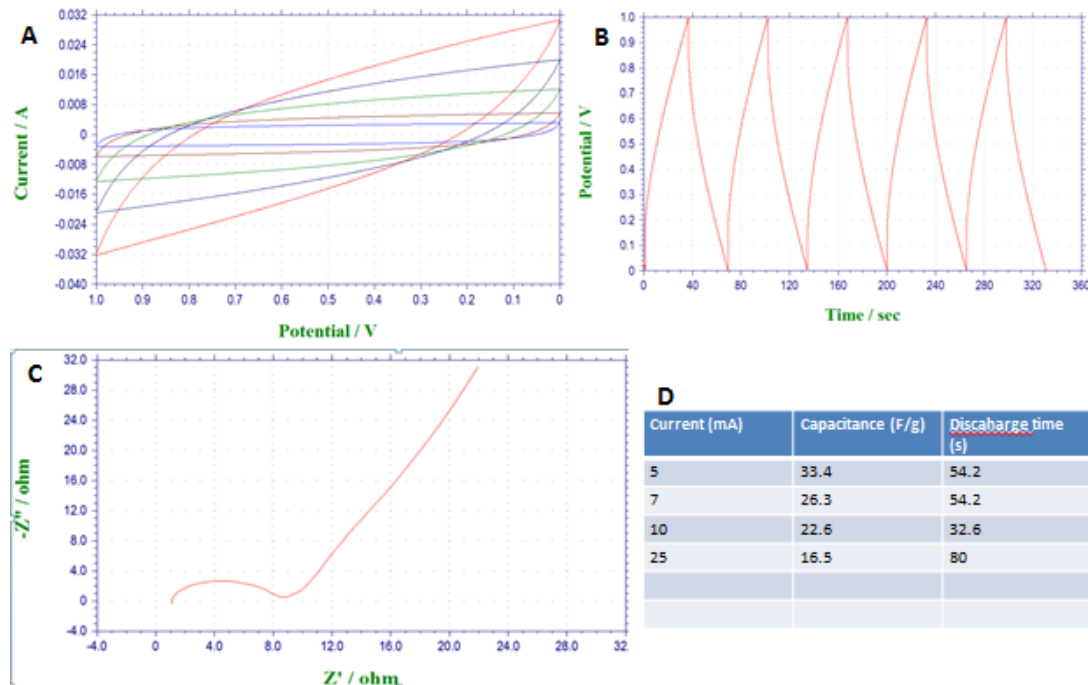


Figure 6.3. Depict the behavior of the fabricated rGO thin films as electrodes for supercapacitive charge storage device. (A) Cyclic voltammogram of the rGO thin film material, b) show the rate of charging and discharging measured using chronopotentiometry method, c) illustrate the adhesion or contact between the thin film material to the electrodes determine based on the electrochemical impedance of the device. prGO material was analyzed using the same methods (6%wt PTFE) as the rGO with the expectation to have low result because prGO exhibit low SSA over rGO but instead the capacitance was 46F/g compared to 33F/g at low scan rate and 5 mA for rGO and prGO.

While new experimental methods to improve the conductivity of the reduced graphene oxide and the porosity of the scaffold need to be design, moving forward, a two-step synthetic method that utilizes nickel sol gel (small particle size) as the suspenders between graphene oxide nanosheets. What makes this proposal so unique,

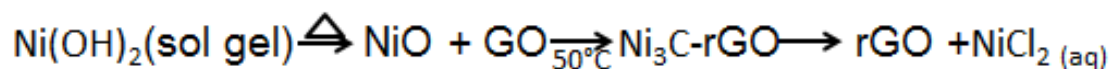
attractive and promising is the ability of nickel sol gel to uniformly disperse and stacks between GO nanosheets and function as the activating agent creating microspores for higher SSA. The size of the nickel hydroxide (25 nm) will have an extra advantage over PSS in infiltrating the graphene oxide solution¹⁸⁸. The objective is to improve the SSA of rGO as well as increased the level of connectivity between reduced graphene oxide nanosheets during thermal reduction under hydrogen environment.

6. 2. 0 Nickel sol gel as suspenders for reduced graphene oxide

6. 2. 1 Introduction and experimentation

Modification of the chemical exfoliation of graphene oxide known as the modified hummer's method was used in the synthesis of graphene oxide with no phosphoric acids as mention in chapter 1. We observed that the role of phosphoric acid in preventing over oxidation of graphene nanosheets has been over started^{53,72}. In a separated set-up experiment, nickel sol gel was synthesized as mention above from nickel nitrate, nickel chloride in diluted ethanol and sodium hydroxide solution. The washed graphene oxide with excessive deionized water was dispersed in (1:1 volume ratio) ethanol-water solution. The salt solution (sodium chloride) was removed from the nickel sol gel using water-ethanol solution (3:1 volume ratio) mixture several times. Homogenous composite mixture of GO and nickel sol gel was prepared by mixing different portions of GO and nickel hydroxide. The composite mixture was stirred for three hour at 300 rpm on the hot plate at room temperature. The composite mixture was filtered using filter paper set-up attached to the water ventilation system. The obtained brownish solid composite material was dried in the oven overnight. The composite turns into a dirty-black composite

material as a result of thermal reduction of nickel hydroxide into nickel oxide and partial reduction of oxidized graphene oxide as shown in the schematic below.



The obtained composite material was treated with hydrogen (3sccm) at 500°C for one hour. At elevated temperature and hydrogen, nickel oxide was completely reduced to metallic nickel and the represent of carbon source (reduced graphene oxide), carbon atoms pitched off from the parent rGO into the metallic nickel. The metallic nickel prevent restacking of the thermally rGO and solubility of carbon into nickel create microspores within the rGO nanosheets resulting into the highly porous reduced graphene oxide (HprGO). The obtained powder composite material was immersed into concentrated hydrochloride acid solution over night to etch the metallic nickel or un-reduced nickel oxide. The resulted HprGO was washed several times with deionized water and dry overnight in the oven at 100°C

6. 2. 2 Analysis of highly porous graphene oxide

The obtained powder (high porous reduced graphene oxide) was ready for analysis and device fabrications. Small portion of the material was mounted on carbon tape for scanning electron microscopy. The micrographs shown below figure 4 depict the physical appearance of HprGO nanosheets. The SEM images show graphene oxide nanosheets grumble together but with low resolution SEM images cannot depict the microspores. Figure 3D also include Raman analyzed spectra that complete support that the material is graphene oxide with an intense D-band. The G-band intensity over the 2D band is an indication of multilayer graphitic material.

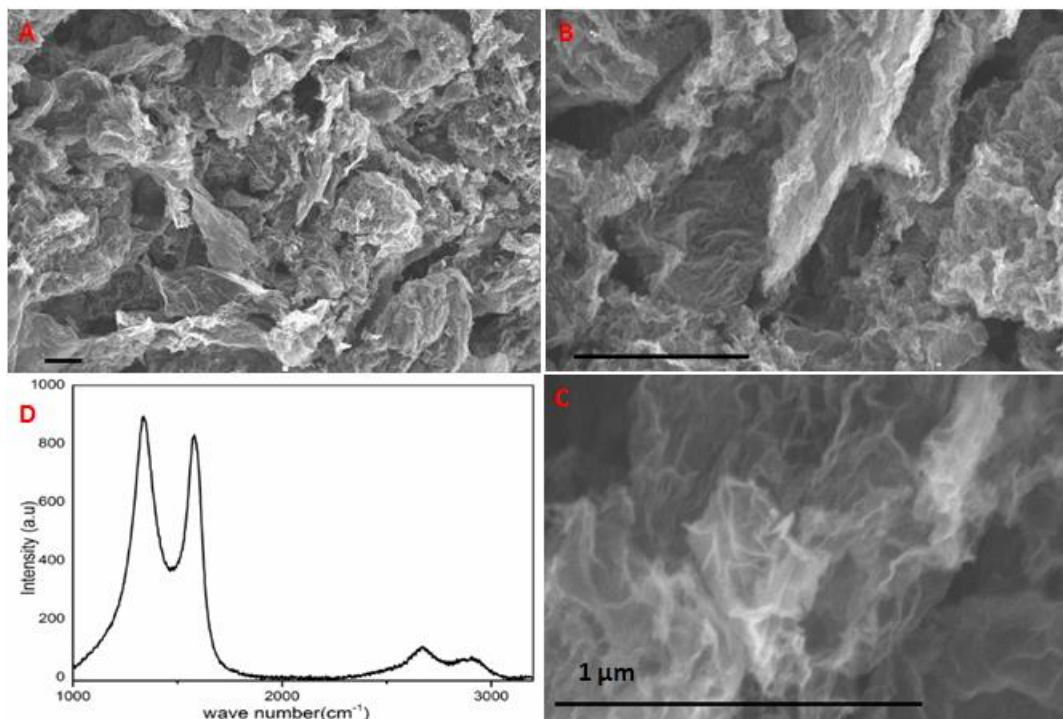


Figure 6.4. Scanning electron micrographs and Raman spectra support that the material is reduced graphene oxide. (a, b, & c) illustrated the microstructure of the highly porous reduced graphene oxide with zoom in images showing high degree of porosity and (d) Raman spectra of the synthesized material.

X-ray diffraction and energy dispersive X-ray analysis were performed to determine the present or absent of nickel/nickel precursor within the powder⁵⁰. Based on our results shown in figure 5 below, the nickel was not completely etched out of the reduced graphene oxide and was also supported by XRD analysis. This means that after etching and washing the product with deionized water, not all the nickel was completely etched away. The EDX also confirmed that not all the nickel was completely removed. The trace amount of nickel shown by EDX and XRD can be attributed to short time of etching and poor washing/rinsing method or it could be attributed to the trap nickel/nickel oxide within the GO nanosheets.

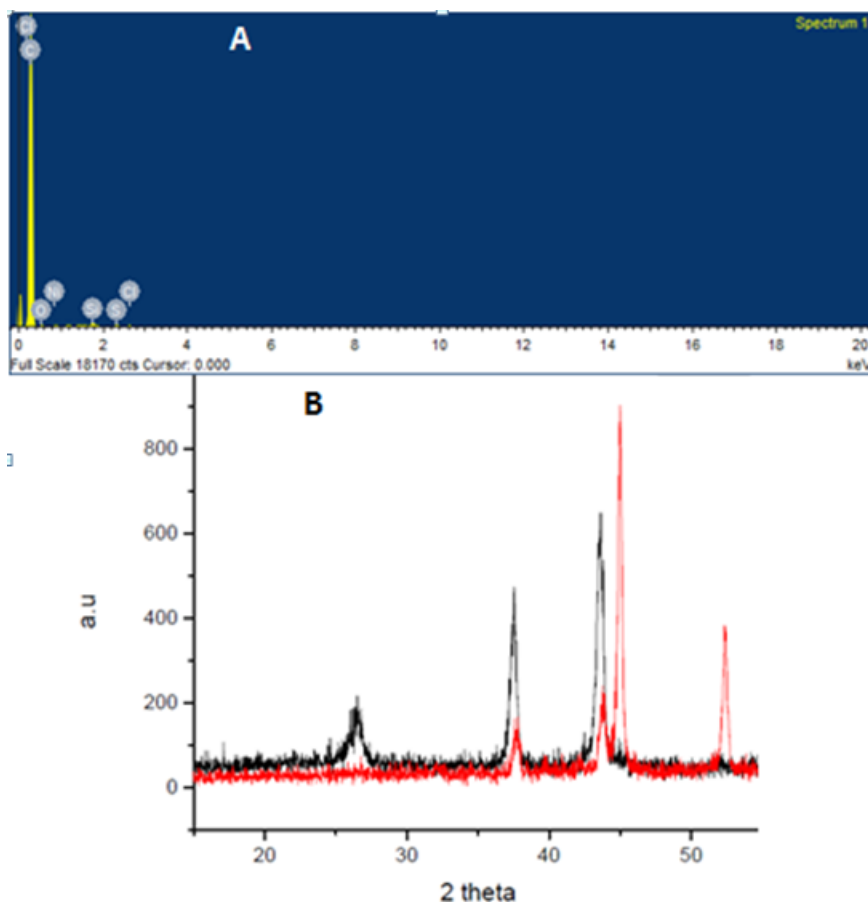


Figure 6.5. Energy dispersive X-ray spectroscopy and X-ray diffraction analysis of the highly porous reduced graphene oxide (a) EDX show small amount of nickel present and (b) XRD show not nickel present.

These results are very important for this project because it established the concept that no nickel could be trapped by graphene oxide hindering etching by hydrochloride acid. Given that nickel has been and is used as metal hydride in energy storage devices, nickel is expensive, heavy and poor charge storage compared to graphene giving the reason for us to completely removed the nickel from the material to qualitatively and quantitatively determine the actual SSA as well as the actual specific capacitance of the new material.

6. 1. 3 Results of highly porous reduced graphene oxide

Brunauer-Emmett-Teller (BET) analysis was performed on the HprGO powder and Raman analysis. The determined SSA did not meet the expectations but point to a very promising direction. While this material gives a low SAA compared with previous material ($324.6\text{m}^2/\text{g}$), HprGO has shown the best result in terms of capacitance analysis for all materials analyzed. The thin film of the highly porous rGO was prepared using the same methods as mention above (powder porous rGO mixed with 6%wt PTFE¹⁸⁹ mixed using mortar and pestle for uniformity and was then fabricated into a supercapacitive device for analysis. The supercapacitance device was then inserted into sodium sulfate electrolytes solution with two electrodes cell set up.

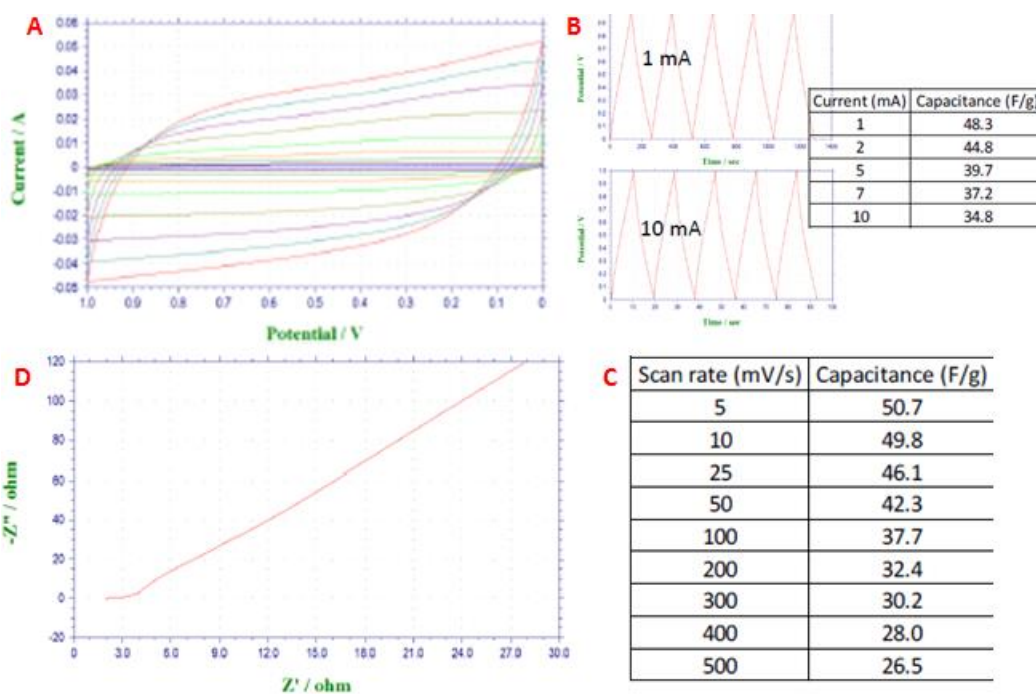


Figure 6.6. Electrochemical analyses of highly porous reduced graphene oxide using two electrodes cell. Figure 6(a, b c & d) provide good understanding and capacitance of the fabricated device. (a & b) provide a faster charging and discharging rate compared with

prGO and rGO, (d) illustrated a better adhesion/ contact between the electrodes and the fabricated thin film as above.

The result confirmed that using nanoparticles such as nickel hydroxide will be the best way to turn graphene oxide into a better material for energy storage devices. To obtain this goal, we will improve the quality of the HprGO material by increasing the concentration of nickel hydroxide, playing with the concentration of hydrogen gas and the reduction temperature to ensure high microspores concentration, macrospores density and good conductivity of the synthesized material. Knowing that the process of transforming graphite into graphene oxide is fast but irreversible, it will be effective to synthesis pristine graphene powder that can be used directly without any reduction steps or doping procedure.

6. 3. 0 **Powder Graphene sol gel**

Graphene which was first synthesized via mechanical exfoliation using scotch tape cannot be synthase in bulk at this moment. Since graphene oxide end up producing heavily doped graphene nanosheets with oxygen, avoiding the doping effect means synthesizing pristine graphene powder. Here we hypothesize how to synthesize pristine graphene powder using nanoparticles. Nickel is the only transition metal that has high carbon solubility and catalyzes the synthesis of few to multilayers graphene. Atomic layer thick nanosheets exhibit high surface energy as a result cannot maintain their structural confirmation except when supported by flat surface. It is not possible to synthesis single layer of few layers of free standing graphene (two dimensional materials) powder that will overcome the high surface energy that causes it to grumble.

In this project we prescribe a synthetic route that will enable the achievement of pristine graphene powder from any doping agent. The synthesized nickel sol gel will be reduced into nickel oxide nanoparticles which will be further reduced into nickel nanoparticles under hydrogen conditions. The nickel nanoparticles will be utilized to synthesize what we call graphene sol gel.

6. 3. 1 Experimental

Nickel sol gel was synthesized as mention above using nickel nitrate, nickel chloride and sodium hydroxide in diluted ethanol. The obtain nickel sol gel was washed several times with deionized water to remove sodium salts by product. After drying the product overnight in the oven at 50°C, nickel oxide nanoparticles were obtain as shown in figure 7 below. Nickel oxide was then place into a ceramic boat and inserted into the chemical vapor deposition system. The powder was annealed at 290°C for 30 minutes to complete reduced all the nickel hydroxide into nickel oxide. The temperature was ramp to 500°C under hydrogen condition (3sccm). The system was health steady at 500°C for 30 minutes and was then exposed to acetylene (3sccm) for another 30 minutes. The system was then turn off to cold slowly to room temperature. The nickel nanoparticles coated with graphene was then poured into highly concentrated hydrochloric acid solution and was allowed to seat for 5 hours. The material was filtered, washed with deionized water and dry at 100°C in the oven overnight. The obtained powder was then analyzed and will be use as energy storage and gas sensors devices.

6. 3. 2 Analysis of powder pristine graphene sol gel

Scanning electron microscopy (SEM) was used to analysis the synthesized powder graphene sol gel. Fig. 7 below show the structures of nickel hydroxide, nickel

oxide, nickel coated with graphene and powder graphene sol gel. SEM images indicated that the nickel coated graphene particles was leach out using hydrochloric acid. The hypothesis is that with defect side on the particles and grain boundaries, it was successful to etch the nickel out of the coated graphene.

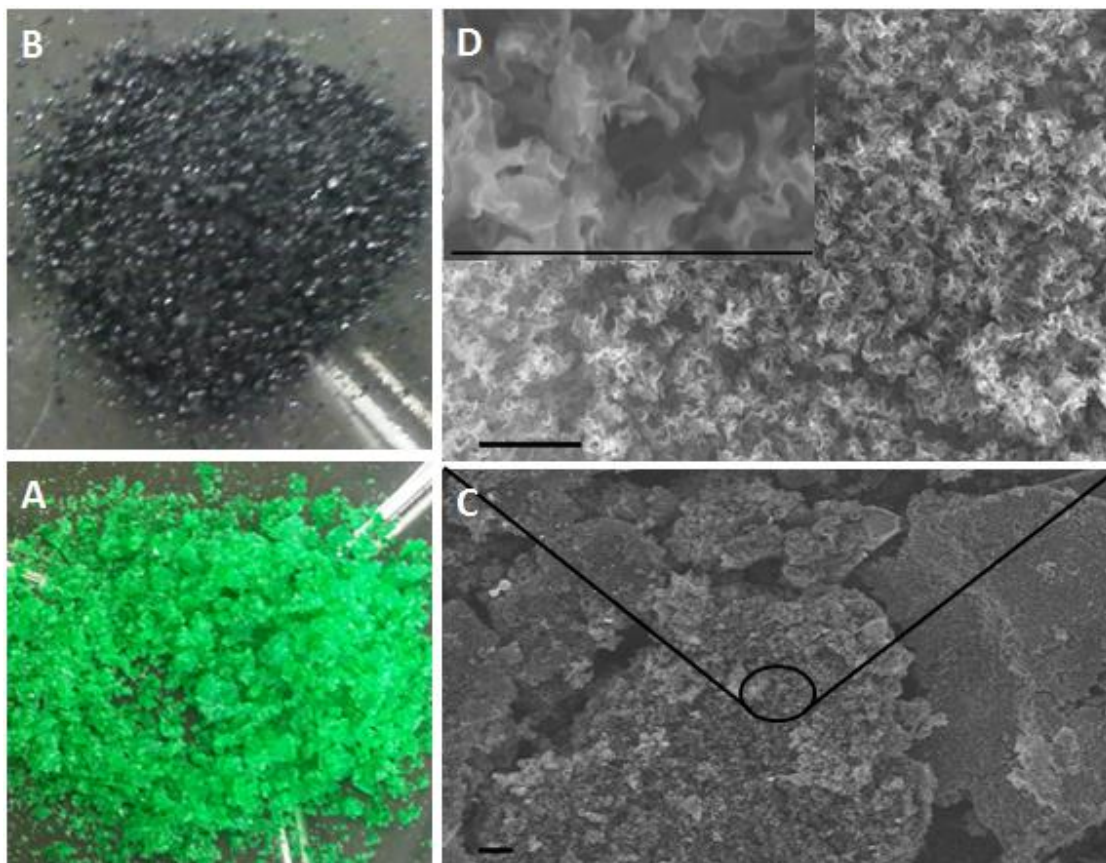


Figure 6.7. Field emission scanning electron micrographs of the synthesized pristine graphene powder. (a) Nickel hydroxide, (b) Nickel coated with graphene and (c & d) graphene sol gel with zoom in image (7d) to illustrate the microstructure of the material.

In addition to SEM, the graphene powder was further analyzed with EDX and Raman spectroscopy figure 8 below. The Raman analysis show highly quality graphene evident by the G-band and 2D-band. The present of D-band around 1100 wave numbers

demonstrate the high degree of defects present which was expected due to rough disrupted edges after acidic etching of nickel.

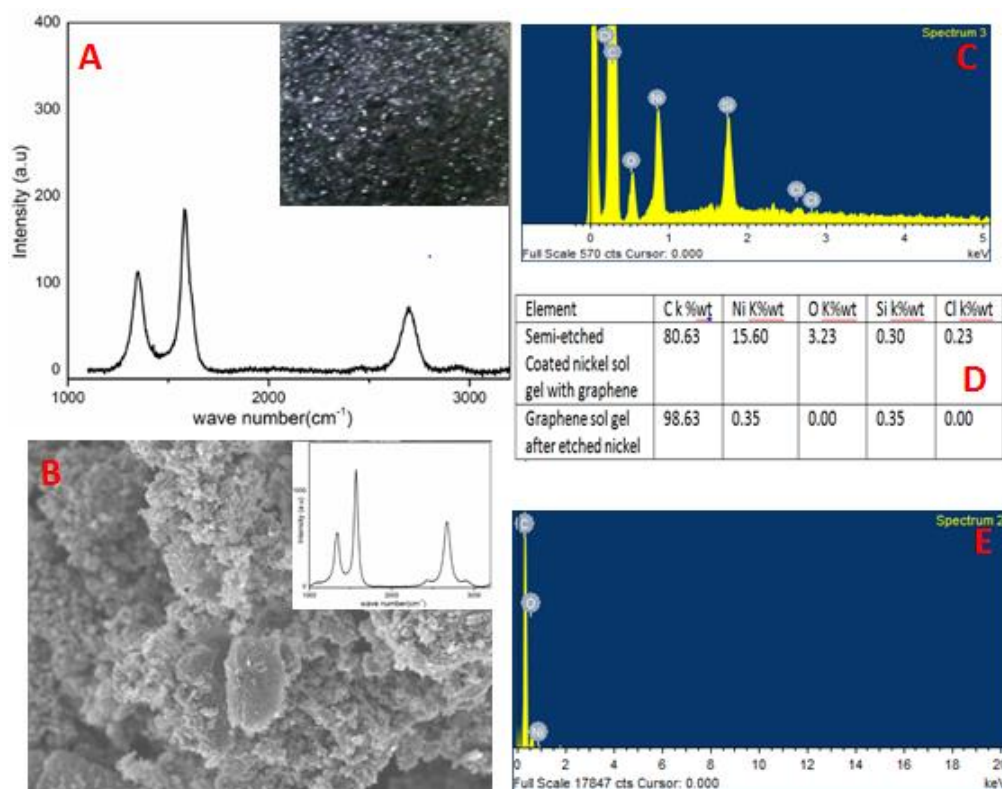


Figure 6.8. Energy dispersive X-ray spectroscopy and Raman analysis of the powder graphene sol gel. (A & C) Raman and EDX spectra of nickel coated with graphene and (B & E) Raman and EDX spectra of etched graphene sol gel powder and (D) EDX elemental composition.

The Raman spectra confirmed that nickel nanoparticles can be used as sacrificial template for pristine graphene powder. EDX elemental analysis support the hypothesis that nickel nanoparticles coated with graphene can be completely etched out using concentrated hydrochloric acid solution generating pure clean graphene powder as

product sensors, energy and biological applications. These findings were further supported by XRD analytical result shown in figure 6.9 below.

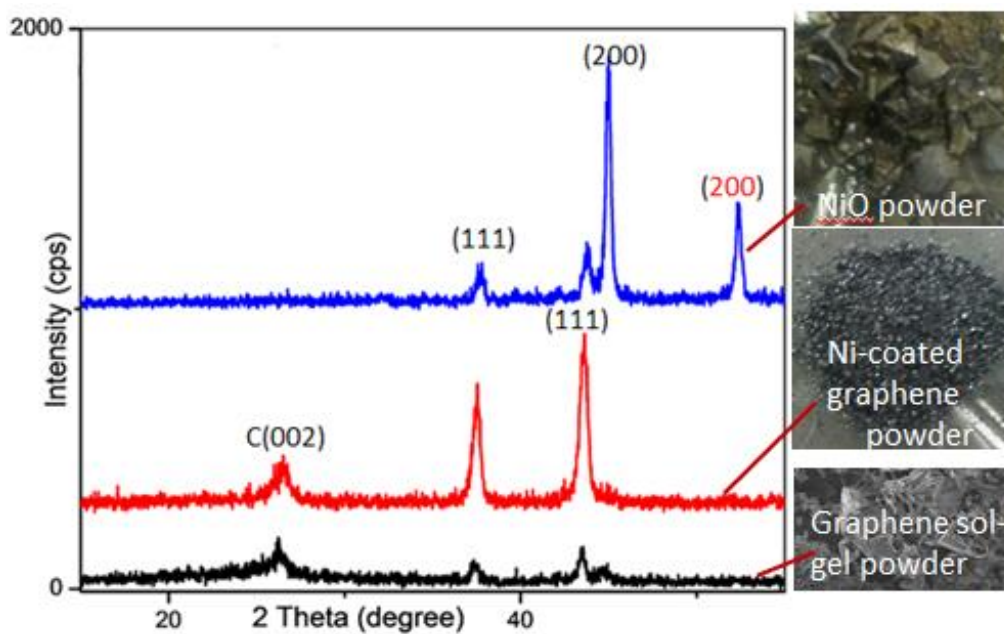


Figure 6.9. X-ray crystallography spectrum of graphene sol gel powder (blue) only nickel oxide at 209C, (red) nickel coated with multilayers of graphene and (black) only etched graphene sol gel powder.

The spectra indicated that nickel is still present in the graphene sol gel after etching. This could be attributed to poor washing conditions, incomplete etching of nickel or nickel that has been completely coated with graphene. All the possible reasons can be resolved to a lowest degree to give high pure pristine and highly conductive graphene powder than any existing carbon source in the market. The next objective will be to rewash the material and assemble a device for energy storage and another devices for gas sensors.

6. 4. 0 Multilayered porous graphene films for gas sensors

Single layer and few layers graphene have been synthesized via chemical vapor deposition and mechanical exfoliation of graphite for gas sensors applications^{190,191-34}. Chemical vapor deposition technologies have also enabled the fabrications of porous single layer graphene material known as nanomesh for sensors applications⁷⁴. Graphene nanomeshes have only been synthesized using lithographic technologies. This method is not only time consuming, the technique is also very expensive, require high labor and material wastage. Some modifications of the technique rearrangement of the CVD synthesis graphene on wafer using different geometry to obtain different nanomeshes¹⁹². One of the challenges involved in this technology is the need for a flat substrate to support the graphene nanomesh. With high surface energy and the interaction between the substrate and graphene nanomesh, the substrate act as a doper reducing the conductivity and sensitivity of the graphene nanomesh. To integrate this technology we hypothesize the used of nickel nanoparticles to synthesize a free standing thin film of graphene that can used for different applications such as sensors and transistors.

6. 4. 1 Experimental

Nickel sol gel was synthesized as described above using nickel nitrate, nickel chloride and sodium hydroxide in a 1:1 volume ratio of deionized water and ethanol. A ceramic bolt was filled with nickel hydroxide nanoparticles and inserted into the CVD chamber and the pressure was set to 10mtorr. The CVD was run at 290°C for 30 minutes for complete reduction of nickel hydroxide to nickel oxide. The temperature was increased to 500°C for 30 minutes under hydrogen gas (3sccm) and acetylene (0.5sccm) the pressure increased up to 500mtors. The CVD was turned off and wait for its return to room temperature. A silvering graphene nickel thin film was form about the

ceramic bolt on the quartz wall. The thin flexible film can be pill off and shape into different geometries that suits its applications.

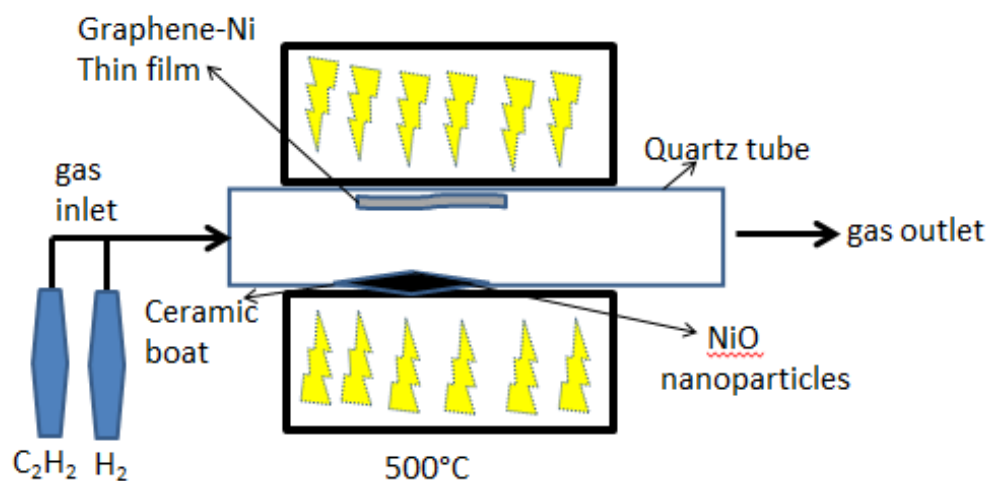


Diagram 6.1. Schematic set up of the chemical vapor deposition for the growth of silvery grey graphene-nickel thin film

6. 4. 2 Analysis of the graphene thin film (mesh)

The synthesized graphene mesh was analyzed using scanning electron microscopy, Raman spectroscopy, X-ray diffraction spectroscopy and energy dispersive X-ray spectroscopy. Mechanical analysis shows that the graphene-nickel thin film is very conductive and flexible. The graphene-nickel film was suspended onto iron III chloride solution over 30 minutes followed by rigorous cleaning with deionized water. The material was fished out with silicon oxide wafer for SEM analysis as shown in figure 10 below.

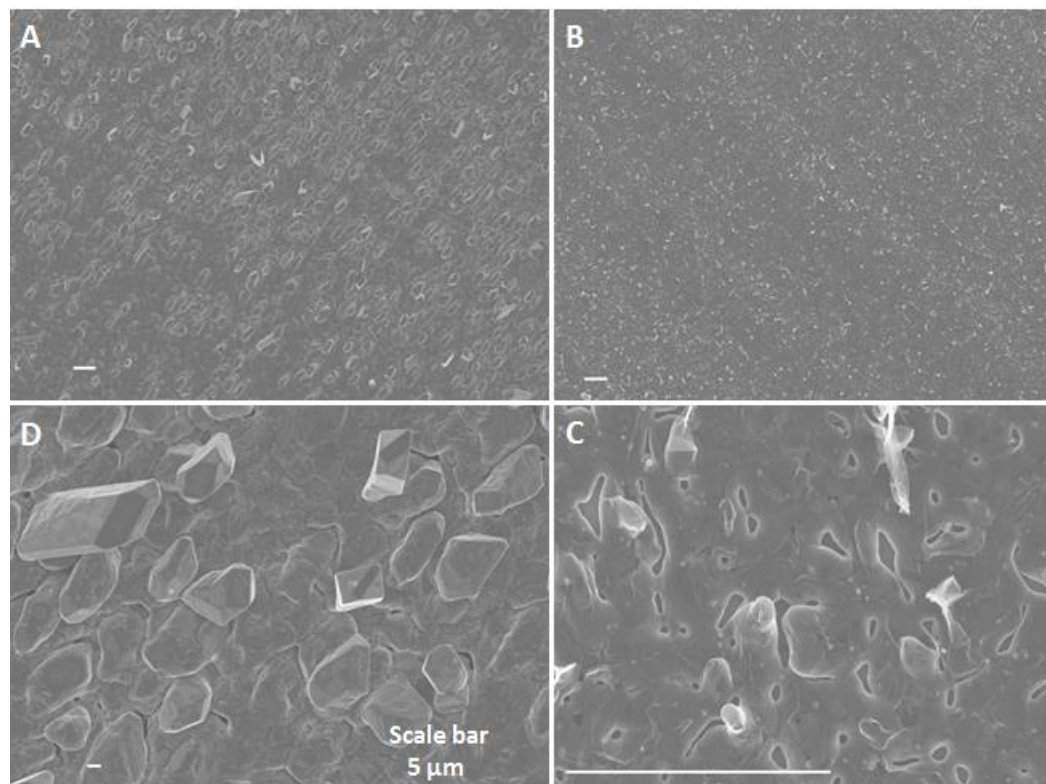


Figure 6.10. Scanning electron micrographs of graphene-nickel thin film and graphene thin layer mesh. (a & d) SEM images of graphene-nickel thin film and (b & c) SEM images of graphene thin film mesh after etching the nickel with iron III chloride solution.

The energy dispersive X-ray spectrograph shown in figure 11 below indicates complete etching of the nickel. The Raman analysis also included in figure 11 shows that the film is of high graphitic quality as the D-band is less intense compared to that from the graphene sol gel powder.

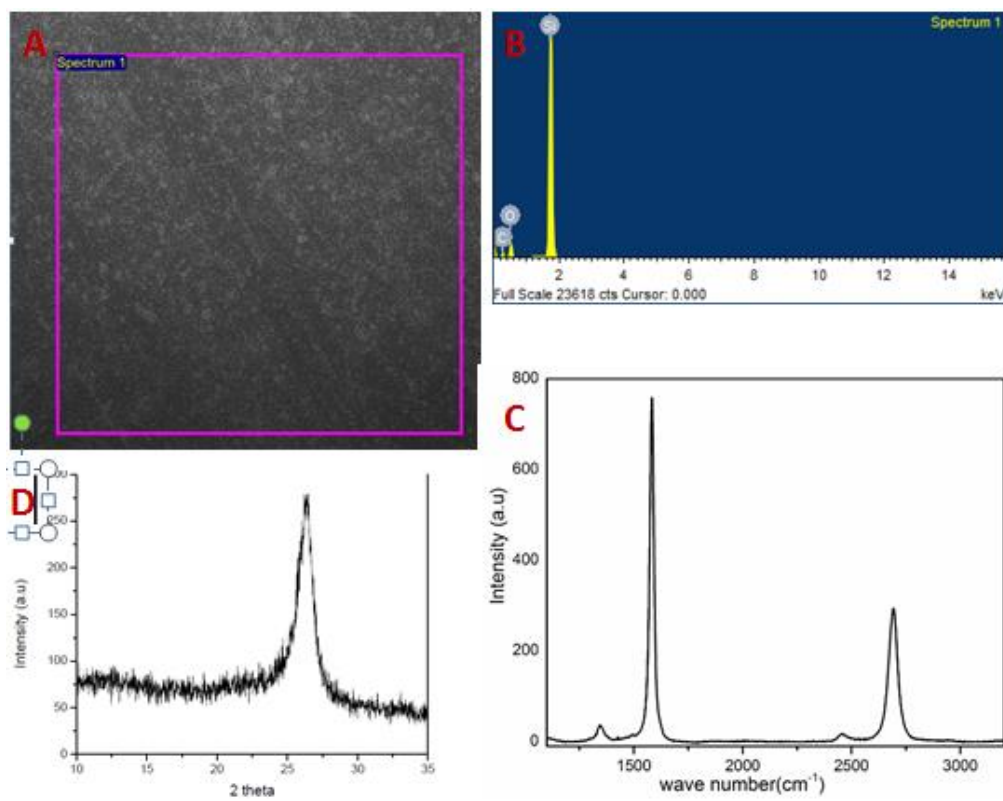


Figure 6.11. Energy dispersive X-ray spectrograph, Raman spectrum and X-ray diffractogram of the graphene mesh. (a & b) EDX image and spectra of the graphene mesh, (C) Raman spectrum of the graphene mesh and (d) XRD spectrum of the graphene mesh on silicon wafer.

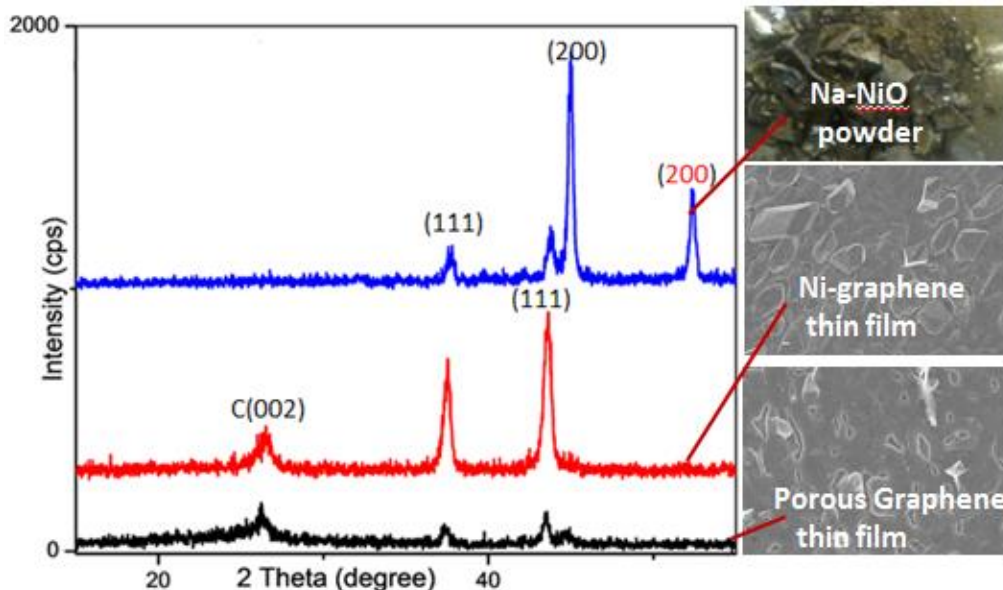


Figure.12. XRD spectra of nickel oxide (blue), graphene-coated nickel (red) and graphene powder.

Comparing XRD in figure 11 and that in figure12, it is easier to etch nickel from the thin film than from the sol gel. The reason could be concentration of nickel in the thin film is not much compared to graphene-nickel sol gel and/or that the time of exposure is enough to etch the nickel out of the thin film. The ability to transfer the graphene thin film onto any substrate is an advantage over the existing graphene nanomesh. The synthesized graphene mesh will be applicable in the fabrication of gas sensor devices.

6. 5. 0 Conclusions

We have created and proven that three dimensional nanostructure of graphene can be synthesized via Nano architecture frame works design. While these are new technologies, optimizing them still require a lot of work and analyses. Work has to done to enable scaling up productivity to insure high quality material as well as devices. These new materials will be implemented in energy storage, electronics and sensors devices

References

1. Purwins, H. *et al.* Regression methods for virtual metrology of layer thickness in chemical vapor deposition. *IEEE/ASME Trans. Mechatronics* **19**, 1–8 (2014).
2. Zhang, H., Yu, X. & Braun, P. V. Three-dimensional bicontinuous ultrafast-charge and -discharge bulk battery electrodes. *Nat. Nanotechnol.* **6**, 277–281 (2011).
3. Science & Technology Concentrates. *Chem. Eng. News Arch.* **92**, 28–29 (2014).
4. Novoselov, K. S. *et al.* Electric field effect in atomically thin carbon films. *Science* **306**, 666–669 (2004).
5. Berlin, L. R. Robert Noyce and Fairchild Semiconductor, 1957–1968. *Bus. Hist. Rev.* **75**, 63–101 (2001).
6. Goldstein, S. C. The impact of the nanoscale on computing systems. *IEEE/ACM Int. Conf. Comput. Des. Dig. Tech. Pap. ICCAD* **2005**, 654–660 (2005).
7. Keyes, R. W. What makes a good computer device? *Science* **230**, 138–144 (1985).
8. Teal, G. K. Single crystals of germanium and silicon - Basic to the transistor and integrated circuit. *IEEE Trans. Electron Devices* **23**, 621–639 (1976).
9. Goldberger, J., Hochbaum, A. I., Fan, R. & Yang, P. Vertically Integrated Nanowire Field Effect Transistors. *Mater. Sci.* **1**, 1–7 (2006).
10. Jurczak, M. *et al.* Silicon-on-Nothing (SON)— an Innovative Process for Advanced CMOS. **47**, 2179–2187 (2000).
11. Keyes, R. W. Physical limits of silicon transistors and circuits. *Reports Prog. Phys.* **68**, 2701–2746 (2005).
12. Lansbergen, G. P. Nanoelectronics: Transistors arrive at the atomic limit. *Nat. Nanotechnol.* **7**, 209–210 (2012).
13. Bhaskaran, H. *et al.* Ultralow nanoscale wear through atom-by-atom attrition in silicon-containing diamond-like carbon. *Nat. Nanotechnol.* **5**, 181–185 (2010).
14. Tao, L. *et al.* Silicene field-effect transistors operating at room temperature. *Nat. Nanotechnol.* 1–5 (2015). doi:10.1038/nnano.2014.325

15. Paul, R. K., Badhulika, S., Saucedo, N. M. & Mulchandani, A. Graphene nanomesh as highly sensitive chemiresistor gas sensor. *Anal. Chem.* **84**, 8171–8 (2012).
16. Zhu, Y. *et al.* A seamless three-dimensional carbon nanotube graphene hybrid material. *Nat. Commun.* **3**, 1225 (2012).
17. Ren, W. & Cheng, H.-M. The global growth of graphene. *Nat. Nanotechnol.* **9**, 726–730 (2014).
18. Novoselov, K. S. *et al.* A roadmap for graphene. *Nature* **490**, 192–200 (2012).
19. Wei, Y. *et al.* The nature of strength enhancement and weakening by pentagon-heptagon defects in graphene. *Nat. Mater.* **11**, 759–63 (2012).
20. Nardecchia, S., Carriazo, D., Ferrer, M. L., Gutiérrez, M. C. & del Monte, F. Three dimensional macroporous architectures and aerogels built of carbon nanotubes and/or graphene: synthesis and applications. *Chem. Soc. Rev.* **42**, 794–830 (2013).
21. Wang, X. & Shi, Y. I. Fabrication Techniques of Graphene Nanostructures. 1–30 (2004).
22. Geim, a K. Graphene: status and prospects. *Science* **324**, 1530–4 (2009).
23. Das, T. K. & Prusty, S. Recent advances in applications of graphene. *Chem. Siences Appl.* **4**, 39–55 (2013).
24. Lin, Q. *et al.* Step-by-Step Fracture of Two-Layer Stacked Graphene Membranes. 10246–10251 (2014).
25. Jhon, Y. & Jhon, M. Chiral-Dependent Tensile Mechanics of Graphene. *Arxiv* 1–13 (2013). at <<http://arxiv.org/abs/1301.6834>>
26. Sridhar, V. *et al.* Nanostructures with Ultrahigh. 10562–10570 (2012).
27. Gladstone, S. Graphene and Its Applications. *Dartmouth Undergrad. J. Sci.* 6–8 (2012). doi:10.1149/1.3119527
28. Lee, Y. *et al.* Wafer-scale synthesis and transfer of graphene films. *Nano Lett.* **10**, 490–3 (2010).
29. Leggett, L. A. J. Lecture 5 : Graphene : Electronic band structure and Dirac fermions. *Condens. Matter Phys.* 1–12 (2010).
30. Liu, C., Yu, Z., Neff, D., Zhamu, A. & Jang, B. Z. Graphene-based supercapacitor with an ultrahigh energy density. *Nano Lett.* **10**, 4863–8 (2010).

31. Liu, K. *et al.* An atlas of carbon nanotube optical transitions. *Nat. Nanotechnol.* **7**, 325–9 (2012).
32. Nandkishore, R., Levitov, L. & Chubukov, A. Chiral superconductivity from repulsive interactions in doped graphene. *Nat. Phys.* **8**, 158–163 (2011).
33. Chen, L., Wang, L. & Beljonne, D. Designing coved graphene nanoribbons with charge carrier mobility approaching that of graphene. *Carbon N. Y.* **77**, 868–879 (2014).
34. Rumyantsev, S., Liu, G., Shur, M. S., Potyrailo, R. a & Balandin, A. a. Selective gas sensing with a single pristine graphene transistor. *Nano Lett.* **12**, 2294–8 (2012).
35. Zhou, F., Li, Z., Shenoy, G. J., Li, L. & Liu, H. Enhanced room-temperature corrosion of copper in the presence of graphene. *ACS Nano* **7**, 6939–6947 (2013).
36. Yong, V. & Tour, J. M. Theoretical efficiency of nanostructured graphene-based photovoltaics. *Small* **6**, 313–318 (2010).
37. Lang, X., Hirata, A., Fujita, T. & Chen, M. Nanoporous metal/oxide hybrid electrodes for electrochemical supercapacitors. *Nat. Nanotechnol.* **6**, 232–6 (2011).
38. Chung, S.-Y., Bloking, J. T. & Chiang, Y.-M. Electronically conductive phospho-olivines as lithium storage electrodes. *Nat. Mater.* **1**, 123–128 (2002).
39. Šljukić, B. R., Kadara, R. O. & Banks, C. E. Disposable manganese oxide screen printed electrodes for electroanalytical sensing. *Anal. Methods* **3**, 105 (2011).
40. Kovanda, F., Grygar, T. & Dorničák, V. Thermal behaviour of Ni-Mn layered double hydroxide and characterization of formed oxides. *Solid State Sci.* **5**, 1019–1026 (2003).
41. Luhrs, C., Daskam, C., Gonzalez, E. & Phillips, J. Fabrication of a Low Density Carbon Fiber Foam and Its Characterization as a Strain Gauge. *Materials (Basel)*. **7**, 3699–3714 (2014).
42. Zhang, J., Jiang, J. & Zhao, X. S. Synthesis and capacitive properties of manganese oxide nanosheets dispersed on functionalized graphene sheets. *J. Phys. Chem. C* **115**, 6448–6454 (2011).
43. Gauza, L. & Hall, H. Enhanced light harvesting in dye-sensitized solar cells with highly reflective surfaces .
44. Nokami, T. *et al.* and -Discharge Lithium-Ion Batteries with High Capacity. (2012).

45. Liu, Y., Artyukhov, V. I., Liu, M., Harutyunyan, A. R. & Yakobson, B. I. Feasibility of lithium storage on graphene and its derivatives. *J. Phys. Chem. Lett.* **4**, 1737–1742 (2013).
46. Kim, O. H. *et al.* Ordered macroporous platinum electrode and enhanced mass transfer in fuel cells using inverse opal structure. *Nat. Commun.* **4**, 2473 (2013).
47. Chen, Y.-C. *et al.* Highly flexible supercapacitors with manganese oxide nanosheet/carbon cloth electrode. *Electrochim. Acta* **56**, 7124–7130 (2011).
48. Dong, X., Wang, L., Wang, D., Li, C. & Jin, J. Layer-by-Layer Engineered Co À Al Hydroxide Nanosheets / Graphene Multilayer Films as Flexible Electrode for Supercapacitor. 293–298 (2012).
49. Zhu, Y. *et al.* Carbon-based supercapacitors produced by activation of graphene. *Science* **332**, 1537–41 (2011).
50. Sun, Z. *et al.* Growth of graphene from solid carbon sources. *Nature* **468**, 549–52 (2010).
51. Zhong-Shuai Wu, Wencai Ren, Li Xu, Feng Li, and H.-M. C. Doped Graphene Sheets As Anode Materials with Superhigh Rate and Large Capacity for Lithium Ion Batteries. *ACS Nano* **5**, 5463–5471 (2011).
52. Cheng, Q.-Y. *et al.* Supramolecular self-assembly induced graphene oxide based hydrogels and organogels. *Langmuir* **28**, 3005–10 (2012).
53. William S. Hummers, J. & Offeman, R. E. Preparation of Graphitic Oxide. *J. Am. Chem. Soc* **80**, 1339 (1958).
54. Li, D., Müller, M. B., Gilje, S., Kaner, R. B. & Wallace, G. G. Processable aqueous dispersions of graphene nanosheets. *Nat. Nanotechnol.* **3**, 101–105 (2008).
55. Reina, A. *et al.* Large area, few-layer graphene films on arbitrary substrates by chemical vapor deposition. *Nano Lett.* **9**, 30–35 (2009).
56. Zhang, L. L. *et al.* Highly conductive and porous activated reduced graphene oxide films for high-power supercapacitors. *Nano Lett.* **12**, 1806–12 (2012).
57. Shen, H., Zhang, L., Liu, M. & Zhang, Z. Biomedical applications of graphene. *Theranostics* **2**, 283–294 (2012).
58. Serrano, M. C., Gutiérrez, M. C. & Del Monte, F. Role of polymers in the design of 3D carbon nanotube-based scaffolds for biomedical applications. *Prog. Polym. Sci.* **39**, 1448–1471 (2014).

59. Liu, S. *et al.* Lateral Dimension Dependent Antibacterial Activity of Graphene Oxide Sheets. *Langmuir* (2012). doi:10.1021/la3023908
60. Manuscript, A. NIH Public Access. *Changes* **29**, 997–1003 (2012).
61. Kim, K. S. *et al.* Large-scale pattern growth of graphene films for stretchable transparent electrodes. *Nature* **457**, 706–710 (2009).
62. Dai, B. *et al.* High-quality single-layer graphene via reparative reduction of graphene oxide. *Nano Res.* **4**, 434–439 (2011).
63. Son, D. I. *et al.* Emissive ZnO–graphene quantum dots for white-light-emitting diodes. *Nat. Nanotechnol.* **7**, 465–471 (2012).
64. Lee, J., Tao, L., Hao, Y., Ruoff, R. S. & Akinwande, D. Embedded-gate graphene transistors for high-mobility detachable flexible nanoelectronics. *Appl. Phys. Lett.* **100**, 1–5 (2012).
65. Hwang, G., Acosta, J. C., Vela, E., Haliyo, S. & Régnier, S. Graphene as thin film infrared optoelectronic sensor. *ISOT 2009 - Int. Symp. Optomechatronic Technol.* 169–174 (2009). doi:10.1109/ISOT.2009.5326118
66. Lu, R., Christianson, C., Weintrub, B. & Wu, J. Z. High Photoresponse in Hybrid Graphene – Carbon Nanotube Infrared Detectors. 11703–11707 (2013).
67. Stoller, M. D., Park, S., Zhu, Y., An, J. & Ruoff, R. S. Graphene-based ultracapacitors. *Nano Lett.* **8**, 3498–502 (2008).
68. Yi, M. & Shen, Z. A review on mechanical exfoliation for scalable production of graphene. *J. Mater. Chem. A* **00**, 1–16 (2015).
69. Lofgran, S. C. Thin Film Deposition & Vacuum Technology.
70. Asatekin, A. *et al.* Designing polymer surfaces via vapor deposition. *Mater. Today* **13**, 26–33 (2010).
71. Graphene, T. Large-Area Bernal-Stacked. (2012).
72. Chen, T. *et al.* High throughput exfoliation of graphene oxide from expanded graphite with assistance of strong oxidant in modified Hummers method. *J. Phys. Conf. Ser.* **188**, 012051 (2009).
73. Schwierz, F. Graphene transistors. *Nat. Nanotechnol.* **5**, 487–496 (2010).
74. Bai, J., Zhong, X., Jiang, S., Huang, Y. & Duan, X. Graphene nanomesh. *Nat. Nanotechnol.* **5**, 190–4 (2010).

75. Choi, B. G., Yang, M., Hong, W. H., Choi, J. W. & Huh, Y. S. 3D Macroporous Graphene Frameworks for Supercapacitors with High Energy and Power Densities. (2012).
76. Wilson, P. M. *et al.* Three-dimensional periodic graphene nanostructures. *J. Mater. Chem. C* **2**, 1879 (2014).
77. Grandthyll, S. *et al.* Epitaxial growth of graphene on transition metal surfaces: chemical vapor deposition versus liquid phase deposition. *J. Phys. Condens. Matter* **24**, 314204 (2012).
78. Ji, H. *et al.* Graphene growth using a solid carbon feedstock and hydrogen. *ACS Nano* **5**, 7656–61 (2011).
79. Pettes, M. T., Ji, H., Ruoff, R. S. & Shi, L. Thermal transport in three-dimensional foam architectures of few-layer graphene and ultrathin graphite. *Nano Lett.* **12**, 2959–64 (2012).
80. Lee, S., Lee, K. & Zhong, Z. Wafer scale homogeneous bilayer graphene films by chemical vapor deposition. *Nano Lett.* **10**, 4702–7 (2010).
81. Sakhalkar, S. & Hirt, D. Admicellar polymerization of polystyrene on glass fibers. *Langmuir* **11**, 3369–3373 (1995).
82. Lee, K. C. & Wi, H. A. Synthesis of crosslinked polystyrene particles by seeded batch polymerization with monomer absorption. *Trans. Nonferrous Met. Soc. China (English Ed.)* **21**, 1–7 (2011).
83. Ou, J. L., Yang, J. K. & Chen, H. Styrene/potassium persulfate/water systems: Effects of hydrophilic comonomers and solvent additives on the nucleation mechanism and the particle size. *Eur. Polym. J.* **37**, 789–799 (2001).
84. Hyun, J. & Chilkoti, A. Surface-initiated free radical polymerization of polystyrene micropatterns on a self-assembled monolayer on gold. *Macromolecules* **34**, 5644–5652 (2001).
85. Henzie, J., Grünwald, M., Widmer-Cooper, A., Geissler, P. L. & Yang, P. Self-assembly of uniform polyhedral silver nanocrystals into densest packings and exotic superlattices. *Nat. Mater.* **11**, 131–7 (2012).
86. Xia, X. *et al.* Graphene sheet/porous NiO hybrid film for supercapacitor applications. *Chemistry* **17**, 10898–905 (2011).
87. Soltan-Dehghan, M., Sharifi-Sanjani, N. & Naderi, N. Preparation of polystyrene/poly(vinyl acetate) nanocomposites with a core-shell structure via emulsifier-free emulsion polymerization. *J. Appl. Polym. Sci.* **100**, 2409–2414 (2006).

88. Massafra, M. P., Moore, D. G. & Torresi, R. M. Nanostructured Thin Films Obtained by Electrodeposition over a Colloidal Crystal Template: Applications in Electrochemical Devices. **20**, 663–673 (2009).
89. Ferrari, A. C. Raman spectroscopy of graphene and graphite: Disorder, electron–phonon coupling, doping and nonadiabatic effects. *Solid State Commun.* **143**, 47–57 (2007).
90. Ferrari, A. C. *et al.* Raman spectrum of graphene and graphene layers. *Phys. Rev. Lett.* **97**, 1–4 (2006).
91. Dodd Gray, Adam McCaughan, B. M. Crystal Structure of Graphite, Graphane and Silicon. **2**, 1–20 (2009).
92. Maiyalagan, T., Dong, X., Chen, P. & Wang, X. Electrodeposited Pt on three-dimensional interconnected graphene as a free-standing electrode for fuel cell application. *J. Mater. Chem.* **22**, 5286 (2012).
93. Cao, X., Yin, Z. & Zhang, H. Three-dimensional graphene materials: preparation, structures and application in supercapacitors. *Energy Environ. Sci.* **7**, 1850 (2014).
94. Dong, X. *et al.* 3D graphene foam as a monolithic and macroporous carbon electrode for electrochemical sensing. *ACS Appl. Mater. Interfaces* **4**, 3129–33 (2012).
95. Kim, I. D., Rothschild, A., Hyodo, T. & Tuller, H. L. Microsphere templating as means of enhancing surface activity and gas sensitivity of CaCu 3Ti 4O 12 thin films. *Nano Lett.* **6**, 193–198 (2006).
96. Stein, I. Y. & Wardle, B. L. Morphology and processing of aligned carbon nanotube carbon matrix nanocomposites. *Carbon N. Y.* **68**, 807–813 (2014).
97. Gutierrez, M. C. *et al.* Biocompatible MWCNT scaffolds for immobilization and proliferation of E. coli. *J. Mater. Chem.* **17**, 2992 (2007).
98. Yan, Z. *et al.* Rebar graphene. *ACS Nano* **8**, 5061–5068 (2014).
99. Chang, C.-H. *et al.* Assembling nanoparticle catalysts with nanospheres for periodic carbon nanotube structure growth. *Nanotechnology* **22**, 035301 (2011).
100. Chang, C.-H., Tan, C.-W., Miao, J. & Barbastathis, G. Self-assembled ferrofluid lithography: patterning micro and nanostructures by controlling magnetic nanoparticles. *Nanotechnology* **20**, 495301 (2009).
101. Prosser, J. H., Brugarolas, T., Lee, S., Nolte, A. J. & Lee, D. Avoiding cracks in nanoparticle films. *Nano Lett.* **12**, 5287–91 (2012).

102. Zhou, Y., Hu, L. & Grüner, G. A method of printing carbon nanotube thin films. *Appl. Phys. Lett.* **88**, 123109 (2006).
103. Kim, T. *et al.* Large-scale graphene micropatterns via self-assembly-mediated process for flexible device application. *Nano Lett.* **12**, 743–8 (2012).
104. Lee, S. *et al.* Utilizing 3D SERS active volumes in aligned carbon nanotube scaffold substrates. *Adv. Mater.* **24**, 5261–5266 (2012).
105. Hajiesmaili, S. *et al.* 3D solid carbon foam-based photocatalytic materials for vapor phase flow-through structured photoreactors. *Appl. Catal. A Gen.* **382**, 122–130 (2010).
106. Chae, C. *et al.* 3D-Stacked Carbon Composites Employing Networked Electrical Intra-Pathways for Direct-Printable, Extremely Stretchable Conductors. *ACS Appl. Mater. Interfaces* **7**, 4109–4117 (2015).
107. Xu, F., Lu, W. & Zhu, Y. Controlled 3D Buckling of Silicon Nanowires for.pdf. **5**,
108. Hashim, D. P. *et al.* Covalently bonded three-dimensional carbon nanotube solids via boron induced nanojunctions. *Sci. Rep.* **2**, 363 (2012).
109. Kumar, R., Tiwari, R. S. & Srivastava, O. N. Scalable synthesis of aligned carbon nanotubes bundles using green natural precursor: neem oil. *Nanoscale Res. Lett.* **6**, 92 (2011).
110. Sadakane, M., Horiuchi, T., Kato, N., Takahashi, C. & Ueda, W. Facile Preparation of Three-Dimensionally Ordered Macroporous (3DOM) Alumina, Iron Oxide, Chromium Oxide, Manganese Oxide, and their Mixed Metal Oxides with High Porosity. 5779–5785 (2007).
111. Park, S. *et al.* Colloidal suspensions of highly reduced graphene oxide in a wide variety of organic solvents. *Nano Lett.* **9**, 1593–7 (2009).
112. Vaucher, S., Dujardin, E., Lebeau, B., Hall, S. R. & Mann, S. Higher order construction of molecule-based magnets. *Chem. Mater.* **13**, 4408–4410 (2001).
113. Verploegen, E. *et al.* Non-destructive characterization of structural hierarchy within aligned carbon nanotube assemblies. *J. Appl. Phys.* **109**, 94316–943165 (2011).
114. Hata, K. *et al.* Water-assisted highly efficient synthesis of impurity-free single-walled carbon nanotubes. *Science* **306**, 1362–1364 (2004).
115. Baughman, R. H., Zakhidov, A. a & de Heer, W. a. Carbon nanotubes--the route toward applications. *Science* **297**, 787–792 (2002).

116. Du, C. & Pan, N. Supercapacitors using carbon nanotubes films by electrophoretic deposition. *J. Power Sources* **160**, 1487–1494 (2006).
117. Xiang, R., Einarsson, E., Okawa, J., Miyauchi, Y. & Maruyama, S. Acetylene-Accelerated Alcohol Catalytic Chemical Vapor Deposition Growth of Vertically Aligned Single-Walled Carbon Nanotubes. *J. Phys. (main title)* 7511–7515 (2009).
118. Tucker, P. C., Lita, A. & Lattuner, S. E. Reaction of methane with bulk intermetallics containing iron clusters yields carbon nanotubes. *Chem. Mater.* **25**, 1480–1482 (2013).
119. Wang, Q., Ng, M. F., Yang, S. W., Yang, Y. & Chen, Y. The mechanism of single-walled carbon nanotube growth and chirality selection induced by carbon atom and dimer addition. *ACS Nano* **4**, 939–946 (2010).
120. Schebarchov, D. & Hendy, S. C. Comment on “dynamic catalyst restructuring during carbon nanotube growth.” *ACS Nano* **5**, 685 (2011).
121. Wang, H., Robinson, J. T., Diankov, G. & Dai, H. Nanocrystal growth on graphene with various degrees of oxidation. *J. Am. Chem. Soc.* **132**, 3270–1 (2010).
122. Filled, C. S. *et al.* In Situ Transmission Electron Microscopy Observation of Electrochemical Sodiation of Individual. 3620–3627 (2014).
123. He, Z. *et al.* Iron Catalysts for the Growth of Carbon Nanofibers: Fe, Fe₃C or Both? *Chem. Mater.* **23**, 5379–5387 (2011).
124. Sawangphruk, M., Pinitsoontorn, S. & Limtrakul, J. Surfactant-assisted electrodeposition and improved electrochemical capacitance of silver-doped manganese oxide pseudocapacitor electrodes. *J. Solid State Electrochem.* **16**, 2623–2629 (2012).
125. Lima, F. H. B., Calegaro, M. L. & Ticianelli, E. a. Electrocatalytic activity of manganese oxides prepared by thermal decomposition for oxygen reduction. *Electrochim. Acta* **52**, 3732–3738 (2007).
126. Pang, S.-C. & Anderson, M. Novel Electrode Materials for Ultracapacitors: Structural and Electrochemical Properties of Sol-Gel-Derived Manganese Dioxide Thin Films. *MRS Proc.* **575**, 444–450 (1999).
127. DESAI, B. D., FERNANDES, J. B. & KAMAT DALAL, V. N. Manganese dioxide — a review of a battery chemical. II: Solid state and electrochemical properties of managanese dioxides. *J. Power Sources* **16**, 1–43
128. Calegaro, M. L., Lima, F. H. B. & Ticianelli, E. a. Oxygen reduction reaction on nanosized manganese oxide particles dispersed on carbon in alkaline solutions. *J. Power Sources* **158**, 735–739 (2006).

129. Lima, F. H. B., Calegaro, M. L. & Ticianelli, E. a. Investigations of the catalytic properties of manganese oxides for the oxygen reduction reaction in alkaline media. *J. Electroanal. Chem.* **590**, 152–160 (2006).
130. Beyene, N. W. *et al.* (Bio)sensors based on manganese dioxide-modified carbon substrates: Retrospections, further improvements and applications. *Talanta* **64**, 1151–1159 (2004).
131. Yan, D. *et al.* MnO₂ film with three-dimensional structure prepared by hydrothermal process for supercapacitor. *J. Power Sources* **199**, 409–412 (2012).
132. Xu, C., Shi, S., Sun, Y., Chen, Y. & Kang, F. Ultrathin amorphous manganese dioxide nanosheets synthesized with controllable width. *Chem. Commun.* **49**, 7331–3 (2013).
133. Xiao, W., Wang, D. & Lou, X. W. Shape-Controlled Synthesis of MnO₂ Nanostructures with Enhanced Electrocatalytic Activity for Oxygen Reduction. 1694–1700 (2010).
134. Amini, M., Najafpour, M. M., Nayeri, S., Pashaei, B. & Bagherzadeh, M. Nano-layered manganese oxides as low-cost, easily synthesized, environmentally friendly and efficient catalysts for epoxidation of olefins. *RSC Adv.* **2**, 3654 (2012).
135. Lvov, Y. *et al.* Films of manganese oxide nanoparticles with polycations or myoglobin from alternate-layer adsorption. *Langmuir* **16**, 8850–8857 (2000).
136. Zhang, J., Jiang, J. & Zhao, X. S. Synthesis and Capacitive Properties of Manganese Oxide Nanosheets Dispersed on Functionalized Graphene Sheets. *J. Phys. Chem. C* **115**, 6448–6454 (2011).
137. Cho, J. *et al.* Ketjenblack Carbon Supported Amorphous Manganese Oxides Nanowires as Highly Efficient Electrocatalyst for Oxygen Reduction Reaction in Alkaline Solutions Table of Contents Graphic Ketjenblack Carbon Supported Amorphous Manganese Oxides Nanowires as Highly. *Nano Lett.* 5362–5366 (2011). doi:10.1021/nl2029078
138. Nakayama, M., Kanaya, T. & Inoue, R. Anodic deposition of layered manganese oxide into a colloidal crystal template for electrochemical supercapacitor. *Electrochem. commun.* **9**, 1154–1158 (2007).
139. Lei, Y., Fournier, C., Pascal, J. L. & Favier, F. Mesoporous carbon-manganese oxide composite as negative electrode material for supercapacitors. *Microporous Mesoporous Mater.* **110**, 167–176 (2008).
140. Ahmed, K. A. M., Peng, H., Wu, K. & Huang, K. Hydrothermal preparation of nanostructured manganese oxides (MnO_x) and their electrochemical and photocatalytic properties. *Chem. Eng. J.* **172**, 531–539 (2011).

141. Duay, J. *et al.* Self-Limiting Electrodeposition Properties. 1200–1214 (2013).
142. Hsu, Y.-K., Chen, Y.-C., Lin, Y.-G., Chen, L.-C. & Chen, K.-H. Birnessite-type manganese oxides nanosheets with hole acceptor assisted photoelectrochemical activity in response to visible light. *J. Mater. Chem.* **22**, 2733 (2012).
143. Deng, M. J., Chen, P. Y. & Sun, I. W. Electrochemical study and electrodeposition of manganese in the hydrophobic butylmethylpyrrolidinium bis((trifluoromethyl)sulfonyl)imide room-temperature ionic liquid. *Electrochim. Acta* **53**, 1931–1938 (2007).
144. Lima, A. S., Bocchi, N., Gomes, H. M. & Teixeira, M. F. S. An electrochemical sensor based on nanostructured hollandite-type manganese oxide for detection of potassium ions. *Sensors* **9**, 6613–6625 (2009).
145. Adelkhani, H., Ghaemi, M. & Jafari, S. M. Novel Nanostructured MnO₂ Prepared by Pulse Electrodeposition: Characterization and Electrokinetics. **24**, 857–862 (2008).
146. Zhang, J., Chen, Z., Wang, Z., Zhang, W. & Ming, N. Preparation of monodisperse polystyrene spheres in aqueous alcohol system. *Mater. Lett.* **57**, 4466–4470 (2003).
147. Song, M.-S. *et al.* Porously Assembled 2D Nanosheets of Alkali Metal Manganese Oxides with Highly Reversible Pseudocapacitance Behaviors. *J. Phys. Chem. C* **114**, 22134–22140 (2010).
148. Wang, X., Liu, H., Chen, X., Evans, D. G. & Yang, W. Fabrication of manganese dioxide nanosheet-based thin-film electrode and its electrochemical capacitance performance. *Electrochim. Acta* **78**, 115–121 (2012).
149. Zhang, X. *et al.* Rapid hydrothermal synthesis of hierarchical nanostructures assembled from ultrathin birnessite-type MnO₂ nanosheets for supercapacitor applications. *Electrochim. Acta* **89**, 523–529 (2013).
150. Zhang, X., Sun, X., Zhang, H., Zhang, D. & Ma, Y. Microwave-assisted reflux rapid synthesis of MnO₂ nanostructures and their application in supercapacitors. *Electrochim. Acta* **87**, 637–644 (2013).
151. Liu, Y. *et al.* Manganese dioxide nanosheet arrays grown on graphene oxide as an advanced electrode material for supercapacitors. *Electrochim. Acta* **117**, 528–533 (2014).
152. Julien, C. & Massot, M. Structural transitions in positive electrodes for Li-ion batteries the vibronic approach. *Ionics (Kiel)*. **8**, 6–16 (2002).

153. Eremenko, a. V. *et al.* Manganese Dioxide Nanostructures as a Novel Electrochemical Mediator for Thiol Sensors. *Electroanalysis* **24**, 573–580 (2012).
154. Verdaguer, M., Glavez, M., Garde, R. & Desplanches, C. Electrons at Prussian Blue Work in Analogues. *Electrochem. Soc. Interface* **11**, 28 (2002).
155. Pawlicka, a. *Development of electrochromic devices. Recent patents on nanotechnology* **3**, (2009).
156. Rao, M. C. Structure and Properties of WO_3 Thin Films for Electrochromic Device Application. **5**, 1–8 (2013).
157. Niklasson, G. a. & Granqvist, C. G. Electrochromics for smart windows: thin films of tungsten oxide and nickel oxide, and devices based on these. *J. Mater. Chem.* **17**, 127 (2007).
158. Granqvist, C. G. Electrochromic tungsten oxide: Review of progress 1993-1998. *Sol. Energy Mater. Sol. Cells* **60**, 201–262 (2000).
159. Details, E. Towards Active Optical Interference Security Devices. (2013).
160. Bohnke, O. Gel Electrolyte for Solid-State Electrochromic Cell. *J. Electrochem. Soc.* **139**, 1862 (1992).
161. Kholmanov, I. N. *et al.* Improved Electrical Conductivity of Graphene Films Integrated with Metal Nanowires. (2012).
162. Cai, Y. *et al.* Graphene nanosheets-tungsten oxides composite for supercapacitor electrode. *Ceram. Int.* **40**, 4109–4116 (2014).
163. Reyes-Gil, K. R., Stephens, Z. D., Stavila, V. & Robinson, D. B. Composite WO_3/TiO_2 Nanostructures for High Electrochromic Activity. *ACS Appl. Mater. Interfaces* **7**, 2202–2213 (2015).
164. Coridan, R. H., Shaner, M., Wiggernhorn, C., Brunschwig, B. S. & Lewis, N. S. Electrical and Photoelectrochemical Properties of WO_3/Si Tandem Photoelectrodes. *J. Phys. Chem. C* **117**, 6949–6957 (2013).
165. Huguenin, F., Gonzalez, E. R. & Oliveira, O. N. Electrochemical and electrochromic properties of layer-by-layer films from WO_3 and chitosan. *J. Phys. Chem. B* **109**, 12837–12844 (2005).
166. Tian, Z.-Q., Yu, H.-T. & Wang, Z.-L. Combustion synthesis and characterization of nanocrystalline $LaAlO_3$ powders. *Mater. Chem. Phys.* **106**, 126–129 (2007).
167. Chatten, R., Chadwick, A. V., Rougier, A. & Lindan, P. J. D. The oxygen vacancy in crystal phases of WO_3 . *J. Phys. Chem. B* **109**, 3146–3156 (2005).

168. Cheong, F. C. *et al.* WO₃-x nanorods synthesized on a thermal hot plate. *J. Phys. Chem. C* **111**, 17193–17199 (2007).
169. Su, J., Feng, X., Sloppy, J. D., Guo, L. & Grimes, C. a. Vertically aligned WO₃ nanowire arrays grown directly on transparent conducting oxide coated glass: Synthesis and photoelectrochemical properties. *Nano Lett.* **11**, 203–208 (2011).
170. Lee, W. J. *et al.* Effects of surface porosity on tungsten trioxide(WO₃) films' electrochromic performance. *J. Electron. Mater.* **29**, 183–187 (2000).
171. Yan, Z. *et al.* Growth of Bilayer Graphene on Insulating. 8187–8192 (2011).
172. Boukhvalov, D. W. & Katsnelson, M. I. Chemical functionalization of graphene. *J. Phys. Condens. matter an Inst. Phys. J.* **21**, 344205 (2008).
173. Hong, A. J. *et al.* Graphene flash memory. *ACS Nano* **5**, 7812–7 (2011).
174. Habazaki, H., Hayashi, Y. & Konno, H. Characterization of electrodeposited WO₃ films and its application to electrochemical wastewater treatment. *Electrochim. Acta* **47**, 4181–4188 (2002).
175. Bica, E. *et al.* Characterization of some tungsten trioxide thin films obtained by dip-coating. **1**, 1011–1014 (2009).
176. An, X. *et al.* WO₃ nanorods/graphene nanocomposites for high-efficiency visible-light-driven photocatalysis and NO₂ gas sensing. *J. Mater. Chem.* **22**, 8525 (2012).
177. Lufano, F. & Staiti, P. Performance improvement of Nafion based solid state electrochemical supercapacitor. *Electrochim. Acta* **49**, 2683–2689 (2004).
178. Patra, a., Auddy, K., Ganguli, D., Livage, J. & Biswas, P. K. Sol-gel electrochromic WO₃ coatings on glass. *Mater. Lett.* **58**, 1059–1063 (2004).
179. Marinenko, G. On the atomic weight of potassium. *Talanta* **16**, 1339–1340 (1969).
180. Chen, W., Fan, Z., Zeng, G. & Lai, Z. Layer-dependent supercapacitance of graphene films grown by chemical vapor deposition on nickel foam. *J. Power Sources* **225**, 251–256 (2013).
181. Wan, W., Zhao, Z., Hu, H., Gogotsi, Y. & Qiu, J. Highly controllable and green reduction of graphene oxide to flexible graphene film with high strength. *Mater. Res. Bull.* **48**, 4797–4803 (2013).
182. Qiu, Y., Guo, F., Hurt, R. & Külaots, I. Explosive thermal reduction of graphene oxide-based materials: Mechanism and safety implications. *Carbon N. Y.* **72**, 215–223 (2014).

183. Feng, H., Cheng, R., Zhao, X., Duan, X. & Li, J. A low-temperature method to produce highly reduced graphene oxide. *Nat. Commun.* **4**, 1539 (2013).
184. Park, S. *et al.* Hydrazine-reduction of graphite- and graphene oxide. *Carbon N. Y.* **49**, 3019–3023 (2011).
185. Mao, W. L. & Mao, H.-K. Hydrogen storage in molecular compounds. *Proc. Natl. Acad. Sci. U. S. A.* **101**, 708–10 (2004).
186. Cao, H., Wu, X., Yin, G. & Warner, J. H. Synthesis of adenine-modified reduced graphene oxide nanosheets. *Inorg. Chem.* **51**, 2954–60 (2012).
187. Li, X. *et al.* Transfer of large-area graphene films for high-performance transparent conductive electrodes. *Nano Lett.* **9**, 4359–63 (2009).
188. Qiao, H., Wei, Z., Yang, H., Zhu, L. & Yan, X. Preparation and Characterization of NiO Nanoparticles by Anodic Arc Plasma Method. *J. Nanomater.* **2009**, 1–5 (2009).
189. Yang, X., Cheng, C., Wang, Y., Qiu, L. & Li, D. Liquid-mediated dense integration of graphene materials for compact capacitive energy storage. *Science* **341**, 534–7 (2013).
190. Liu, L. *et al.* Graphene oxidation: thickness-dependent etching and strong chemical doping. *Nano Lett.* **8**, 1965–70 (2008).
191. Gu, F. *et al.* Layer-by-Layer Doping of Few-Layer. **4**, 4595–4600 (2010).
192. Leaird, D. E. *et al.* Layer-by-Layer Removal of Graphene. **331**, (2011).

Appendix

1. Field emission scanning electron microscopy (FE-SEM or SEM).....Hitachi S4700
2. X-Ray diffraction spectroscopy (XRD).....Rigaku Multiflex Diffractometer CuK α
3. Energy dispersion X-Ray spectroscopy (EDX).....FEI-Nova NanoSEM 450
4. X-Ray photoelectron spectroscopy (XPS).....PHI versa probe II instrument Alka
5. Chemical vapor deposition (CVD).....USF
6. Flame atomic absorption spectroscopy (FAAS or AAS).....Perkin-Elmer model 3100
7. Raman spectroscopy.....DXR Raman microscopy 532 nm laser
8. Voltage source.....Agilent

9. Ultraviolet-visible spectroscopy (UV/Vis).....UV-670 with 1200 grooves/mm
10. Potentiostat/Gavanostat.....CH instruments model 1140B